Probing the interactions between particles and biomembranes using lipid vesicles

vorgelegt von

M.Phys.

Eleanor Jane Ewins

geb. in Shoreham-by-Sea, UK

von der Fakultät II – Mathematik und Naturwissenschaften

der Technischen Universität Berlin

zur Erlangung des akademischen Grades

Doktor der Naturwissenschaften

Dr.rer.nat

genehmigte Dissertation

Promotionsausschuss:

Vorsitzender:	Prof. Dr. Karola Rück-Braun
Gutachterin:	Priv.-Doz. Dr. Rumiana Dimova
Gutachter:	Prof. Dr. Michael Gradzielski

Tag der wissenschaftlichen Aussprache: 16.10.18

Berlin 2019

Disclaimer

All parts of this thesis were written and experimental data obtained by myself, Eleanor Jane Ewins.

Acknowledgements

First and foremost, I would like to extend an enormous amount of gratitude to my supervisor, Rumy. Thank you for your guidance and your encouragement all the way through and your vision for the project. I could not imagine working with a more supportive advisor. Except perhaps Tom, who has also been an excellent co-supervisor as well as a close friend. For the many opportunities that this project has given me, I must thank the IRTG 1524 and especially Prof. Schön and Dr. Fliegner. In the same vein, thanks to Prof. Lipowsky and the theory department at the MPIKG for the excellent working environment. The same goes for Prof. Velev at NCSU, I always felt very welcome in your group. I am lucky enough that some of the members of the Dimova group (past and present) also fall into the friendship category, especially Yun and Vasil. Also special thanks to Jan, Roland and Carmen for introducing me to the world of biophysics and your continued help throughout. To you all and the rest of the group, thank you for making my time here so enjoyable. Kasia, Nadin, Sonja and José: thank you for always being there for me and for the many fun times and gossiping sessions, you are truly wonderful friends. Rafa, muito obrigado fofinho; você conseguiu me inspirar e me apoiar, por ser um cientista excepcional e um namorado realmente maravilhoso. Possibly I could have done it without you but thank you very much for doing it with me. Finally, to my family for your unwavering belief, support and love, I am so very grateful. Thank you for being my personal cheerleaders and always listening.

Abstract

Studying the interactions between particles and biological membranes is highly important due to the role that these interactions play in different processes such as drug delivery, medical imaging and understanding cytotoxicity. How particles in our environment interact with cell membranes is a complex problem due, in part, to the highly intricate nature of the cell membrane. Therefore, we use a simple model membrane system formed from phospholipids, one of the main constituents of cellular membranes. This allows us to look at the contributions from system parameters that we can carefully control such the adhesion energy or the lipid composition. In this work, GUVs and LUVs are the model membranes of choice (giant and large unilamellar vesicles, respectively); the majority of the experiments are performed using GUVs due to the option they provide to directly visualise any interactions and the comparable curvature they have with cell membranes (due to their size of 1-100 μm). We incubate these lipid vesicles with two main types of particles: micron-sized particles with both homogeneous and Janus-like surfaces and nanoparticles formed from poly(ionic liquids). For the micron-sized particles we observe charge dependent interactions which take the form of wetting and engulfment of the particles by the membrane. By modulating the proportion of the surface that has an attractive interaction with the membrane (Janus particles), we can control the wetting of the particle surface. Lowering the adhesion energy of the system by tuning the lipid composition also affects the engulfment of the Janus particles. Finally, we indicate a potential application of the interactions between biomembranes and Janus particles through the magnetic manipulation of the adhering particle-vesicle system. In our investigations with poly(ionic liquid) nanoparticles (PILs), we first observed an interaction via the loss of optical contrast for the GUVs. This is caused by the exchange of sugars across the membrane via pores that form in the presence of the PILs. We examine the survival and size of the vesicles for different lipid compositions and PILs concentrations. Microfluidic experiments allow direct visualisation of the interactions and we observe instances of macropore formation. Fluorescently labelled PILs (Rh-PILs) revealed the location of the nanoparticles both on the vesicle membranes and at the GUV interiors. From this we could also determine a density of the nanoparticles on the membranes and the concentration within the vesicles. FRAP (fluorescence recovery after photobleaching) experiments also revealed a decrease in the lipid diffusion coefficient in the presence of PILs. We also draw comparisons between the action of these nanoparticles and that of antimicrobial peptides; further investigations with these particles could result in their use as antimicrobial agents.

Zusammenfassung

Die Interaktion zwischen kolloiden Partikeln und Biomembranen hat einen großen Einfluss auf viele Prozesse, wie zum Beispiel die medizinische Wirkstoffverabreichung, Bildgebung und Zytotoxizität. Das Erforschen dieser Interaktionen ist daher von größter Bedeutung für das Verständnis der Prozesse. Die Beschreibung der Wechselwirkung von Partikeln aus der Umgebung mit der Zellmembran stellt aufgrund des komplexen Aufbaus der Zellmembran ein sehr unfangreiches Problem dar. Für die Untersuchungen verwenden wir daher Modellmembranen aus Phospholipiden, einer der Hauptbestandteil der Zellmembran. Dies erlaubt es den Einfluss einzelner Systemparameter, wie z.B. die Adhäsionsenergie oder Lipidzusammensetzung, zu kontrollieren und zu untersuchen. In dieser Arbeit werden LUVs (engl. large unilamellar vesicles) und GUVs (engl. giant unilamellar vesicles) als Modellmembransystem verwendet. Der Großteil der Experimente wurde an GUVs durchgeführt, da diese durch ihre Größe von 1-100 µm eine ähnliche Krümmung wie die Zellmembran aufweisen. Wir inkubieren Lipidvesikel mit verschiedenen Arten von Partikel: Zum einen Mikrometer große Partikel mit einer homogen Oberfläche und Mikrometer große Janus-Partikel und zum anderen Nanometer große Partikel die aus Polyionischer Flüssigkeit bestehen. Eine von der Oberflächenladung abhängige Benetzung oder Endozytose der Mikrometer großen Partikeln durch die Membran wird beobachtet. Die Benetzung der Partikeloberfläche kann durch das Einstellen des Anteils der mit der Membran adhäsiven Oberfläche (Janus Partikel) verändert werden. Auch die Verringerung der Adhäsionsenergie über Veränderung der Lipidzusammensetzung hat einen Einfluss auf die Endozytose. Abschließend zeigen wir eine mögliche Anwendung des Partikel-Vesikel Systems über die magnetische Bewegung der adhärenten Partikel. Die Interaktion der Partikel aus Polyionischer Flüssigkeit (PILs) mit der Membran wurde über den Verlust des optischen Phasenkontrasts der GUVs beobachtet. Dieser wird durch den Austausch von Zuckern über Membranporen in Anwesenheit der PILs verursacht. Wir untersuchen die Stabilität und Größe der Vesikel für verschiedene Lipidzusammensetzungen und PIL Konzentrationen. Mikrofluidische Experimente erlauben die direkte Visualisierung der Interaktionen und wir beobachten wie Makroporen auf den GUV entstehen. Fluoreszenz markierte PILs (Rh-PILs) enthüllen die Anwesenheit der Nanopartikel sowohl auf der GUV Membran als auch im Inneren der GUVs. Auf diese Weise wurde die Nanopartikelkonzentration auf der Membran und im Inneren der GUVs bestimmt. FRAP (Fluorescence Recovery after Photobleaching) Experimente zeigen eine Verringerung der Lipiddiffusion unter Einwirkung der PILs. Die Wirkung von Nanopartikeln wird mit der von antibakteriellen Peptiden verglichen. Weitere Forschungen mit diesen Partikeln könnten diese als antibakterielle Wirkstoffe etablieren.

Table of Contents

1 Introduction

In this work we use giant unilamellar vesicles (GUVs) as a model membrane system to probe the interactions between biomembranes and particles of different sizes, compositions and surface chemistries. The knowledge of such processes is vital for the understanding and advancement of biomedical applications such as imaging, drug delivery and bio-sensing.

The contents of this thesis are divided into multiple chapters as follows: Chapter 1 introduces the concept of lipid vesicles as model cell membrane systems and the context for studying their interactions with particles, as well laying out the relevant biological and theoretical contexts. Chapter 2 describes common experimental techniques that are used throughout the results chapters. Chapter 3 investigates the interactions between micron-sized particles with different surface properties; of particular interest is the contrast between particles with a uniform or an anisotropic surface chemistry. We focus on the role of charge in these interactions and how modulating the adhesion between particle and vesicle affects the interaction. In Chapter 4 we look at the interactions between nanoparticles formed from poly(ionic liquids) and GUVs and draw comparisons between the action of this new class of particles and antimicrobial peptides. We look specifically at the stability of the GUVs and the location of the nanoparticles relative the vesicle membrane. Finally, we conclude and summarise the work and suggest future experiments and directions.

1.1 Motivation

The interactions that take place between biomembranes and particles are involved in many of the underlying processes that occur for important biomedical applications such as imaging, controlling cytotoxicity and drug delivery.[1–10] For example, in a time of increased antibiotic resistant bacteria,[11–14] nanoparticles are starting to emerge as a promising option for the treatment of undesirable microbes.[15–18] Conversely, the increasing presence of microplastics that mistakenly end up in our environment, for example through the breakdown of plastic waste in the ocean, have been shown to have adverse effects on the marine population.[6] Utilising or preventing, respectively, interactions such as these rely on an understanding of the parameters that govern these processes. In the context of a cell membrane, the interactions between cells and particles have been extensively studied,[2,19–25] with the effects that properties such as particle size[21,26,27] and surface chemistry[28–30] have on the uptake of the particles (to name but a few) among those that have been investigated. However, due to the complex nature of the cell membrane, clearly elucidating which system properties have precisely what effect on an interaction is a challenging task. We seek to probe such interactions using a simplified model of a cell membrane in a “bottom-up” type approach, which allows us to control specific system parameters. A main component of cellular membranes is lipids;[31] thus, we use a model membrane system composed entirely of lipids. In the subsequent sections of this chapter we will introduce the two main building blocks of our studies: the nature of lipids and lipid bilayers and the model systems they form; and the particles that we use, highlighting their notable properties. We also discuss some theoretical predictions that guided our investigations and make note of comparable previous experimental observations.

1.2 The nature of lipids and lipid bilayers

The fundamental constituents of biological membranes are lipids.[31] A cell membrane typically consists of lipids from three different classes: (i) glycerophospholipids, (ii) sphingolipids, and (iii) sterol lipids. The basic structure of these molecules is amphiphilic: they are made up of two regions, a hydrophilic polar head group and a hydrophobic region, typically in the form of two fatty acid tails.[32] An example of the structure can be found in Fig. 1.1. The fatty acid tails can vary in length, denoted by the number of carbon atoms (16-24 commonly), and also can have varying degrees of double bonds. If a fatty acid tail contains no double bonds, such as is the case for most sphingomyelin lipids for example, these lipids are referred to as saturated. Lipid tails that do contain double bonds are referred to as unsaturated, which is the case for most other phospholipids. The headgroups between phospholipids can also vary and are responsible for, among other properties, attributing charge to the lipid. For example, phosphatidylglycerol lipids, a major component of some bacterial membranes, has a negative charge on the phosphate group at neutral pH;[33] an example of the lipid structure for 1-palmitoyl-2-oleoyl-sn-glycero-3-phosphoglycerol (POPG) can be found in Fig. 1.1 B, together with the structure for POPC (1-palmitoyl-2-oleoyl-glycero-3-phosphocholine), the same lipid as depicted schematically in A, for comparison. We utilise the charge afforded to the membrane by different lipid compositions extensively in this work to mimic cell membrane charges and mediate the interaction strengths. In the context of biological membranes, phosphatidylglycerol is a commonly occuring lipid species in bacteria, while phosphatidylcholines (PC) and phosphatidyletahnolamines (PE) are the most abundant lipids in cells.[34,35]

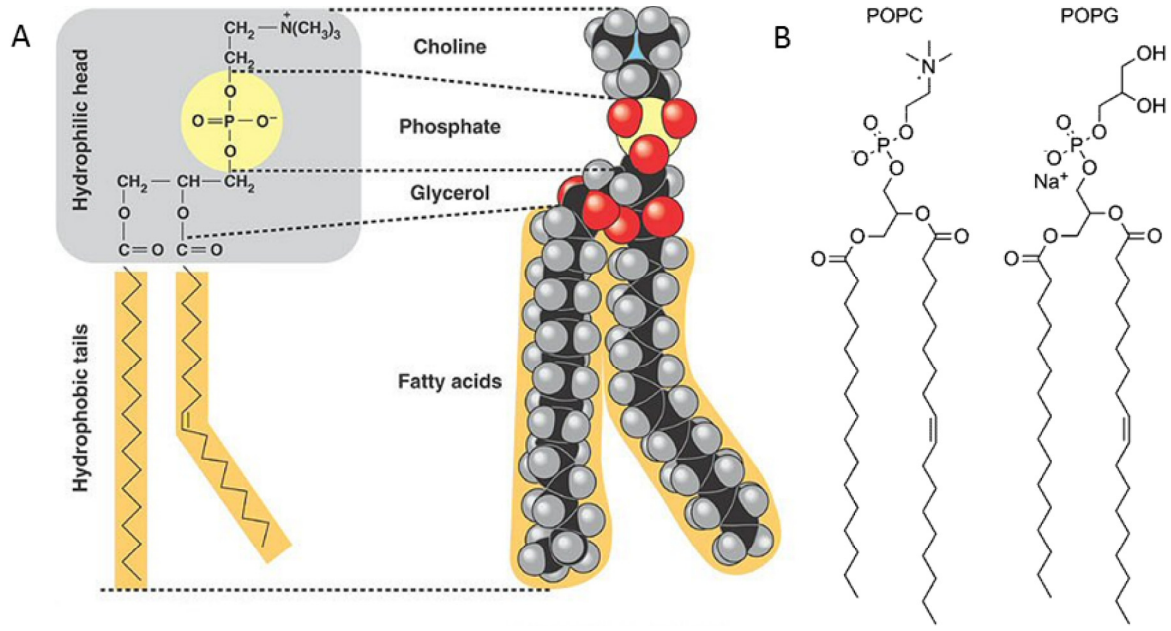

Fig. 1.1 Lipid structures. A) Diagram depicting the main components of an amphiphilic lipid structure, shown here for phosphatidylcholine (POPC). Adapted from [36]. B) Zwitterionic POPC and anionic POPG lipid structures, adapted from [37].

Due to the amphiphilic nature of these molecules, lipids self-assemble in water into structures that minimise the energy of the system. The hydrophobic tails cannot form hydrogen bonds with the water molecules. The lipids form structures that consist of the hydrophilic head groups shielding the fatty acids from the water as this is more energetically favourable. This effect, together with van der Waals interactions between the lipid tails, keeps the assembled lipid structures stable.[38] The nature of such structures depends on a number of factors, such as the specific lipids, salt conditions, temperatures, lipid concentrations etc. For example, at very low concentrations the lipids will typically form micelles; the critical micelle concentration of lipids is between 10^{-7} and 10^{-10} M.[39] The shape of the lipids can also dictate the nature of the structure formed; smaller head group lipids prefer an inverted micelle phase, while larger head group lipids prefer a micellar structure.[40] Please see Fig. 1.2 for a summary of the different phases. We focus on lipid structures in the lamellar phase; more specifically, single lamellar lipid bilayers. Biomembranes are naturally in such a state. Due to the previously described amphiphilic nature of the lipids, one can understand the lipids' preference to assemble into two opposing leaflets which are closed in a spherical configuration, as shown by the vesicle diagram in Fig. 1.2; exposing the hydrophobic core of this structure would be energetically unfavourable. Lipids arranged in such a way provide the basic structural component of cellular membranes. Not only does this provide protection to the interior of the cell (or bacterium) from the external environment, it also provides a site for membrane proteins to associate to or immerse themselves in. According to the model of cellular membranes proposed by Singer and Nicholson, these membranes are fluid and the components can diffuse freely.[41] We next describe typical model membrane systems that assemble into the biomembrane mimicking bilayer phase.

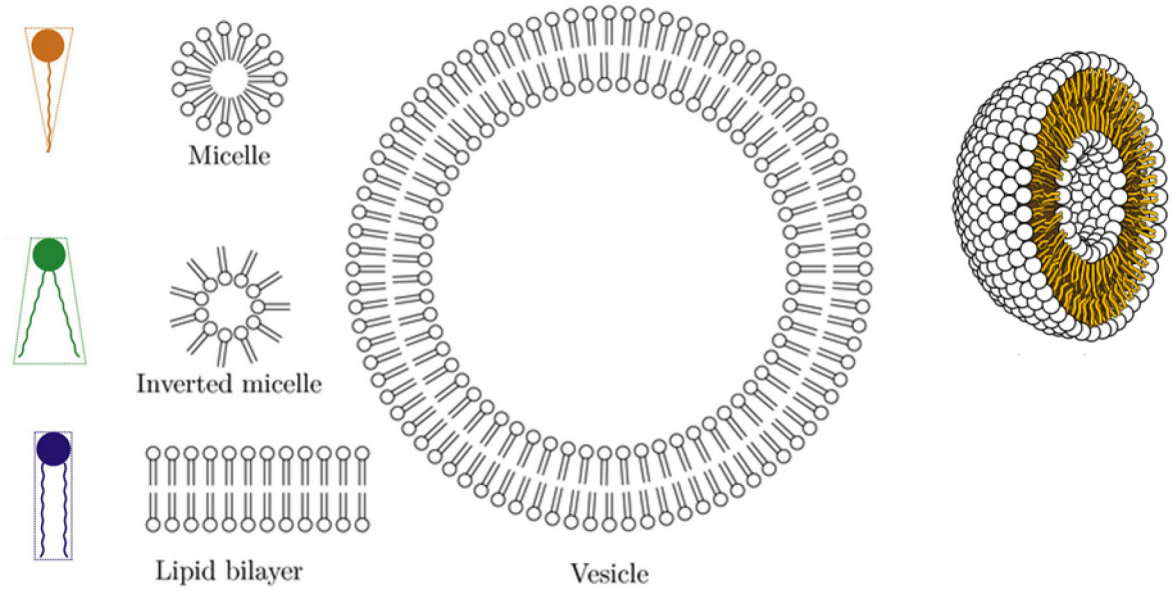

Fig. 1.2. Schematic diagram relating the shape of the lipid molecules to the structure they adopt. Of interest to us are the vesicles that form from the lamellar lipid bilayer phase. Figure adapted from Texample.net, Wikipedia and [42].

1.3 Model cell membrane systems

Many studies have looked at the interactions between particles and cell membranes;[26,43–46] however, extracting the different system parameters that govern and affect these interactions is non-trivial. This is due in part to the highly complex, multi-component environment that cell (both eukaryotic and prokaryotic) membranes have (such as many different lipid and protein species, the underlying cytoskeleton etc.). For example, it has been shown that the stage of the cell cycle that the sample is in can affect uptake of nanoparticles.[47] One approach is to instead employ model membrane systems composed purely of phospholipids to probe the interactions.[48–53]

As previously stated, lipid molecules are one of the most predominant components of eukaryotic and bacterial cellular membranes. As such, it is common practice to use simplified systems consisting of 1 or more lipid components to model the behaviour of these biomembranes in response to external stimuli. Typical model systems are supported lipid bilayers, black lipid membranes and free-standing vesicle systems. Among these vesicle models are small and large unilamellar vesicles (SUVs and LUVs respectively; with sizes in the range 20-100 nm diameter for SUVs and 100-1000 nm for LUVs), which can be used for studies such as measurements of vesicle leakage in bulk.[54,55] Another widely used model membrane system is giant unilamellar vesicles (GUVs). These vesicles have sizes on the order of tens of microns (typically 10-100 μm diameters), which provides several experimental advantages; notably, they can be directly viewed via optical microscopy (see Chapter 2.4) and have curvature that is comparable to a cell membrane. Typical microscopy images of GUVs can be found in Fig. 1.3.

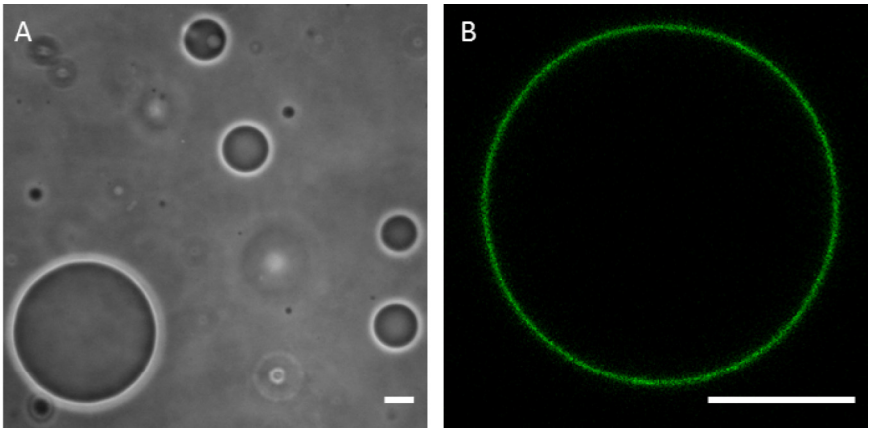

Fig. 1.3. Optical microscopy example images of GUV model membrane systems. A) Phase contrast image of DOPC GUVs; the darker interior and light halo around the vesicles is produced via differences in refractive index between the external and internal solutions (see Chapter 2.4.1 for details). B) Confocal fluorescence microscopy cross-section of DOPC GUV labelled with 1 mol% NBD-PC fluorescent lipid analogue dye (see Chapter 2.4.2 for details).

The versatility of lipid vesicles in terms of composition, size, etc., when combined with the ability to encapsulate hydrophilic and hydrophobic materials, shows the great potential of lipid vesicles for applications such as chemical reactors,[56] and in industries such as cosmetics, food and pharmaceuticals.[57] Small vesicles (SUVs or LUVs) have been extensively used in as drug delivery vehicles and in studies of various membrane properties, while giant vesicles have been used as a cell model for investigating the

effects of different external stimuli (electrical, mechanical, targets of bioactive molecules, etc.) or as (bio) chemical reactors.[58] Of course, the model system of choice should still accurately represent the interaction that is being investigated (in our case, particle interactions). Studies on GUVs with other membrane active agents, such as antimicrobial peptides, have been shown to have a direct relation to the effects observed in cellular studies.[59] As such, GUVs were used primarily in this work as the model of choice for investigating the different interaction mechanisms that particles have with biomembranes.

1.4 Particles and their membrane interactions

The applications of particles, and indeed even the classes and properties of particles themselves, are extremely dense and far-reaching. To name just a few industries, nano)particles are used widely in cosmetics and cosmeceuticals,[60–62] construction,[63,64] and biomedicine and medical imaging.[3–5,7–10,65–67] There are many studies assessing the effects and mechanisms of different particles interacting with different membranes (both biological and model membranes). As such, in this introductory section we will focus primarily on the particles relevant to this work and studies on similar model membrane-particle systems.

In this work we investigate interactions with two main types of particles: microspheres formed from polystyrene and nanoparticles formed from poly(ionic liquid)s. Polystyrene microspheres are one of the most common types of polymer microspheres and have a range of biomedical applications due to their biocompatibility (proteins and ligands adsorb onto polystyrene readily and permanently, for example)[68–70] and tuneable nature.[71] For example, microspheres covered with collagen and growth factors can be injected to the body to induce tissue formation and regeneration.[72] They can be produced via a range of different methods, such as solvent evaporation, spray drying and interfacial polymerisation (to name but a few).[71] Their size means they can be observed with conventional microscopy, which we make use of in this work. Experimental studies on microspheres interacting with GUVs have observed different adhesion and engulfment states, from adhering to fully engulfed, and found that the interactions depends on experimental conditions such as membrane tension or the density of binding sites.[48,51,73,74] We can also prepare Janus surfaces on these microspheres by means of metal vapour deposition on a closely packed particle monolayer (see Chapter 3.2.3 for experimental details). Janus particles are broadly defined as particles that have two sides of different chemistry or polarity.[75] Li et al. reported partial engulfment on tense membranes for particles with a Janus surface.[73] In Chapter 3 we investigate the behaviour of the contact line between GUVs and homogeneous and Janus microspheres that interact via electrostatic interactions and introduce a use of the metallic surface coating to transport adhering vesicles.

Poly(ionic liquid) nanoparticles are a relatively emergent class of nanoparticles, formed via the dispersion polymerisation of ionic liquid monomers.[76,77] These particles combine the attractive properties of polymers, such as flexible functionality, with the properties of ionic liquids.[78] For ionic liquids, some of these properties include anti-microbial-like behaviour.[79,80] In GUV studies, the activity of an anti-microbial agent, typically an anti-microbial peptide, can be observed via methods such as the leakage of molecules into or out of GUVs,[81] changes in membrane morphology (membrane thickening),[82] or GUV bursting.[59]

Nanoparticles formed from more conventional materials (polystyrene and silicon dioxide are the examples herein) have also been shown to disrupt the membrane to produce similar anti-microbial-like effects, such as membrane deformation and pore formation.[53,83] In Chapter 4 we investigate the interaction mechanism between nanoparticles formed of poly(ionic liquid)s and GUVs; to our knowledge, such experiments have not yet been carried out elsewhere.
In the next section we will look at the physical principles and theory that can be used to help describe the interactions of particles with membranes. Theoretical studies examining the interactions of particles and membranes determined that a particle can exist in a free (unbound), partially or fully bound engulfment state. These states depend on the system parameters, such as bending and adhesion energies, membrane tension, and inter-particle-membrane distances.[84–86]

1.5 A physical perspective on particle adhesion and engulfment

For the applications of particle interactions described in section 1.1, the particle must cross the cellular membrane (or at least adhere to it). The internalisation of particles by the membrane is called endocytosis and involves first the adhesion of the particle to the membrane, followed by the membrane spreading over the particle surface and engulfment. In the case of cell membranes, membrane scission then occurs, and the particle wrapped in membrane is disconnected from the main membrane structure.[87,88] A simplified scheme of this wrapping process can be found in Fig. 1.4.

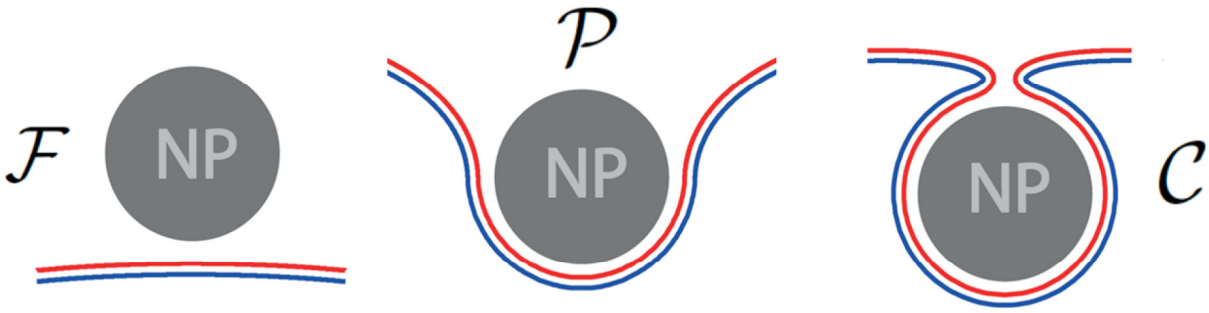

Fig. 1.4 Simplified scheme depicting the stages and states involved with the internalisation of a particle by a model lipid membrane. The letters F, P and C refer to the states free, partially engulfed and completely engulfed respectively. The mechanism is shown for a nanoparticle (NP) of approximately 16 nm in contact with a 4 nm thick membrane, where the red and blue lines depict the outer and inner leaflets respectively. Figure adapted from Agudo-Canalejo & Lipowsky.[84]

For the model membrane system that we employ, we can study the stages of particle adhesion, wrapping and internalisation by the membrane (for particle sizes that are optically resolvable). To consider how a particle interacts with a GUV membrane, we first need to look at the GUV in the absence of particles, in its equilibrium state. As the bilayer thickness (at approximately 4-5 nm) is considerably smaller than the lateral dimensions of the membrane (length scales on the order of >10 μm), the fluid vesicle membrane can be considered as a thin elastic sheet.[89] Helfrich found that the bending energy of the membrane can be expressed using the following equation:[90]

$$E_b = \int \frac{\kappa}{2}(2H - C_0)^2 + \bar{\kappa}K + \sigma \, dA \quad (1)$$

where κ is the bending rigidity of the membrane, H is the curvature, K is the Gaussian curvature, $\bar{\kappa}$ the Gaussian bending rigidity, C_0 is the spontaneous curvature, σ the tension and A the area. This equation describes the energy required to deform a portion of the membrane area. The typical bending rigidity of a fluid bilayer is ~ $20k_bT$, where k_b is the Boltzmann constant and T is the temperature.[91] For the case of a particle being engulfed by a lipid bilayer, the membrane always has to bend, and in cases where the membrane tension is non-zero, it would also need to stretch. In order for these two processes to occur, their associated energy costs need to be overcome; or in other words these energetically unfavourable processes need to be offset by an energy gain for the system. In the case of particle interactions, this energy gain is in the form of the adhesion energy between the particle and the membrane. The source of this adhesion energy depends on the system you are looking at; both specific and generic interactions are possible. The specific interactions are generally related to ligand-receptor pairs on the particle and membrane surfaces, a typical example of which is biotin and avidin. These interactions have been used in other particle-vesicle studies to look at particle adhesion and engulfment.[51,74] Examples of non-specific interactions that occur between particles and membranes are short-range hydration repulsive forces and longer-ranged van der Waals and electrostatic forces, which can be either attractive or repulsive.[92] In the context of the relatively large vesicle shape, one can consider the contribution of these interactions as one value of adhesive strength per unit area, commonly referred to as $|W|$.[93] The energy gained by a particle in contact with a segment of membrane can be described by the following equation, as first proposed by Seifert and Lipowsky:[93]

$$E_{ad} = -|W|A_{ad} \quad (2)$$

where A_{ad} is the area of an adhering membrane segment. If we consider the case of a spherical, tensionless GUV which has fully engulfed a smaller, spherical particle, the bending and adhesion energies must have the relation $E_{ad} > E_b$, which in this specific example can be written as:

$$|W|4\pi R_{pa}^2 > 8\pi\kappa \quad (3)$$

where R_{pa} is the particle radius. For a closed surface, such as a spherical vesicle, the Gaussian bending rigidity has no effect onxf the equilibrium condition and is often neglected.[86,94] It has been theoretically predicted that the particle can also occupy stable partially engulfed states between a free, non-adhering state and a fully engulfed state, as shown in Fig. 1.4 (depending on the system parameters).[84,85] Additionally, theoretical investigations for Janus particles that have two regions of different adhesion energies (one with a high adhesion energy, the other comparatively small) have demonstrated the existence of partially bound states for these particle morphologies as well.[95]

Examining particle interactions using GUVs allows us to more clearly determine the contributions that adhesion to and bending (and in some cases tension) of the membrane

have to the process of engulfment, without the other components of cells that can drive endocytosis, for example the formation of clathrin coated pits.[96]

1.6 Aim of this work

The interactions between biomembranes and particles are important for many applications, such as understanding cytotoxicity, medical imaging and drug delivery. In this work we aimed to explore how the different experimental parameters in a simplified model system can be tuned to facilitate different types of interactions. We attempted to achieve this goal by looking at GUVs with micron-sized polystyrene and silica particles and nanoparticles formed from poly(ionic liquid)s, where we could tune the properties of the vesicle membrane and, for the micron-sized particles, also the particle properties. Being able to produce particles that are perfectly tailored for the aforementioned applications requires an understanding of the role that each component in an interaction plays. Using simplified synthetic biology systems such as GUVs allows us to investigate some of these components without the high complexity of a cell membrane, which takes us closer to the overarching goal.

2 General methods

Throughout this chapter the general materials and methods used in this work are described and the theoretical background is expanded upon where necessary. Any specific values or parameters for the experiments are given in the relevant chapters.

2.1 Materials

Giant unilamellar vesicles and large unilamellar vesicles were all prepared from commercially available phospholipids. The lipid species 1,2-dioleoyl-sn-glycero-3-phosphocholine (DOPC), 1,2-dioleoyl-sn-glycero-3-[phospho-rac-(1-glycerol)] (DOPG), 1,2-dioleoyl-3-trimethylammonium-propane (chloride salt) (DOTAP), 1,2-dipalmitoyl-sn-glycero-3-phosphoethanolamine-N-(lissamine rhodamine B sulfonyl) (Ammonium salt) (Liss-Rhod PE), and 1-Oleoyl-2-[12-[(7-nitro-2-1,3-benzoxadiazol-4-yl)amino]dodecanoyl]-sn-Glycero-3-Phosphocholine (NBD-PC) were acquired from Avanti Polar Lipids (Alabaster, AL). 1,1'-Dioctadecyl-3,3,3',3'-Tetramethylindocarbocyanine Perchlorate was purchased from Thermo Fisher Scientific. For storage, all lipid stocks were dissolved in chloroform and kept at -21 °C. The chemical structures of each lipid can be found in Fig. 2.1. All lipid species are fluid at room temperature. Specific molar concentrations for each lipid composition used are pointed out at the relevant points throughout each chapter.

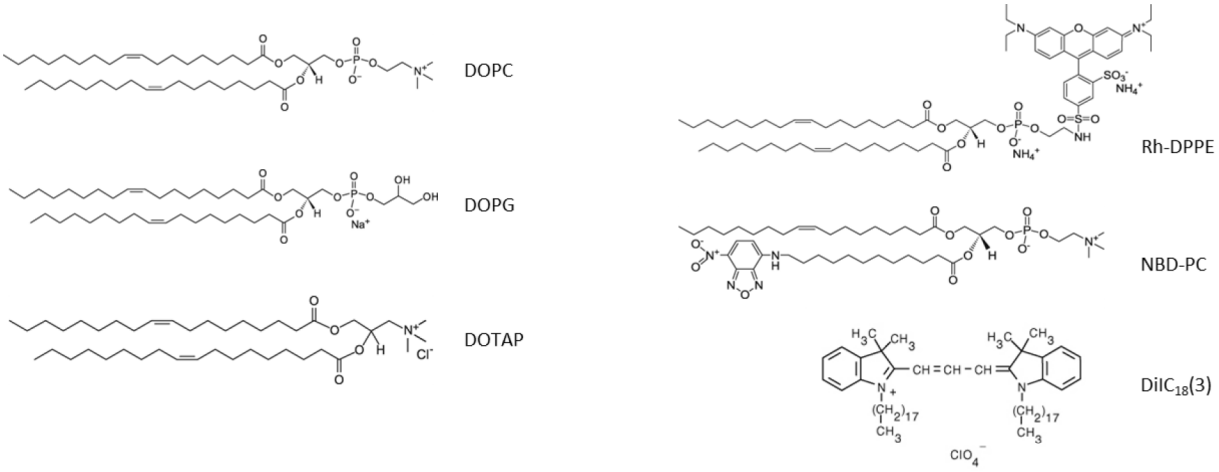

Fig. 2.1 Structures of lipids, fluorescently labelled lipid analogues and dye molecules used throughout this work. Reproduced from Avanti Polar Lipids and Thermo Fisher Scientific.

The effects of membrane charge on particle-membrane interactions are explored throughout both Chapters 3 and 4 in this work. As such, the lipid compositions used throughout are variations on ratios between DOPC (neutral), and DOPG (negative) or DOTAP (positive). The fluorescently labelled lipid molecules Rh-DPPE and NBD-PC are either used for visualisation purposes, for example in Chapter 3.3.3 to determine the vesicle contact line with the particle, or for intensity-based analyses, such as Chapter 4.3.3.1 to determine the number of particles per lipid area. In the latter case, the concentration of the membrane dye was also important. Particles were both obtained commercially and synthesised. 6 μm Polybead® Amino Microspheres were obtained

from Polysciences (Warrington, PA) and 4 μm sulphate polystyrene microspheres were purchased from Interfacial Dynamics Corp. (Eugene, OR). These particles were used both without further treatment and after coating with metal vapour (see Chapter 2.3.1 for further details). 1 μm screenCORE-Amine particles were obtained from Chemiecell (Berlin, Germany). Poly(ionic liquid) nanoparticles, both fluorescently labelled and non-labelled, were provided by M. Antonietti from MPIKG (Colloid Chemistry). Further details on their production can be found in Chapter 2.3.2. A summary of all particle properties used in this work can be found in Fig. S7.1**.** In addition to using fluorescently labelled lipids for vesicle visualisation, we also used different sugar solutions inside and outside of the GUVs, so that their images could be enhanced when viewed via phase-contrast microscopy (details of which can be found in Chapter 2.5.1). As such, sucrose (internal solution) and glucose (external solution) were both obtained from Sigma Aldrich (Darmstadt, Germany).
GUV preparation was performed using the electroformation protocol[97], details of which can be found later in Chapter 2.2.1. For this, indium tin oxide (ITO) coated glasses ITO (film thickness < 100nm, resistance 50 Ω) were obtained from Praezisions Glas & Optik (Iserlohn, Germany). The gel-assisted swelling method was also explored[98] and for this polyvinyl alcohol (PVA) was obtained from Sigma Aldrich (Darmstadt, Germany).
Agarose immobilisation was employed as a method to aid vesicle visualisation[99], by forming a gel-like network within the sample encaging the vesicles (further details are in Chapter 2.4). Low melting temperature agarose was purchased from Fischer Scientifics (Walthan, MA).
In some experiments it was necessary to first passivate the glass coverslip with bovine serum albumin (BSA) at 0.2 wt%, which was obtained from Sigma Aldrich (Darmstadt, Germany).
All aqueous solutions were prepared with Milli-Q water.

2.2 Vesicle preparation

Giant unilamellar vesicles (GUVs) are used predominantly as the model membrane system of choice and the methods we used to form them, electroformation and gel-assisted swelling, are described in this section. Large unilamellar vesicles are also used in Chapter 3 and multi-lamellar vesicles of a similar size are used in Chapter 4. These two smaller vesicle systems provide additional information about the particle-vesicle interactions. The two methods for the production of these vesicles are explained below.

2.2.1 Giant unilamellar vesicles

GUVs were prepared using either the well-known electroformation protocol, as first developed by Angelova and Dimitrov[97], or the gel-assisted swelling method[98]. The electroformation method is first described and then the gel-assisted swelling method. Unless explicitly stated within the subsequent, relevant chapters, the experimental method was kept the same for all experiments. Lipids dissolved in chloroform, of a typical total volume of 16 μL, were deposited on two indium tin oxide (ITO)-coated glasses and dried to evaporate the solvent. The drying was performed first, under a stream of nitrogen, and then under vacuum conditions for 2-2.5 hours at room temperature. After drying the glasses were assembled, together with a Teflon spacer, to form a chamber of volume 2 mL. The chamber was then filled with a solution of sucrose and an AC field was applied,

as shown in the schematic diagram Fig. 2.2. Typical AC field parameters used were 1.2 V, 10 Hz, for 1-2 h. After vesicle formation, the solution was collected from the growth chamber to an Eppendorf tube using a pipette.

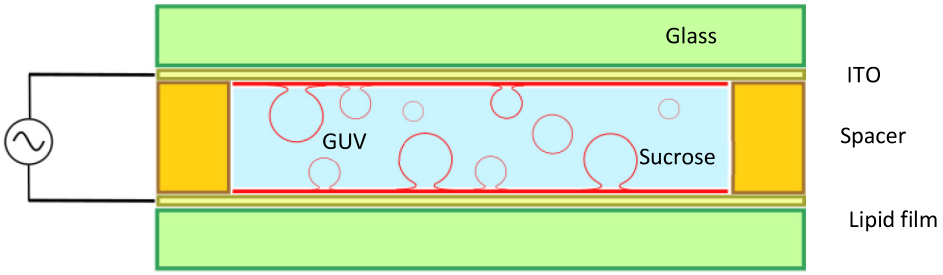

Fig. 2.2 Electroformation of GUVs. Schematic diagram of electroswelling process (not to scale). A lipid film is deposited on ITO coated glasses, which are closed with a spacer to form a chamber. The chamber is then filled with an aqueous solution and an AC field is applied to facilitate/enhance the swelling of GUVs.

Although the process of vesicle formation via electroswelling is not fully understood, some steps have been identified. First, a bud is formed from the lipid bilayer stacks due to the osmotic pressure (the electric field generates the movement of ions, which in turn enhances this pressure). The alternating electric field causes re-distribution of the non-covalently bound lipid counter ions in a periodic fashion; together with the weak dipoles induced in the solution, these factors contribute to generating membrane fluctuations and flow within the solution, which helps separate the bilayers. When these effects overcome the van der Waals inter-bilayer attractions, the bud swells further and eventually pinch off from the lipid stack.[100] After formation, the GUVs can be pipetted out of the growth chamber and are ready to be used for experiments. This method typically produces a large yield of unilamellar vesicles, in the size range 5-100 μm, but this can all vary depending on lipid composition, with some compositions and conditions being more challenging to grow.[101] As such, we also explored the gel-assisted swelling method for GUV preparation.[98]

This method typically produces a smaller vesicle yield than the widely used electroformation method for zwitterionic lipids, but has been shown to be effective in producing more challenging lipid compositions, such as 100% positively charged DOTAP vesicles. The growth protocol was followed as first described by Weinburger et al.[98], and is briefly outlined as follows. Polyvinyl alcohol (PVA) was prepared in 200 mM sucrose solution at a concentration of 5% (w/w). For the PVA to dissolve, the solution was heated at 90˚C and stirred continuously using a magnetic stirring bar. PVA-coated substrates were prepared by pipetting approximately 20 μL of the solution onto glass slides (of size 75×25 mm) and spreading gently with the pipette tip to create a smooth, thin layer. The substrates were then dried for 30 min in an oven at 60˚C. 5-10 μL of lipid solution in chloroform was then spread on the dried PVA film using a syringe. The sample was then dried under a stream of nitrogen and then subsequently placed under vacuum, to evaporate any remaining solvent. After drying, a chamber was formed with a Teflon spacer and a clean glass slide and the lipid film hydrated with 200 mM sucrose solution. The vesicles were then left to form, typically between 30-60 min, after which the sample was removed with a pipette into an Eppendorf tube.

The proposed mechanism of action for the gel-assisted swelling method is shown in Fig. 2.3. When a lipid film is hydrated, it starts to bud and pinch off into vesicles, as described previously and also shown in Fig. 2.3 A. The swelling of the vesicles is as a result of the water penetration into the bilayer stacks, a comparison of which is shown in Fig. 2.3 B for glass and PVA substrates. Water is able to penetrate the bilayers in both cases by two main pathways: by accessing the interlamellar regions from the edges of the stacks and by direct permeation through the membrane. Where the PVA substrate differs from glass is the chemical potential gradient between the outer solution and the dry gel, which drives the water across the bilayer stack and into the gel. This additional water is then able to access the vesicle interior from the gel reservoir, as shown in Fig. 2.3 B on the right. The swelling of the gel as the water enters it also modifies the capillary forces that act at the membrane-gel interface. As the gel swells and stretches, this action may also contribute to generating more membrane defect sites for the water to access and this generates further swelling.

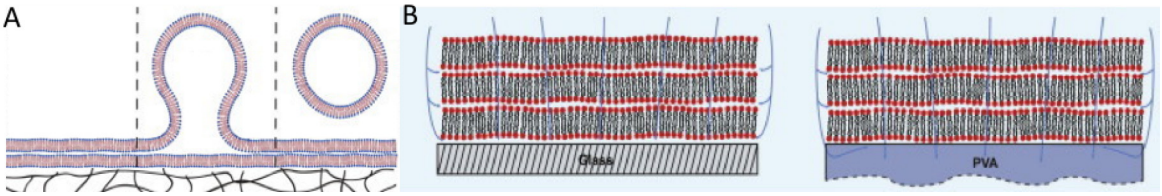

Fig. 2.3 Gel-assisted swelling of GUVs , adapted from Weinberger et al.[98] A) Lipid bilayer stacks on a gel-coated substrate that swell and pinch off to form vesicles. B) Proposed mechanism outlining differences in water transport through and around the lipid bilayers between a conventional glass substrate (left) and a PVA coated substrate (right). Contrary to the case of using a solid material as a swelling support, the PVA gel allows transport oft water from beneath the bilayer stack to facilitate swelling.

We found that this GUV growth method produced a significantly lower yield and vesicles that had more membrane defects. As such, we typically employed the electroformation method to produce vesicles throughout this work, as we did not use lipid compositions and solutions that required no electric field.

2.2.2 LUVs and MLVs

Large unilamellar vesicles (LUVs) have a typical size of 100-200 nm in diameter and were produced via the freeze-thaw cycle method.[102] Briefly, lipids dissolved in chloroform were deposited in a round-bottom glass test tube and dried under nitrogen to create a film. The samples were then further dried under vacuum for 2-2.5 hours to remove any remaining solvent. The lipid films were then re-hydrated with either sucrose or water and vortexed, causing the solution of lipids to emulsify. This resulted in the formation of multi-lamellar vesicles (MLVs). This solution of MLVs was either removed from the test tubes for use in experiments, or further manipulated to produce LUVS. For LUVs, the MLV solution was alternately dipped into liquid nitrogen and a 60 °C water bath, for periods of 3 minutes each. This was repeated 10 times.

2.3 Sample preparation for observation

To prepare a sample for observation, the following steps were typically employed (unless stated otherwise in the relevant sections of Chapters 3 and 4). First, after removal from the growth chamber, the GUVs in sucrose are diluted in a 1:1 ratio with an osmotically

matched solution of glucose. The difference in refractive indices between the interior and exterior solutions results in an observable contrast in phase contrast mode, making the vesicles easier to visualise in the sample (see Fig. 2.4).

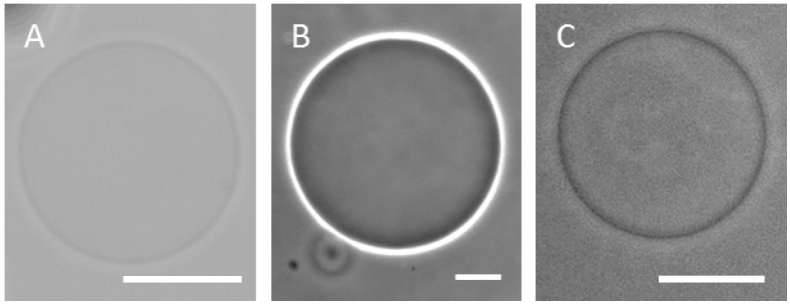

Fig. 2.4. GUVs prepared in 200 mM sucrose and diluted in 200 mM glucose. A) Viewed via bright field; vesicle contour is not as clearly defined. B) Viewed via phase contrast; the difference in refractive indices helps visualisation in this observation mode (see section 2.4.1 for further details). C) Viewed in phase contrast mode after vesicle has lost its contrast (in this case, exchange of sugar solutions through pores).

The asymmetry also causes the vesicles to sediment to the bottom of the observation chamber, greatly aiding observation with an inverted microscope. Further details on phase contrast microscopy can be found in Chapter 2.5.1. For examining interactions with particles, the particles were added to the glucose solution and typically mixed in a 1:1 volume ratio with the GUVs. The particle-vesicle solution was typically left 1 hour to equilibrate before observation. In many cases it was necessary to immobilise the sample for observation, for example when the PILs induced pore formation in the vesicles and they no longer sedimented (see Chapter 4.3.1). For this, we employed the agarose immobilisation method.[99] Low melting temperature agarose was dissolved at 0.5% w/v in a solution of glucose, where the concentration of the sugar was osmotically balanced with the external solution of the GUVs. For use, the agarose was heated to approximately 35-40 ^{o}C, at which point it transitioned from a gel to a fluid. While still fluid, it was then added in a 1:1 ratio with the pre-mixed samples of vesicles and particles and left to cool (approximately 10 minutes). At room temperature this polymer transitions back to a gel. This gelation traps the contents of the solution in a mesh-like structure (in this case, the particles and GUVs) and holds them still for observation. A schematic representation of the experimental set up can be found in Fig. 2.5.

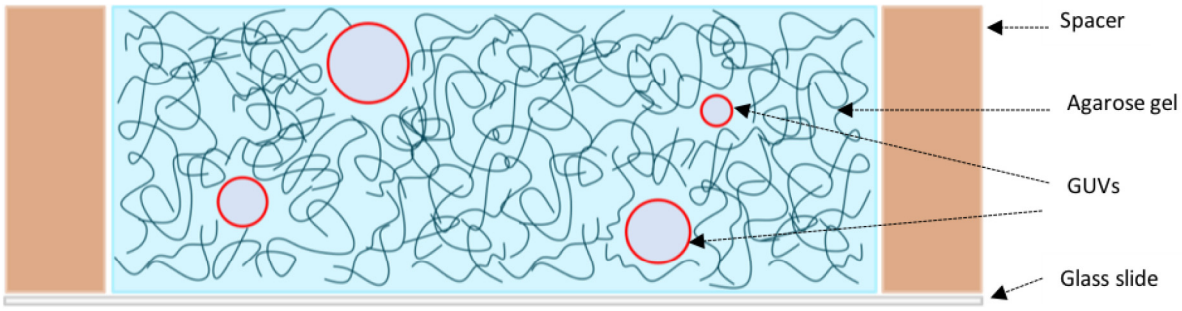

Fig. 2.5 Schematic diagram showing how agarose can be used to immobilise vesicles in an observation chamber following a protocol reported by Lira et al.[99] The agarose-glucose solution is heated before use. After mixing with the sample for observation, the solution cools and the agarose polymers form a gel mesh, holding the vesicles still at different positions in xyz.

2.4 Microscopy

Microscopy is widely utilised throughout the field of biology, among others, to understand the intricate details and features of nature. Since its first development, in the early 1600s, microscopy has evolved to have many complex components, and in turn applications, and has been used extensively in this work. Microscopy, the ability to enlarge an object so that it can be seen by the eye, depends at the simplest level on the setup of two convex lenses, the objective lens and the eyepiece/ocular. The microscope is designed in such a way that the object/specimen (of height h) is placed at distance which is greater than the focal length of the objective, F_o in Fig. 2.6. This produces a "first image" of height h_i which is larger than the original object, which then becomes the object for the eyepiece lens. The position of the eyepiece lens is such that it is closer to the first image than its own focal length, F_e. This further increases the size of the image, which is created as a virtual image in a plane which is more convenient for the eye to observe, d_i'. Further adaptations of this system, such as phase contrast and fluorescence microscopy, are described in the following sections. In this work, a number of different microscope setups are used. For phase contrast microscopy, an Axio Observer D1 (Zeiss, Germany) microscope was used, which was equipped with a Ph2 20x (NA 0.5) objective. For confocal microscopy, Leica SP5 and SP8 systems were used (Mannheim, Germany).

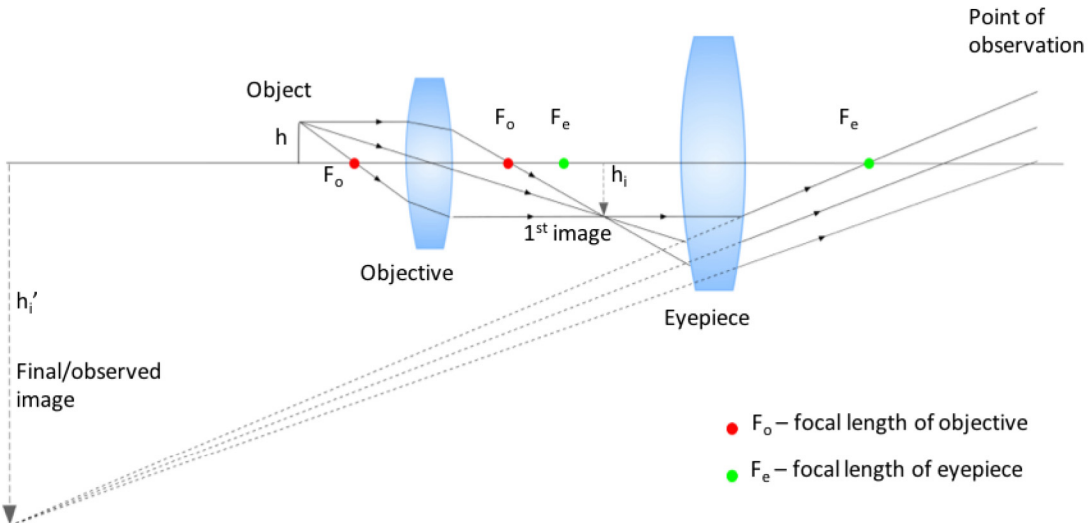

Fig. 2.6 Schematic diagram showing the basic principles of a simple microscope.

2.4.1 Phase contrast

We utilised phase contrast in this work in order to visualise non-labelled membranes. This system works in such a way as to provide contrast to colourless and transparent objects by taking advantage of the differences in refractive indices between different parts of a sample. A larger refractive index slows down the light more, creating a lag behind, or phase shift, for light waves passing through this region of the sample. However, changes in phase are not discernible by the human eye, so this is converted to changes in wave amplitude by additional components within a microscope adapted for phase contrast. In my samples, glucose and sucrose have been used to create regions with different refractive indices. The GUVs are grown in a solution of sucrose, typically 200 mM, and diluted 1:1 (by volume) into a solution of 200 mM glucose. Using sucrose inside the

vesicles also aids with observation with an inverted microscope, as the heavier inner solution causes sedimentation to the bottom of the chamber.
In the microscope, the changes in phase of the waves as they pass through the sample are converted into amplitude using a set of semi-transparent rings (see Fig. 2.7). The incident light passes through the phase annulus, a circular ring in a black field, and is condensed onto the specimen, where it is either diffracted or not, depending on the refractive indices within the specimen. The phase plate at the rear of the objective retards by λ/4 the phase of the diffracted light, and increases by λ/4 the background light, thus creating a λ/2 phase difference. When these two waves are focused on the image plane they interfere destructively, generating a darker foreground on a lighter background. This is positive phase contrast. Negative phase contrast can also be used, where instead of increasing the phase difference of the background (non-diffracted light) it is instead also retarded by λ/4 by the phase ring. When the two light waves collect on the image plane, they interfere constructively, creating areas of brightness in the region of the sample.

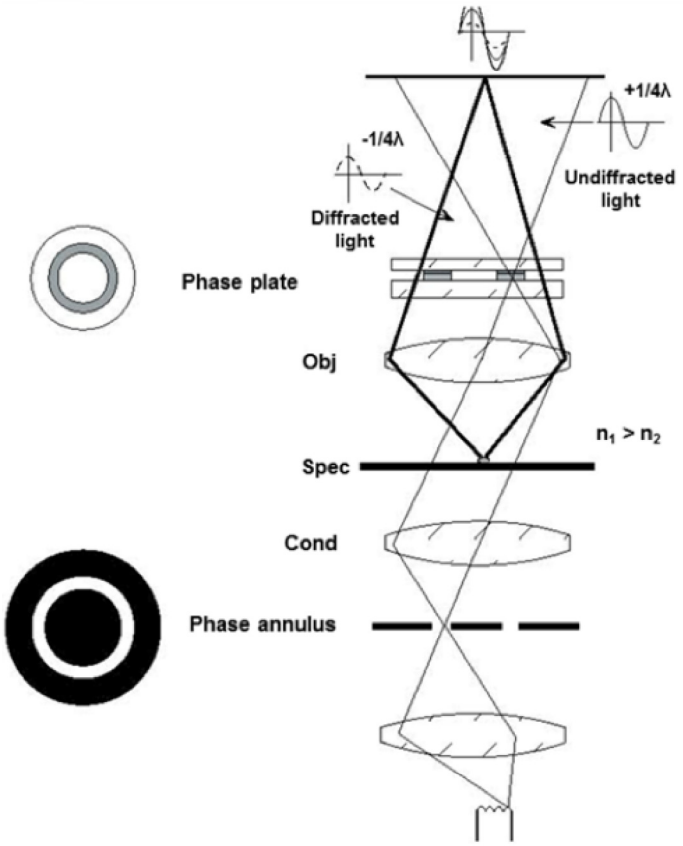

Fig. 2.7. Scheme showing the optical path during phase contrast microscopy. Positive phase contrast is shown here, where the phase annulus and plate shift the light such that the diffracted (by the sample) and non-diffracted light interfere destructively, aiding visualisation; for negative phase contrast, the phase of the non-diffracted light is instead decreased by λ/4 when passing through the phase plate so that constructive interference occurs. Adapted from [103].

2.4.2 Fluorescence microscopy

Fluorescent labelling is heavily used within microscopy studies of biological material due to its broad application and the detailed information that can be obtained about a specimen otherwise not discernible using transmitted light microscopy. In this work, four different fluorescent labels are used; two are derivatives of Rhodamine-B, one in its original configuration (see Chapters 4.2.1 and 4.2.3) and also conjugated to DPPE as a membrane dye (Rh-DPPE). NBD-PC and DiI are also used as membrane dyes. The structures of Rh-DPPE, NCD-PC and DiI have been shown previously in Fig. 2.1. In this section, the theoretical background on which the principles of sample fluorescence rely, along with the application to wide-field and confocal microscopy, will be summarised.

2.4.2.1 Theoretical background

During fluorescent imaging a sample will be irradiated with light, which contains photons of different energies, where the exact energy has a dependence on the wavelength of the light. For a sample containing the correct dye (matching the wavelength of a coherent light source for example), this incident light can result in fluorescence of the sample due to the energy transitions of electrons (as in the simplified diagram in Fig. 2.8). When an outer shell electron of an atom absorbs energy, typically in the form of light, this causes it to transition to a higher energy level (1st excited state). This is an energetically unstable state, so the electron will relax back to the ground state. It can do this via the emission of a photon, which has energy $E = hv$, where v is the frequency of the emitted photon (which has a reciprocal relationship to the wavelength), h is Planck's constant. It is this photon that is detected during fluorescence imaging, which typically has a longer wavelength (and therefore lower energy) than the excitation light. The relaxation pathways can also involve non-radiative relaxation, but these are not utilised in the imaging in this work.[104]

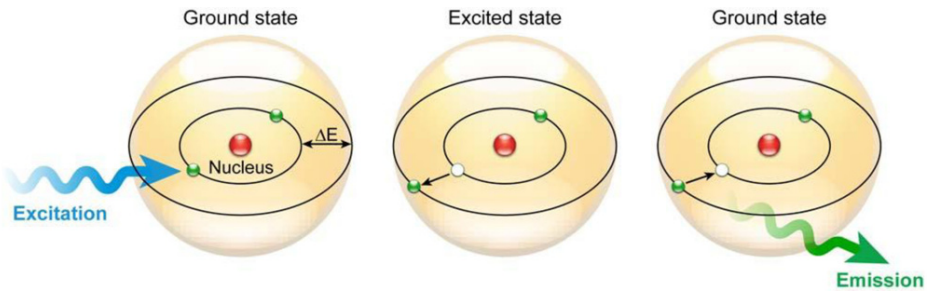

Fig. 2.8 Scheme showing the principles of fluorescence in the classic Bohr model of an atom. Light (blue) is absorbed by a lower energy electron, causing it to transition to a higher, less stable energy state. After a particular time (the fluorescence lifetime) the electron transitions back to the ground energy state and the excess energy is emitted as a photon (green). Adapted from [104]

2.4.2.2 Wide-field fluorescence microscopy

To utilise the fluorescent properties of dyes, it is necessary to adapt the setup of the microscope, as shown in Fig 2.9. Firstly, the incident light is filtered using an excitation filter, such that the light reaching the sample is of the correct wavelength to cause excitation of the fluorophore. A dichroic mirror is used to focus the filtered light onto the sample (before which it must first pass through the objective). When the light reaches the sample, it illuminates a whole region of the sample in the x, y and z directions, or in other words a "wide-field" of view. As such, when the light is re-emitted through fluorescent de-excitation, the emitted light also comes from this entire illuminated region. This is in contrast, for example, to confocal microscopy where the setup of the microscope allows only light from a specific focal point in the sample to be generated and collected. Confocal microscopy is explained in further detail in section 2.5.2.3.

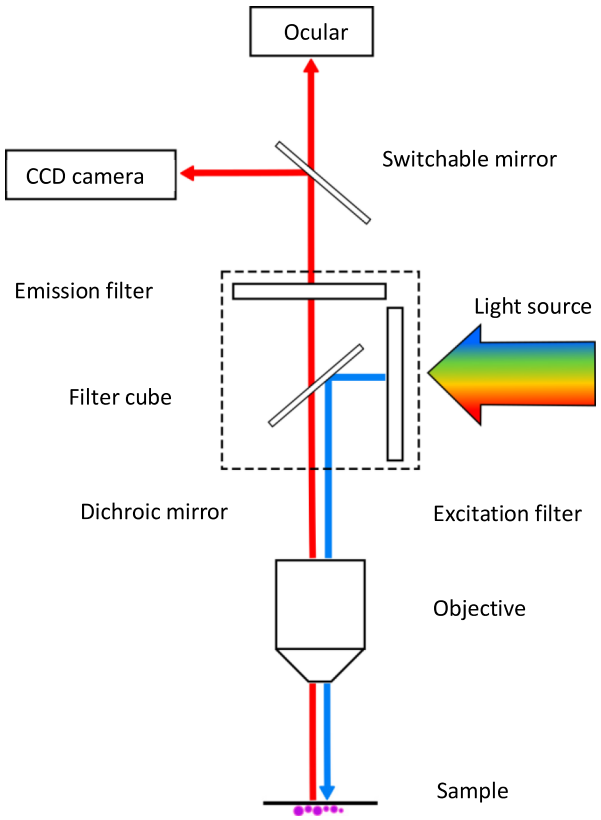

Fig. 2.9 Scheme showing the principles of the optical path for wide-field fluorescence microscopy.

When the light is absorbed by the fluorophores in the sample it is re-emitted at a different (higher) wavelength and is at a much weaker intensity than the incident light. The emission filter is therefore used to filter through only the emitted (not the incident) light, which is then directed either to the oculars or a camera, via a switchable mirror, for observation. The fluorescent parts of the specimen are then clearly visualised against a black background.

2.4.2.3 Confocal laser scanning imaging microscopy

In wide-field microscopy, the emitted fluorescent light can come from regions both in and out of the focal plane of the sample, which reduces the final resolution of the image due to increased background signal. This limitation is overcome in confocal microscopy by placing a physical barrier called a pinhole before the detector, blocking the out-of-focus light rays from the sample. This can be seen in Fig. 2.10; the green light reaches the sample and causes fluorescent emission of the dye molecules, indicated by the red regions. The dark red beams indicate the light from the desired focal planes, whereas the pale red regions indicate the light from the out-of-focus regions of the sample. The placement of a pinhole before the detector only lets through the light from the correct focal plane.

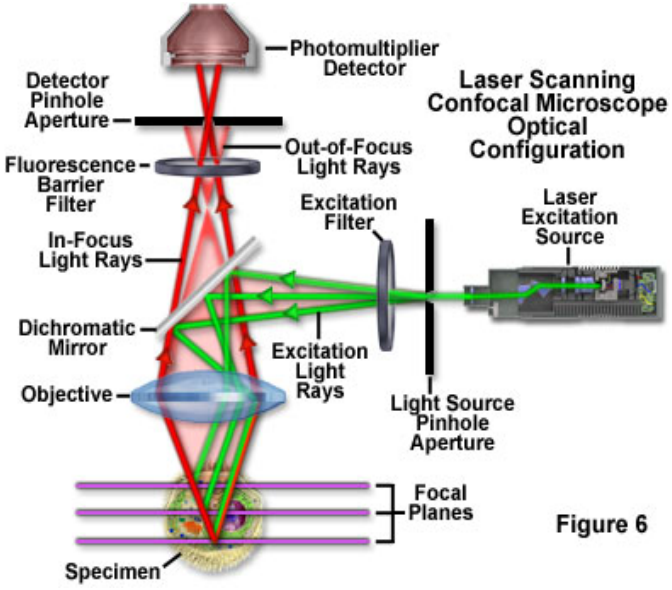

Fig. 2.10. Schematic diagram depicting the light path through a confocal laser scanning microscope (CLSM) setup. The light source is a coherent tightly focussed laser beam. It is directed onto the sample by a mirror and causes excitation of the fluorophores in the sample. The lateral size of the beam is approximately 1 mm (depending on the laser source) so the mirror is also used to scan the laser across the sample. In-focus light is detected, typically by a photomultiplier detector, and out of focus light is blocked from reaching the detector by the pinhole. An additional pinhole can also be placed after the laser source to re-focus the beam (which broadens over a distance). Figure adapted from Olympus Lifescience.[105]

Pinholes can be opened or closed to let more or less light through as desired. The usual size of the pinhole is 1 Airy unit (AU), and typically gives the best ratio of signal to noise. It is defined by the following equation:

$$d_A = \frac{1.21\lambda}{NA} = 1AU \tag{4}$$

where λ is the wavelength of the emitted light, NA is the numerical aperture of the lens and d_A is the size of the pinhole for a particular system. By using an objective with a higher numerical aperture, such as a water immersion objective with a magnification of 63×, the pinhole size can be reduced. Taking example values of $\lambda = 600\ nm$, and $NA = 1.2$ (the value for a water immersion lens), gives a value of $d_A = 605nm$. As the value of NA has the dependence $NA = n \sin\alpha$, where α is half the angular aperture of the

objective, using an immersion lens with a larger value of n (such as water or oil) is one way to increase the numerical aperture. Increasing the angular aperture of the objective (by bringing it closer to the sample) can also be used to increase NA.
In a confocal laser scanning microscope, the focussing of the laser setup is so precise that in fact the focal plane is almost more of a focal point. This focussing is a second benefit of the confocal laser scanning system over conventional epi-fluorescence microscopy, where instead a large region of the sample is illuminated at once, and photons are therefore emitted from many regions and planes simultaneously. To produce two- and three- dimensional images in CLSM, the focal point can be scanned through the sample in both the lateral and vertical directions using a set of oscillating mirrors. The lateral resolution is the lower limit of the system (smaller than the system optimised pinhole size) and is limited by the point spread function (PSF) of the point source of the emitting fluorophore. This determines the size of an object that can be resolved. Any objects smaller than this size will appear larger than they actually are. The relation is as follows:

$$d_{xy} = \frac{0.37\lambda}{NA} \tag{5}$$

where λ is the wavelength of the emitted light, NA is again the numerical aperture of the lens and d_{xy} is the minimum size of the object that can be resolved. Besides these two criteria, the properties of the image that can be obtained also depend on parameters such as the noise and sensitivity of the detector; the excitation energy of the laser; and the quantum yield of the dye (to name but a few).
Using confocal laser scanning microscopy to image fluorescent samples provides many different possibilities for obtaining information about the object in question (see Fig. 2.11). The stability and focussing ability of the laser makes experiments such as measuring membrane or solution intensities, as well as performing techniques such as FRAP, more reliable and precise. The user is also able to perform multi-channel imaging using the different laser lines, allowing one to simultaneously distinguish the components within a sample that are labelled with different dyes. This helps to understand how different elements in a sample interact with one another and their spatial arrangement relative to one another, which would only be possible in conventional widefield fluorescence microscopy with the addition of complex components and multiple cameras.
One major advantage that CLSM provides is the ability to scan through sections of a thick object, also known as optical sectioning. This provides us with information about how the object is behaving spatially and morphologically, which might not be discernible from epi-fluorescence images. Optical sectioning is used throughout this work and is explained subsequently. It is the ability of a confocal scanning laser microscope to produce a thin "slice" or section through an otherwise thick object, revealing information that might otherwise remain hidden.[106] Additionally, these thin slices when taken in the z-direction of the specimen, can be pieced together to provide a 3-dimensional image of the specimen. The entire field of view is scanned at each vertical position, to create a 2-dimensional image, and then the focus is stepped vertically up or down, using a device such as a piezoelectric driver or galvanometer device for more precise movements, or a microstepper motor.[105] An example of such optical sectioning through a GUV can be found in Fig. 2.11. Here, we see that the appearance of the GUV changes as one move

through it in the z-direction. Additionally, the 100 optical slices obtained of this vesicle can be computationally manipulated to present 3-dimensional representations of the vesicle, providing us with a clearer impression of its morphological behaviour.

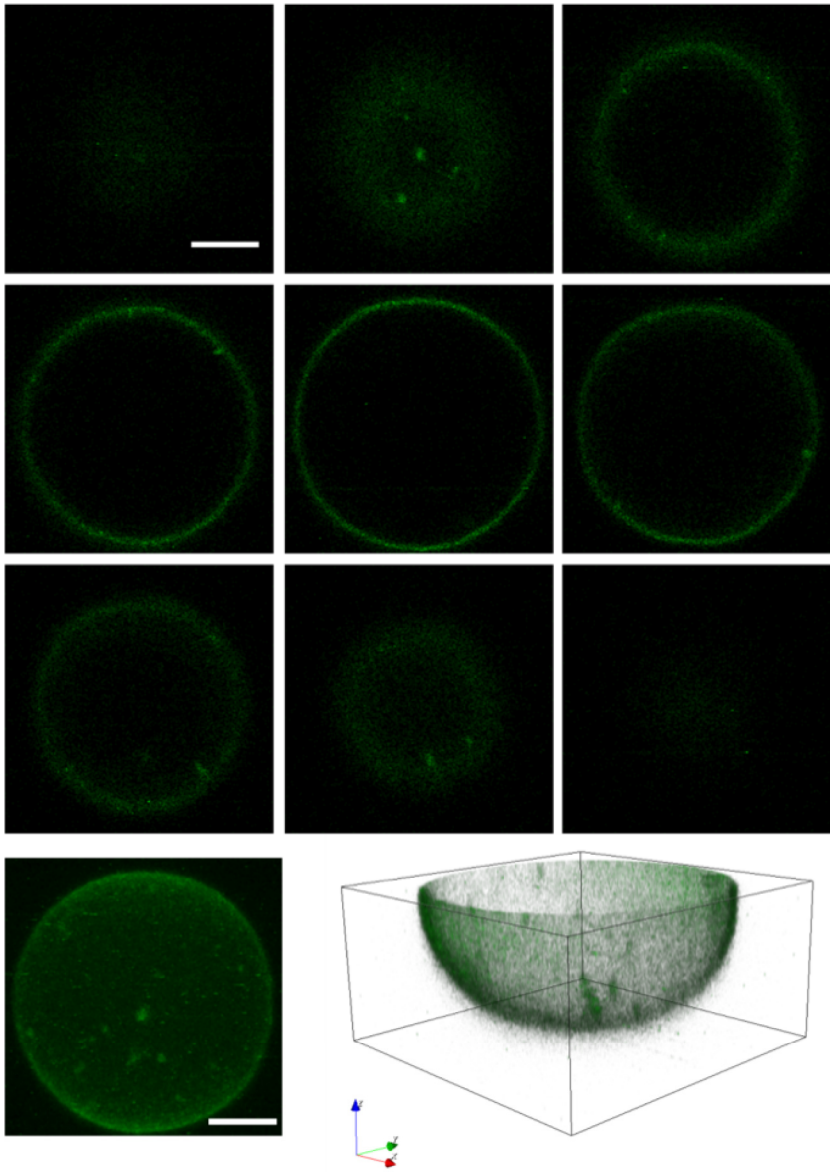

Fig. 2.11 A series of optical slices taken through a GUV and computed to produce a 3D projection and a 3D reconstruction which allows visualisation of the entire vesicle from different angles. The slices shown here are representative of the 100 total slices and in the figure; there is a distance of 2.5 μm between each frame. Changing the z-position clearly results in obtaining different information about the sample, and provides the option to re-construct to provide 3-dimensional representations of the vesicle. For example, we can more clearly see the surface irregularities in the 3-dimensional projection on the left (indicated by dots of higher intensity). The 3-dimensional reconstruction on the right (using slices 1-50, reconstructing only a vesicle hemisphere) allows visualisation of the vesicle morphology from any angle and can help conceptually with understanding the vesicle behaviour. The scale bars indicate 5μm, 3-dimensional reconstruction on right generated from slices 1-50 using image analysis software Icy.[107]

3 Effects of size of adhesive area on the interactions of biomembranes with micron sized particles

3.1 Introduction

In this chapter we examine the interactions between micron-sized particles that have both homogeneous and Janus surfaces with lipid bilayers. This work was motivated by the potential applications of such interactions (as described previously in Chapter 1.1) in fields such as biomedical imaging and drug delivery. Many studies have examined the uptake of particles by bio-membranes, both cellular and model lipid membranes.[25,28,29,50,85,108] For simplified model membrane systems, these processes depend on the competition between the different associated energies; the attractive membrane adhesion and repulsive membrane bending and tension energies. Some theoretical studies predict that the particle will occupy states of being completely free from the membrane, partially engulfed, or completely engulfed and that the stable state depends on the parameters of the system such as particle size or surface properties.[84,109] Experimental studies with GUVs and uniform microspheres have observed a number of engulfment phenomena which depend on different experimental conditions. Van der Wel et al. observed two states of particle interaction: total engulfment for membranes with low tension (as observed by the vesicle fluctuations) and adhesion to the membrane (with no engulfment) for increased tension ($\sigma > 1\,\mu N/m$).[51] Somewhat conversely, Li et al. observed full engulfment for uniform particles on membranes with both "low" ($0.05\,mN/m$) and "high" ($0.24\,mN/m < \sigma < 0.69\,mN/m$) tension.[73] States of partial wetting have also been observed for homogeneous particles by Dietrich et al. and Safarti et al. for GUVs under tension (vesicles that appeared spherical before particle adhesion).[48,74] For Janus particles with GUVs, a partially engulfed state has been observed, but again with a membrane that was under tension.[73] By using membranes that can be considered "tensionless"[109] we can evaluate the engulfment states based on the competition between membrane bending and adhesion energy as the main contributions to the interactions. This can be achieved experimentally by osmotically deflating the vesicles in a hypertonic glucose solution. We use conditions such that the reduced volume is 0.98. The reduced volume relates to the volume-to-area ratio between the surface area of the membrane and the volume contained within it according to:

$$v \equiv 3V/4\pi R_{ve}^3 \tag{6}$$

where V is the enclosed volume, R_{ve} is the radius of the equivalent spherical vesicle with that volume and v has a value according to $0 < v \leq 1$.[84] Therefore values of v that are lower than 1 corresponds to the vesicle having excess area (which can be utilised for particle wrapping).

Other experiments with Janus particles by our collaboration group observed a unique behaviour of the particles in the presence of fatty acids; the fatty acids formed capillary bridges by wetting the metallic coating of the particles, causing the particles to self-assembly into different interesting configurations.[110] Our initial experiments (data not presented here) indicated that the phospholipids did not behave in such a way as the fatty acids by sticking to the metal surface. As such, we decided to use the metal coatings as

potential regions of "inactivity" by selecting the underlying particle surface chemistry to interact with the phospholipid GUVs via electrostatics. Janus particles were produced here via metal vapour deposition on a particle monolayer, a technique that is used in the collaboration group of Prof. Velev.[111] There are many other reported methods to produce particles with two or more surfaces of different properties, such as microcontact printing (using a PDMS stamp) or molecular functionalisation on a layer of particles that are immobilised on an interface;[112–115] microfluidic approaches;[116,117] or the emulsion droplet technique[118] to name but a few. Further approaches can be found in the review by Loget & Kuhn.[119]

Here, we present the findings of preliminary investigations into the effects of particle surface properties on wetting and engulfment by GUV membranes; more specifically, how having particles with regions of different surface chemistries affects the wetting and engulfment processes. For this we use micron sized particles with a homogeneous and Janus surfaces. In the homogeneous case, we use particles such that their surface groups have an attractive electrostatic interaction with the lipid membranes. For the Janus particles, we partially coat the aforementioned homogeneous particles with a thin layer of metal so that only half of their attractive surface functional groups are exposed to the attractive lipid membranes. We prepare all GUVs in sucrose solutions and prepare particles in solutions of glucose that have a larger osmolarity than the GUVs; when the vesicles are mixed 1:1 with the particle solution, the more osmotically active external solution causes deflation of the vesicles (experimental details in subsequent section). For the particles that have a metallic coating, we use a magnetic field setup to manipulate the particles (described in section 3.2.5).

This work was performed in collaboration with Prof. Velev at NCSU and was initiated as part of a research stay at the university. As such, some time was spent learning to prepare the particle samples and how to magnetically manipulate them; these methods are described in the subsequent section of this chapter. Due to a lack of access to confocal microscopy at NCSU, the majority of the experimental observations in this chapter were performed within a short space of time upon return to Dr Dimova's group.

3.2 Materials and methods

3.2.1 Materials

Lipids and fluorescent analogues, ITO glasses, glucose, sucrose, and BSA were obtained as described in Chapter 2. 6 μm Polybead® Amino Microspheres were obtained from Polysciences (Warrington, PA). 1 μm screenCORE-Amine particles were obtained from Chemiecell (Berlin, Germany) (Excitation = 488 nm, Detection = 495 - 530 nm). 4 μm sulphate polystyrene microspheres were purchased from Interfacial Dynamics Corp. (Eugene, OR). Iron (99.95% pure) pellets were purchased from Kurt J. Lesker Co. (Clairton, PA). Chromium-plated tungsten rods were purchased from R.D. Mathis Co. (Long Beach, CA). Milli-Q water was used throughout.

3.2.2 Vesicle preparation

For the experiments in this chapter we prepared both LUVs and GUVs. The preparation methods for LUVs and GUVs has been described previously in Chapter 2.2.2 but is briefly summarised here. For LUVs, lipids dissolved at 4 mM in chloroform were deposited in a round-bottom test tube and dried first under nitrogen and then under vacuum for 2-2.5 hours. The lipid compositions were DOPC/DOPG in a molar ratio of 60/40%, and DOPC/DOTAP in a molar ratio of 60/40%. Both samples contained 0.1mol% of the fluorescent dye DiI. The films were then re-hydrated with 200 mM sucrose and vortexed, creating MLVs. The solutions were then alternately dipped in liquid nitrogen and a 60 °C water bath to produce LUVs. The LUVs were then removed from the test-tubes and further diluted in sucrose. GUVs were initially produced via the gel-assisted method, but we found that such a technique yielded growth of a poorer quality (fewer GUVs and more vesicles with defects). For the experimental data presented here, all GUVs were prepared using the electroformation technique. For this method, lipids in chloroform at 4 mM were spread on two clean ITO-coated glass slides and dried first under a stream of nitrogen and then under vacuum for 2 hours. Together with a Teflon spacer, the glass slides were assembled to form a sealed chamber, which was filled with 200 mM sucrose. The vesicles were grown by attaching the chamber to an alternating electric field, with frequency of 10 Hz and voltage of 1.2-1.6 V.

3.2.3 Particle preparation

For experiments with uniform surface chemistries the particles were first rinsed three times and then diluted in glucose. The rinsing stage consisted of diluting 10 μL of the particle stock solution in 490 μL of water and centrifuging for 5 mins at ~1500 *g*. Approximately 400 μL of supernatant was removed from the Eppendorf tube and the microspheres re-suspended in 400 μL fresh water. The most suitable dilution in glucose for the particles was initially selected by observing samples of different dilutions under a microscope.

The Janus particles for the experimental results presented here were prepared from the 4 μm sulphate-functionalised microspheres, which were prepared using the metal evaporation on a particle monolayer method, as used by Smoukov et al.[120] First, the polystyrene particles were rinsed as previously described and after removal of the last supernatant; we then added water so that the concentration of the final solution was 5% w/v. The cleaned and concentrated microspheres were then deposited on clean glass

slides using a convective assembly method developed by Prevo and Velev.[111] The schematics of the setup are shown in Fig. 3.1.

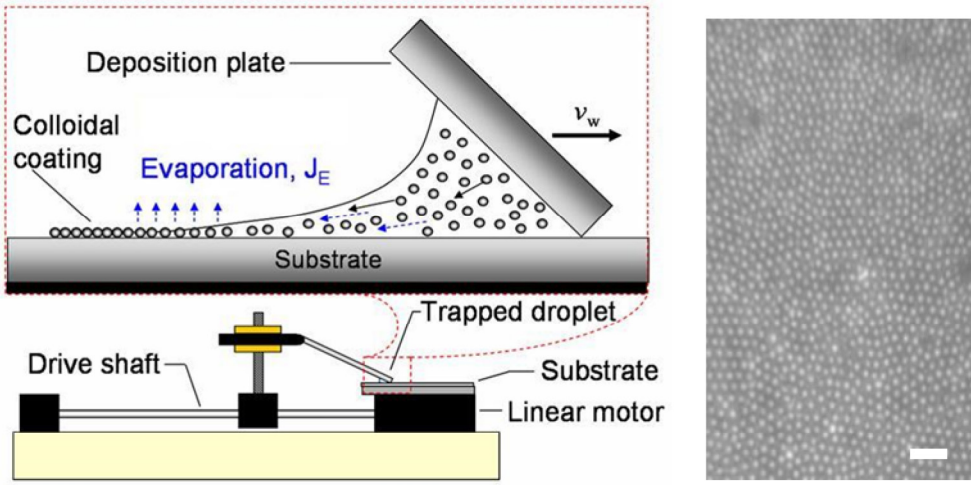

Fig. 3.1. Particle monolayer preparation. Schematic diagram showing the process of convective assembly of a particle monolayer (left) and a bright field image of the resultant particle monolayer (right), scale bar 20 μm. Schematic diagram adapted from Prevo and Velev.[111]

Briefly, 30 μL of the particle solution is injected between two glass slides that meet at an angle of 23˚; the droplet stays in the wedge between the surfaces dues to capillarity. A motor is used to drive the top glass slide across the top of the other at a speed of 10 μm/s; this drags the droplet across the glass and deposits a monolayer of particles. As the coating of particles dries, the particles in the bulk liquid are transported to the edge of the growing crystal due to the flux of the liquid which compensates for the evaporation from the crystal surface. These dried monolayers were coated first with a 5 nm layer of chromium using a metal evaporator (Cooke Vacuum Products, model FPS2-41). Next a 3 nm or 12 nm layer of iron was deposited. The thicknesses of the metals were monitored using a Maxtek, Inc. TM350 thickness monitor using SC-101 sensor crystals, which was integrated into the metal evaporator. Fig. 3.2 shows a schematic diagram of the metal evaporation process and an example SEM image of the particle surface after treatment with the metal vapour. The particles were removed from the glass surface by gentle scraping with a pipette tip.

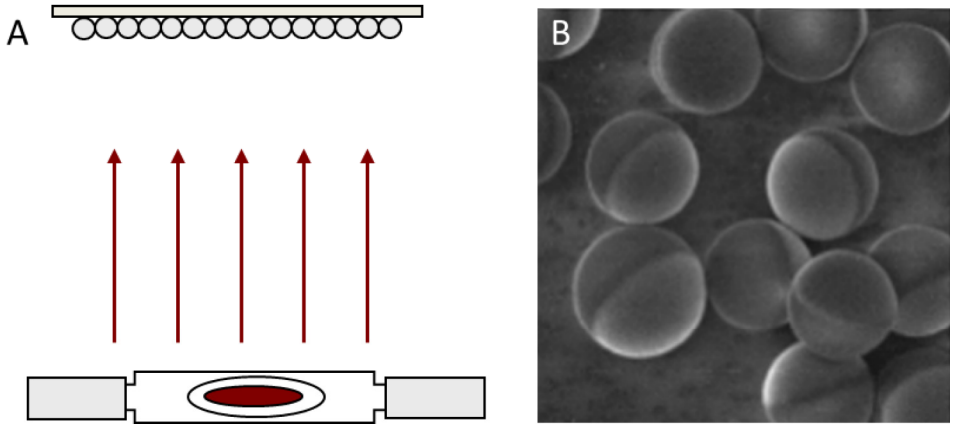

Fig. 3.2. Janus particle preparation. A) Schematic diagram depicting the deposition of metal vapour on a microsphere monolayer. B) SEM image of typical appearance of 4 μm Janus particles that we use after preparation, adapted from Bharti et al (work from our collaborative group, who have looked at other behaviours of these particles).[110]

3.2.4 Visualising vesicle-particle interactions

For the LUV experiments, after their dilution in sucrose the LUVs were mixed with different particle samples that had been prepared in osmotically matched glucose solutions. The sample was observed on a Leica SP5 confocal system after incubation for 1 hour. The affinity between the particles and different lipid compositions was qualitatively observed by the fluorescent signal from the DiI in the LUVs on the particle surfaces.

For the GUV experiments, the particle samples were prepared in glucose with a higher osmolarity than the vesicles in sucrose. This creates a hypertonic environment for the membranes; water molecules move from inside the vesicles to the region of higher sugar concentration outside, thus slightly deflating the GUVs. The solutions are prepared such that this dilution in glucose results in GUVs with a reduced volume of 0.98 (as has been introduced in Chapter 3.1). The confocal images of the particle-membrane interactions are taken using either a Leica SP5 or SP8 confocal system after incubation for 1 hour. The GUVs are labelled with DiI or Rh-DPPE (specific concentrations can be found in the relevant figures and relating text).

The confocal data displayed later in this chapter was often obtained as a series of images in the z-direction (a z-stack), a process that has been described in Chapter 2.4.2.3. A higher magnification objective (typically a 63x objective) was chosen to capture the behaviour of the membrane in the greatest details. For this objective it was not appropriate to use agarose immobilisation as this would distribute the vesicles through the entire chamber; the higher magnification objective has a shorter working distance and thus cannot image the entire volume. In some instances, the vesicle-particle configuration was moving as the z-stack was being obtained. We addressed this issue by using the StackReg plugin in ImageJ.[121] This plugin aligns a stack of images by using the previous slice as the template with respect to which the next slice is aligned; in other words, the alignment proceeds by propagation.

For the Janus particles, in addition to examining the contact between the GUV membrane and the particle surface, we also try to determine which part of the particle surface the membrane is in contact with. As we can see in the SEM image shown previously in Fig.

3.2 B, the Janus particles that we produce here have two distinct surface regions (one coated in metal, the other the surface of the underlying polystyrene particle). However, when viewed with bright field microscopy, it is not always so easy to characterise the particle surface in such a way. This depends mostly on the thickness of the metal coating. For example, in Fig. 3.3 we can see a comparison between Janus particles coated with 3 nm iron (A) compared with particles coated with 12 nm iron (B) (all particles are coated with an initial 5 nm layer of chromium before the iron is deposited). For the thicker iron coating, the Janus region of the particles is more clearly visible, as is highlighted in image C. In A it is almost impossible to determine which regions of the particles are coated with metal. Additionally, the orientation of the particle can also make it difficult to tell which region is coated in metal. Using particles with a thicker metallic coating overcomes this problem, however, doing so creates stronger inter-particle van der Waals forces and it is much more challenging to find single particles. Understanding the interactions that occur between membranes and larger, more complex particle aggregates is more challenging than modelling the particle as a simple sphere.

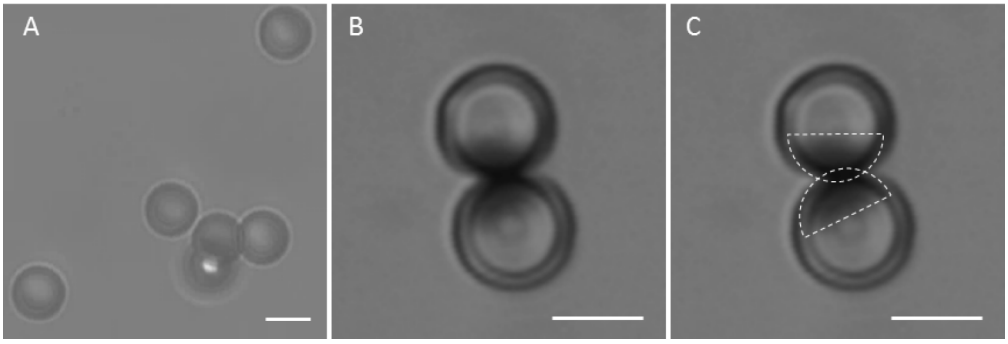

Fig. 3.3**.** Bright field images of Janus particles with different thicknesses of iron coatings. A) 4 μm Janus particles coated with 5 nm chromium and 3 nm iron. It is not possible to determine which region of the particle surface is coated with metal. B) 4 μm Janus particles coated with 5 nm chromium and 12 nm iron; metal patches are the darker regions of the particles. The particles can sometimes adhere as is shown here due to attractive van der Waals forces. C) The regions of the particles with the metallic coating in image B are approximately indicated. Scale bars = 4 μm.

3.2.5 Manipulation of Janus particles using magnetic field

The iron coating of the Janus particles means they can be manipulated in a magnetic field. A typical experimental setup is shown in Fig. 3.4. The sample containing the Janus particles (and GUVs) is placed between two electromagnetic coils. Providing current to one electromagnetic coil generates a magnetic field, with an associated magnetic field gradient. The magnetic nature of the metallic Janus coating causes the particles to move to regions of the chamber that experience a stronger magnetic field (where the field lines are denser).[122]

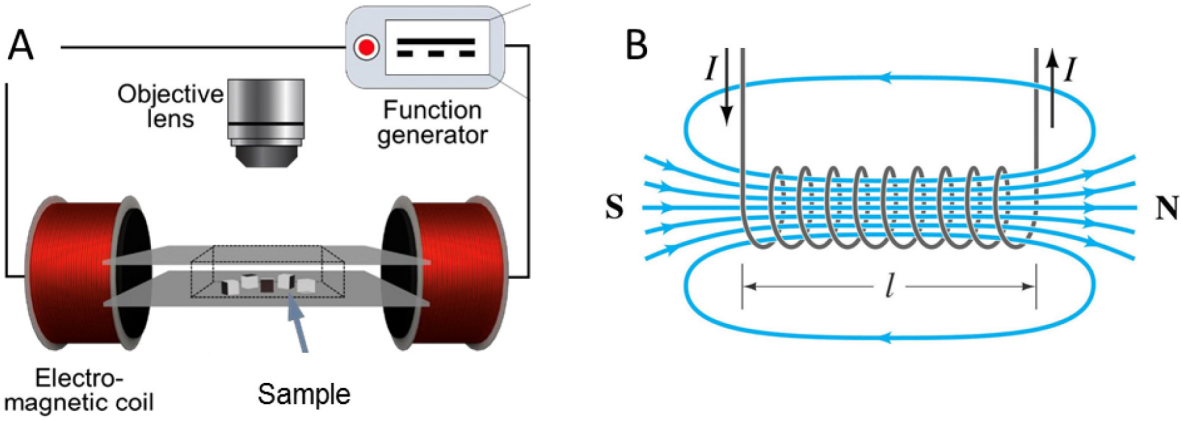

Fig. 3.4. Electromagnetic coil setup for manipulating Janus particles. A) Experimental setup. B) Magnetic field lines around electromagnetic coil; field lines are denser closer to the coil. The coil is symbolised by the grey looping lines, which correspond to the red electromagnetic coils in image A.

3.3 Results

3.3.1 LUV adhesion as an indicator of membrane-particle interaction strength

There are many classes and types of particles that can have different interactions with membranes, such as specific receptor-mediated interactions[123,124] and electrostatics-based interactions.[125] To probe the role that adhesion energies and particle sizes have on these interactions, it was first necessary to find interacting particle-membrane pairs to investigate. We did so by "screening" interactions using fluorescently labelled LUVs (~100 nm) and micron-sized particles with different surface chemistries, focussing on electrostatics as the governing force behind these interactions, by looking at the intensity from different LUV compositions on different particle surfaces. These preliminary investigations allowed us to qualitatively assess the combinations of particles and vesicles that would potentially interact on the larger scale with GUVs, from which we could then possibly observe the predicted wrapping of particles[84] by the larger vesicles and image contact angles. We prepared fluorescently labelled (red – 0.1 mol% DiI) LUVs with different lipid compositions via the freeze-thaw cycle method described previously. The LUV solutions in 200 mM sucrose were then mixed with particles of different surface chemistries and sizes in osmotically matched glucose and incubated for 1 h before observation on a Leica confocal SP5 system. The combinations of incubated particles and vesicles can be found in Table 1.

40% PG (negative) LUVs	40% DOTAP (positive) LUVs
1 μm amine (positive)	1 μm amine (positive)
6 μm sulphate (negative)	6 μm sulphate (negative)
4 μm sulphate Janus (negative + metal)	4 μm sulphate Janus (negative + metal)

Table 3.1. Combinations of LUVs and particles incubated together to "screen" for adhesive systems to later apply to GUV experiments. The surface charge is indicated in brackets. A full summary of all particles used in this thesis and further details in their properties can be found in Fig. S1.

Representative images showing the combinations of particles and vesicles that did and did not interact can be found in Fig. 3.5. From these images we conclude that the interactions between the particles and the LUVs have a strong dependence on electrostatic interactions. For example, the positively charged amine-functionalised particles in panel A have fluorescently labelled 40% PG LUVs adhere to them, where these LUVs are negative. Similarly, for the negatively charged sulphate-functionalised particles in panel C, these show a strong interaction with the positively charged 40% DOTAP LUVs. The inverse is also the case, an example of which is shown in panel B; the positive amine particles do not have positive DOTAP LUVs adhered to them. From these initial "screening" experiments, we determined particle-vesicle combinations which are more likely to interact when we use GUVs to look at particle wrapping and engulfment. One can clearly see from the example given in Fig. 3.5 that these interactions have a strong dependence on electrostatics, with oppositely charged particles and membranes adhering to one another (and those with like charge not). When we look at the LUV coverage for the Janus particles, where half of their surface is negative sulphate groups and half is metal, we do not see coverage to the same extent as for the sulphate particles with no metal coating.

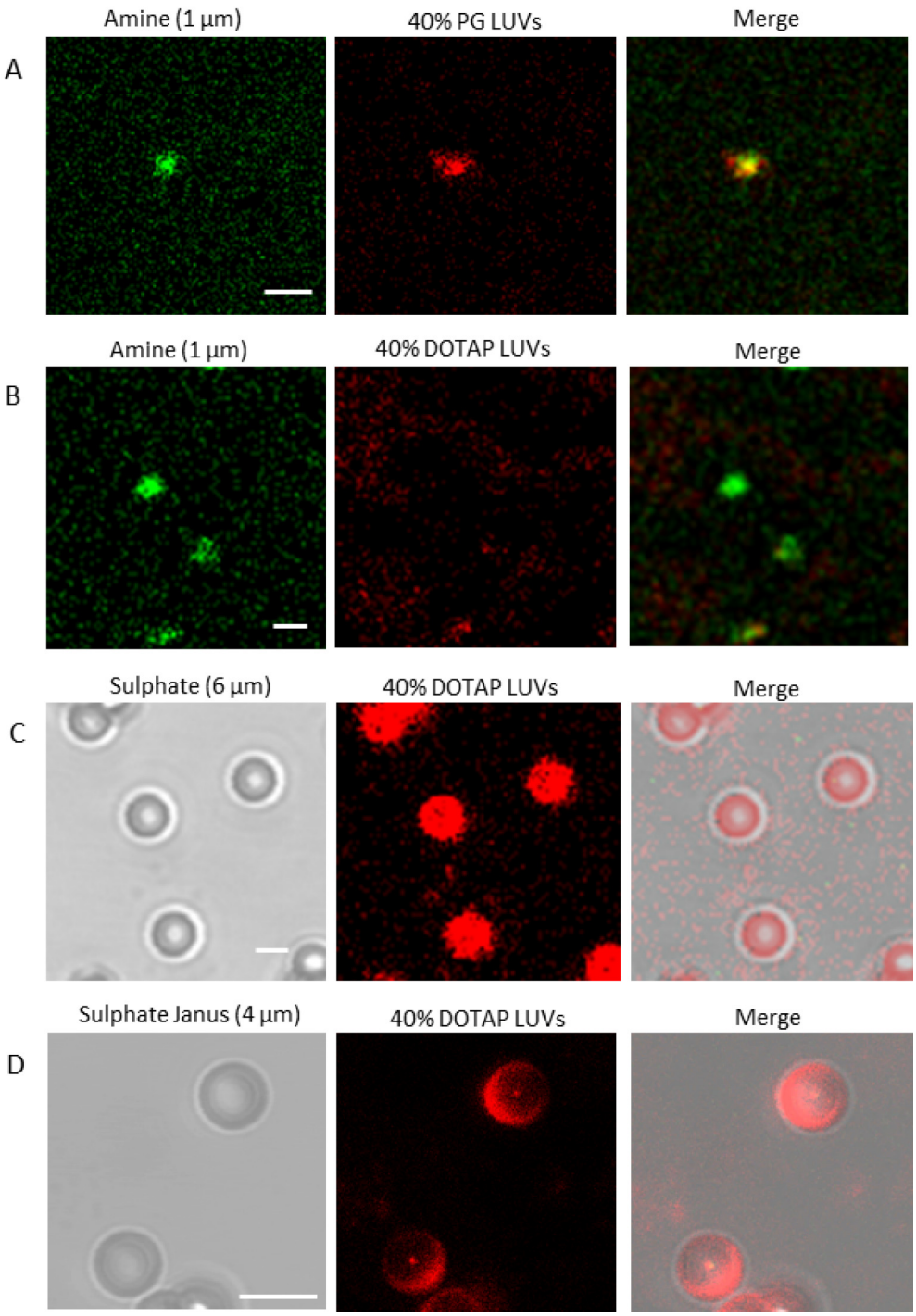

Fig. 3.5. Affinity between different lipid compositions and particle surfaces as assessed by fluorescently labelled LUVs. A) Co-localisation of fluorescent signal from 40% DOPG LUVs (negative) on surface of 1 µm amine particle (positive). B) No 40% DOTAP LUVs (positive) on 1 µm amine particle (positive). C) Co-localisation of signal from 40% DOTAP LUVs on 6 µm sulphate particle surface (negative). D) Sulphate Janus particles (negative/iron) partially coated with 40% DOTAP LUVs (positive).

Due to the nature of the particles, specifically the thickness of the metal coating (the thickness of the iron here is only 3 nm, see Fig. 3.3, and section 3.2.4), it is not possible to determine from these images whether the location of the LUVs is on the non-metal part of

the particles' surface or not. Nonetheless, this partial coverage does indicate that the adhesion of the GUVs to the particle surfaces might also follow such behaviour.

3.3.2 Particle properties dictate the extent of engulfment by GUVs

From the previous LUV "screening" experiments, we were able to deduce combinations of particles and vesicles that adhere to one another and conclude that these interactions primarily depend upon electrostatic forces. We then applied these findings to experiments with particles and GUVs by using oppositely charged particles and vesicles.

We first examined the interactions between DOPG containing GUVs (negative) with amine-functionalised 1 μm particles (positive). The GUVs were prepared in the lipid ratio 60/40 % DOPC/DOPG in 200 mM sucrose via electroformation and incubated for 1 h with the amine particles that had been prepared in 210 mM glucose (hypertonic solution for osmotic deflation, see earlier section 3.2.4). The glasses were first passivated with 0.2 wt% BSA (prepared in 200 mM glucose) to avoid adhesion of the positively charged particles or vesicles to the glass. In Fig. 3.6 we can see a typical interaction between this combination of particles and vesicles. We observed the complete wrapping of these particles by the GUV membrane upon contact. Fig. 3.6 is a reconstructed image in the z-direction, produced from many confocal cross-sections of a GUV volume. Due to the assumptions made by the image analysis software that the voxel is cubic (i.e. takes the distance between the slices of the vesicle contour to be the same as pixel size), the image reconstructions show the vesicle with a more elongated appearance in the z-direction. The differences between the refractive indices of the sample and the immersion objective can also play a role in this aberration.[126] The particle is fluorescently labelled which allows us to visualise its position just inside the vesicle volume, completely wrapped by red-fluorescent membrane. This complete wrapping and internalisation of the particle indicates that for this combination of particle and vesicle, the adhesion energy is strong enough to overcome the repulsive force of the bending energy of the membrane. However, we can see that in the region of the particle there is excess membrane area. This could mean that the energy limitations imposed by the tension in a quasi-spherical vesicle perhaps did not need to be overcome for wrapping to occur; there could have been an external membrane tube or defect that facilitated the engulfment.

We then went on to examine the interactions for larger particles, so that the contact between the membrane and the particle surface could be more easily distinguished. Figure 3.7 shows a representative interaction that was observed between 6 μm amine-functionalised polystyrene particles and 40% PG doped GUVs. From the reconstructed XZ and YZ images in A) and B), one can see a particle (green) located at the edge of a (red) GUV membrane, which curves around the contour of the particle. By taking a closer look at this section of membrane in the region of the particle, in images E-H), we can see more closely the bend of the membrane as it comes into contact with the particle. The 3-D reconstruction in H) also helps to visualise the slight protrusion that the particle makes towards the vesicle interior. This behaviour indicates that there is an attractive interaction between the particle and membrane, as the membrane bends in the opposite direction from its preferred spherical curvature, so as to increase contact area with the particle. However, the fact that these particles are not fully engulfed indicates that the adhesion energy is not great enough to overcome the energy limitation imposed for such a process by the bending elasticity of the membrane.[127]

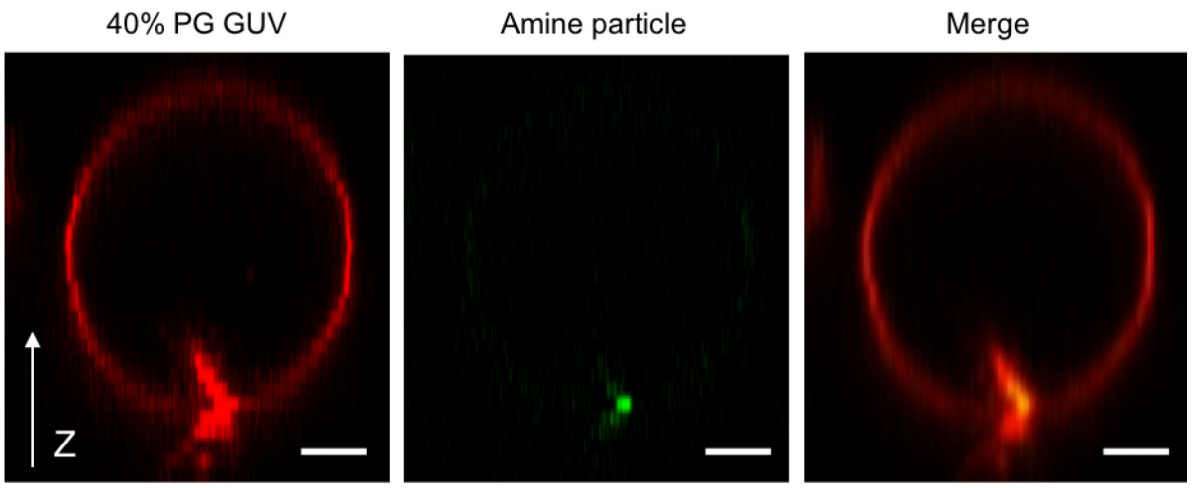

Fig. 3.6. 1 μm amine-functionalised (positive surface charge), green fluorescently labelled polystyrene particle wrapped by a 40% PG GUV (0.1 mol% Rh-DPPE). The images are obtained from confocal z slices through a GUV volume, which have been reconstructed to show the "side" view, with the z direction indicated. The red channel shows the fluorescence from the membrane and the green channel shows the fluorescent signal from the particle. The third image is a merge of these channels, showing the co-localisation of the two fluorescent signals, indicating that the particle is wrapped by membrane.

For the same combination of particles and vesicles, we also observed interactions where the behaviour of the membrane in the vicinity of the particle surface was not so clearly displayed, an example of which can be seen in Fig. 3.8. Here, we see the 6 μm amine-functionalised particle in close contact with the vesicle membrane, which is displayed at three z positions through the GUV volume. As we travel in the positive z-direction from the particle equator in A), we see that in the region of the particle the membrane intensity seemingly decreases, or the confocal microscope somehow does not detect fluorescent signal from this region (the red channel images in images B and C). We know from previous experiments, shown in Figs 3.6 & 3.7, that this combination of particle functional groups (amine) and vesicle composition do interact, in the form of full or partial wrapping by the membrane. As the setup of the confocal microscope means that the sample is scanned with a laser from below and the signal also detected from below, the decrease in fluorescent signal could be due to a partial blocking or scattering of the light by the polystyrene particle (i.e. the portion of membrane directly above the particle is not reached by the laser). The presence of the surface groups on the particle could perhaps also influence the distribution of the membrane dye, by exclusion of the dye from the area of the membrane in contact with the particle either via repulsive interactions with the dye, or by attraction of more negatively charged DOPG lipids to the positively charged particle surface. As the degree of particle engulfment has a dependence on the adhesion energy between the particle and vesicle, we tried increasing the percentage of the negatively charged lipid DOPG to 100%.

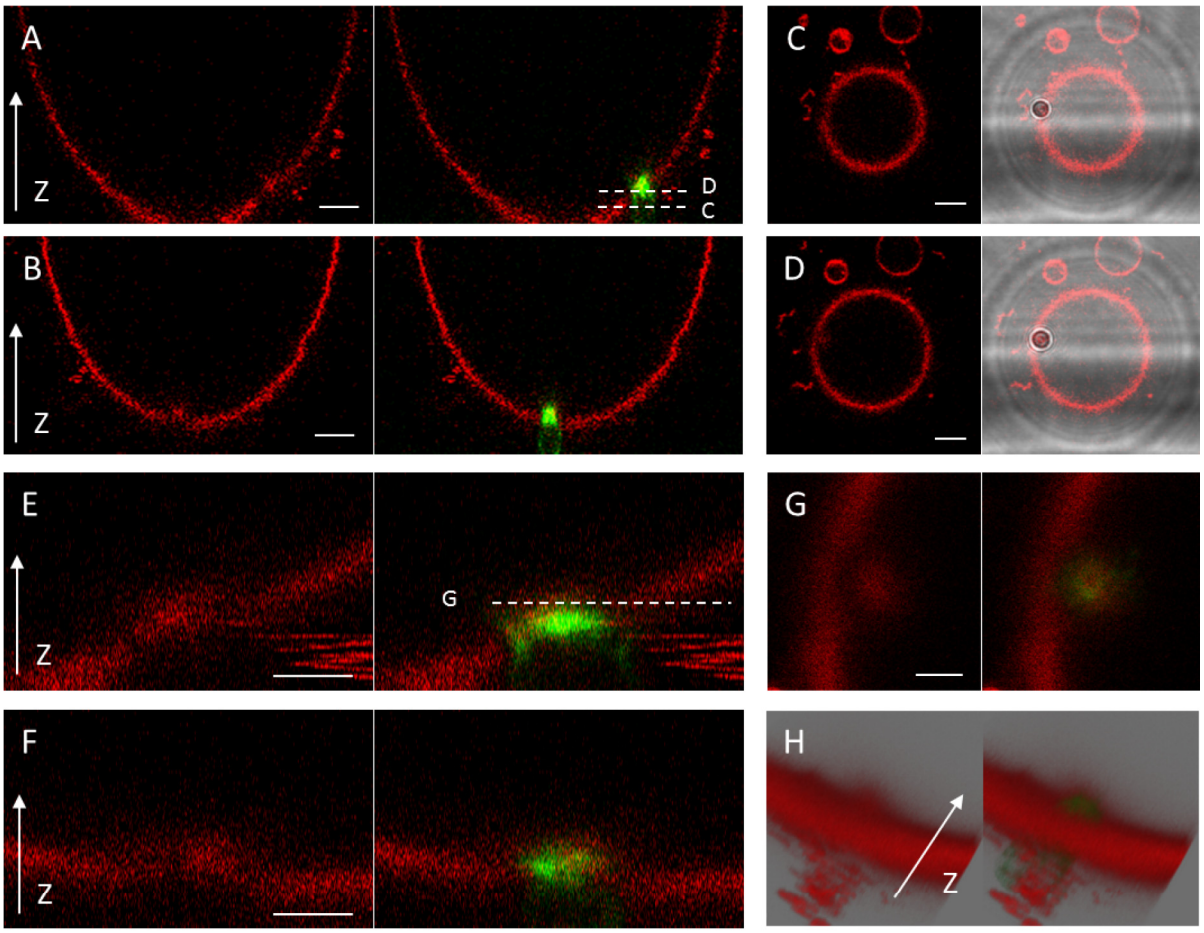

Fig. 3.7. 6 µm amine-functionalised polystyrene particle (positive) in contact with a 40% PG (negative) GUV (0.1 mol% Rh-DPPE). A) and B) are reconstructed cross-sections in the XZ and XY planes, obtained from multiple z-slices through the GUV volume. In the vicinity of the particle (green) the membrane (red) partially bends around the particle. C) and D) show XY cross sections at the indicated Z-positions through the sample, showing the behaviour of the membrane at different positions. E) XZ reconstructed cross-section zoomed in to region in contact with particle. F) YZ reconstructed cross-section of the same zoomed-in region. G) Confocal cross-section at highlighted z-position in E, showing the small coating of membrane at the top of the particle. H) 3D reconstruction from z-slices in E) and F), showing the small membrane bend around the particle towards the vesicles interior. Scale bars 10 µm images A-D, 5 µm images E-G.

However, even at this percentage of negative lipid, we did not see full engulfment of the particle by the membrane for the 6 µm particle size. As such, we decided to look at the interactions for the same surface charges but in an opposite configuration: negatively charged particles with positively charged GUVs. In the LUV screening experiments, we had tested the combinations of particles and vesicles using a lipid composition of 40% of the positively charged lipid species, DOTAP. However, to produce GUVs with this amount of DOTAP is experimentally challenging.[98] We started with a low percentage of DOTAP (5%); if interactions already occurred at this concentration, it would not be necessary to spend time developing methods of GUV production for a more positively charged composition.

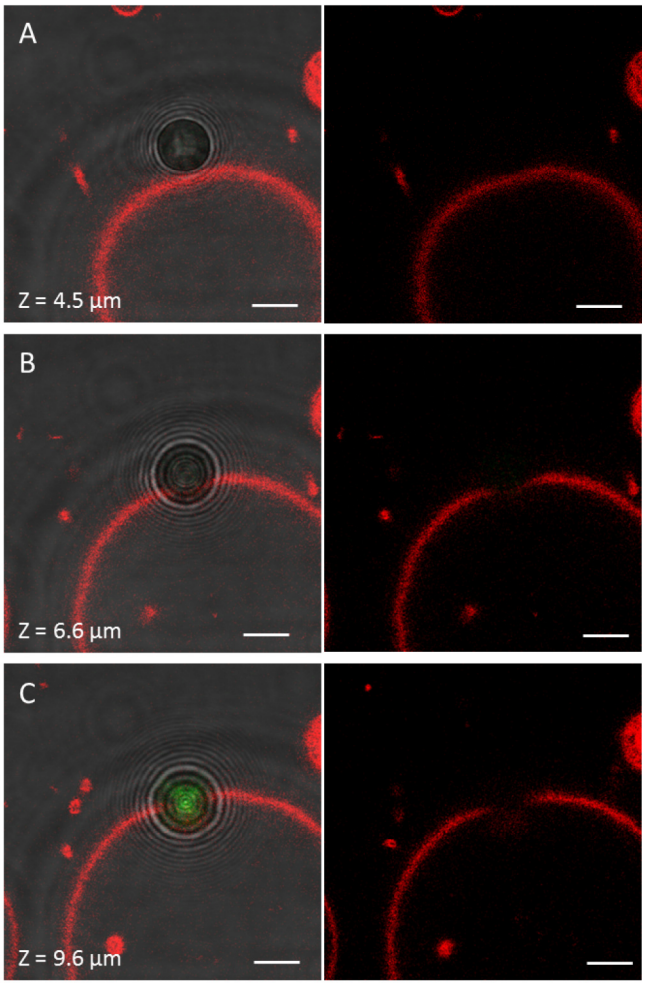

Fig. 3.8. Confocal cross-sections at different z-position for a 6 µm sulphate-functionalised particle at the surface of a 40% PG GUV. A) Cross-section at the equator of the particle, where the z positions refers to the distance above the bottom of the vesicle. B) Cross-section at z = 6.6 µm, showing the decrease in membrane intensity close to the particle surface. C) Cross-section at z = 9.6 µm, again showing how membrane fluorescent intensity behaves close to particle surface. Scale bars 5 µm.

We prepared GUVs with the composition 95/5 % DOPC/DOTAP via electroformation, with the small experimental adjustments described in the Methods section of this Chapter. These GUVs were then incubated with 6 µm sulphate-functionalised polystyrene particles, where the sulphate groups produce a negative surface charge. Fig. 3.9 shows a typical interaction between particles and membranes of these compositions. We can see in this figure that the particle (most clearly visualised in bright field image E) is completely wrapped and internalised by the GUV. In image A, a XZ reconstruction from many z-slices, we can see the membrane which has the configuration of a main vesicle body, at the centre of which sits a fully wrapped particle. From other confocal slices (data not shown) one can see that the vesicle has retained its contrast, so the engulfment of this particle did not involve the formation of pores to facilitate the change in surface area to volume ratio.

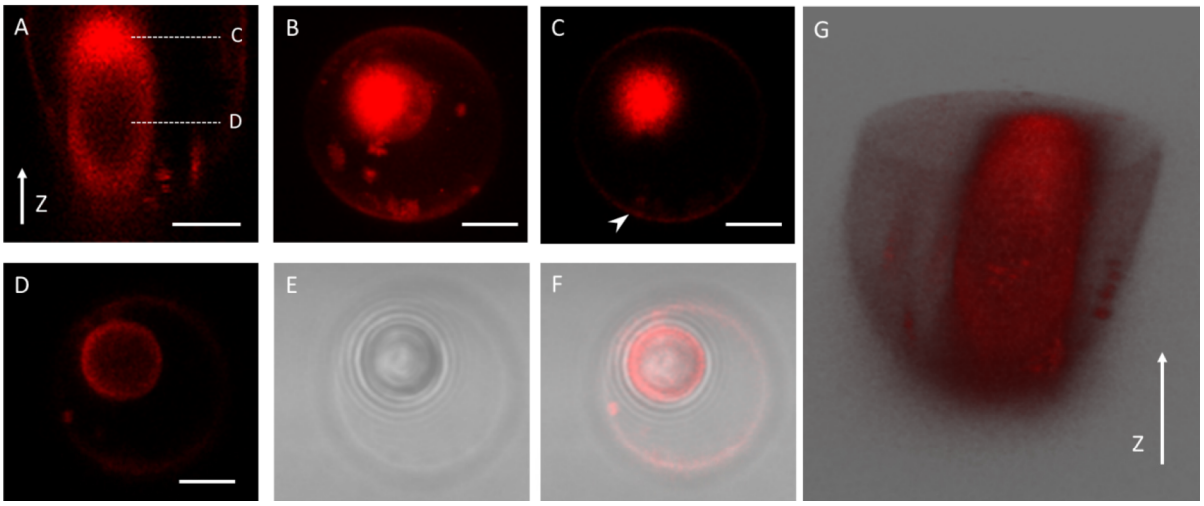

Fig. 3.9. 6 μm sulphate-functionalised (negative surface charge) polystyrene particle internalised by a 5% DOTAP GUV (0.2 mol% DiI). A) A reconstruction of the "side" view of the particle-vesicle configuration from confocal z slices, showing the particle coated in lipid material located at the centre of the vesicle; the labels C & D indicate the position in the z direction of individual slices shown in the respective images. B) 3D projection of the z-stack images. C) Confocal cross-section at the mid-plane of the vesicle, corresponding to the "top" of the particle, coated in lipid. Vesicle contour is very faint and thus indicated by arrow. D) Confocal cross-section at the mid-plane of the particle. E) Bright-field image showing particle more clearly, at same z-position as D. F) Merge of images D & E. G) Reconstruction of the z-slices to create one image showing all dimensions simultaneously. Scale bars 5 μm.

As one can see in this figure (Fig. 3.9), there are several membrane defects and tubes on this vesicle; other such defects could have provided the excess area required for the particle engulfment without need for membrane pores. Such membrane defects were observed throughout the population of 5% DOTAP vesicles. For this combination of particles and vesicles, all interactions involved total engulfment of the particle by the membrane for the cases where the vesicle was larger than the particle; however, we did not always observe internalisation of the particle. An example of this is shown in Fig. 3.10, where the particle is fully engulfed but the majority of the particle body sits outside of the main GUV structure. Due to the apparently strong affinity that this combination of particle and the vesicle have for one another, this particular interaction in Fig. 3.10 could have involved vesicle pore formation. This would reduce the vesicle volume to compensate increase in vesicle surface area that is used up due to spreading over the particle. After this pore formation the membrane could then spread over the outer most particle surface while resealing, which would account for the regions of dense lipid where the membrane covering the particle meets the membrane of the main vesicle structure. Pore formation seems likely in the case of the vesicle shown in Fig. 3.10 as it is very difficult to discern the membrane contour in the bright field images. For vesicles that retain their contrast (i.e., have not exchanged internal and external solutions), one can typically resolve the vesicle contour in bright field much more clearly than this. An example of a vesicle viewed in bright field mode with sugar contrast preserved is shown in Fig. S2. In Figs 3.9 and 3.10 we also observe an apparent increase in intensity for the regions of the membrane that wraps the particles. This was also the case for small vesicles that adhered to particles, as can be seen in Fig. 3.11; in the region of the membrane where

the vesicle is adhered to the particle, the membrane intensity is qualitatively much higher than for the rest of the vesicle. These effects could also be due to the membrane being more than 1 bilayer thick in these regions; we do not know the full history of the interaction. Indeed, we do not know the full history of the particle before the interaction either; it could be that it has collected other fluorescent free lipid "dirt" in the sample before interacting with this GUV. Alternatively, such strong fluorescent signal could also be as a result of dye accumulation on the particle, as the particle surface has negatively charged functional groups and DiI is a cationic dye.

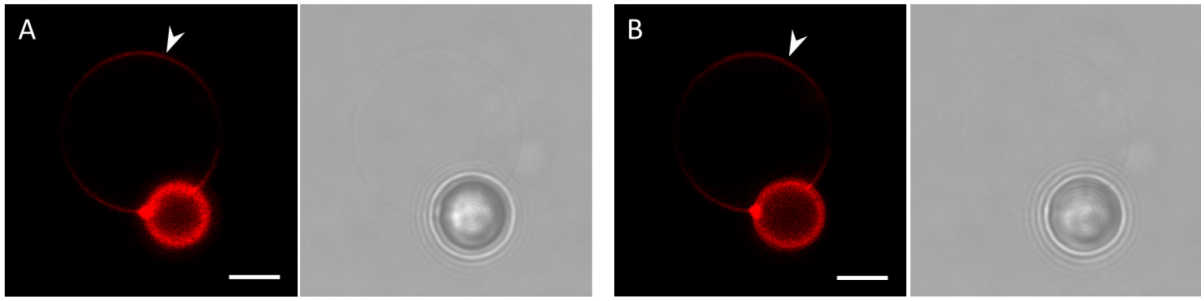

Fig. 3.10. 6 μm sulphate-functionalised (negative surface charge) polystyrene particle fully wrapped by a 5% DOTAP GUV (0.2 mol% DiI) shown at two different z-positions. A) Confocal cross-section and bright field image at vesicle equator. B) Confocal cross-section and bright field image at particle equator. The white arrows indicate the faint GUV contour. Scale bars 5 μm.

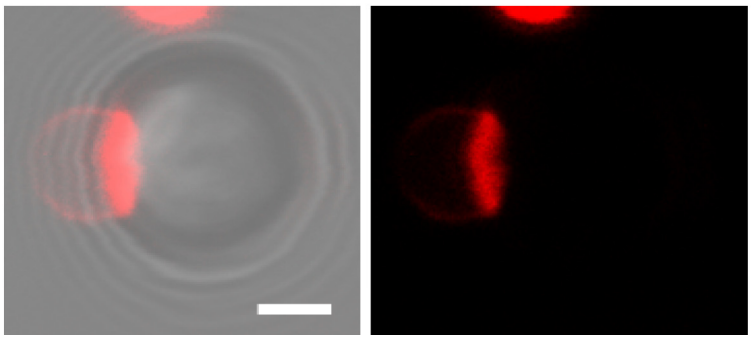

Fig. 3.11. 6 μm sulphate-functionalised (negative surface charge) polystyrene particle with an adhered 5% DOTAP GUV (0.2 mol% DiI). The intensity of the membrane in the region where it adheres to the particle qualitatively appears brighter.

3.3.3 Janus particles' interactions with the membrane demonstrate a pinning of the contact line

To probe the effect that a non-uniform surface chemistry can have on particle-membrane interactions, we produced Janus particles with a thin metal coating (<25 nm) on half of their surface (the fabrication process has been explained previously Chapter 4.2.3). We had previously seen how particles with a uniform surface behave when in contact with a membrane; for positively doped (DOTAP) membranes, we observed complete engulfment of negatively (sulphate) charged particles, while for membranes with a negative charge (DOPG) we observed engulfment of smaller positive (amine) particles but only adhesion to the membrane for larger positive (amine) particles. As such, we decided to use Janus particles where the non-metal portion of the sphere were the sulphate functional groups, as we knew that this combination of particles and vesicles interact strongly (as we see full wetting and engulfment). We incubated these particles with DOTAP doped GUVs and observed the subsequent interactions with confocal microscopy.

First, we looked at 4 μm Janus particles (half metal, half sulphate functional groups) with 5% DOTAP GUVs and observed two main types of interactions. In all cases, the particles' surfaces were only partially coated in lipid material. However, these partially wrapped particles were located both outside and inside the vesicle main body. An example of one such partially wrapped Janus particle is shown in Fig. 3.12. The 3D projection from multiple confocal slices is shown in images A-C, which shows the intensity from the lipid membrane only on part of the surface. The wrapped region of the particle corresponds with the still-exposed negative sulphate groups on the particle surface (the metal coating is the darker region). The XZ reconstruction in D and E also helps to visualise how the membrane partially spreads over the particle's surface. We previously discussed the possibility of the particle "blocking" the excitation of the fluorescent molecules in the membrane in relation to Fig. 3.8 (as the illumination is from the below and the excitation light possibly cannot reach the membrane through the particle). However, if we look at the region of Fig. 3.12 indicated with a white star, we can see that there is fluorescent signal from the membrane at the region directly above the surface of the particle; as such, we can conclude that in this instance the presence of the particle is not responsible for the lack of signal where we suppose the metallic portion of the particle is situated.

We observed further instances of this partial wetting and engulfment, such as in Fig. 3.13. At one particular z-position shown in images A and C, the particle partially extends into the vesicle main body and the membrane wraps around the contour of the particle. Image C indicates that the sulphate region of the particle (the lighter region) is the part that is in contact with the membrane. One should also note the regions of higher fluorescent intensity on the particle surface. This could indicate that the adhesion and partial engulfment was facilitated by existing sites of membrane defects (potentially providing excess area), or that multiple bilayers were generated during the engulfment process itself. It could also be a further indication of dye accumulation on the particle surface, as discussed previously. This latter process could proceed as follows: due to the high affinity between the sulphate region of the particle and the membrane, the membrane quickly spreads over the particle surface, increasing the membrane tension due to an increase in the surface area to volume ratio. The tension can then be reduced via pore formation, to

reduce the internal volume. Due to the typically high edge tension of membrane pores,[91] this pore would quickly re-seal and the membrane could come back together in multiple layers, producing these regions of higher intensity around the particle that we see here.

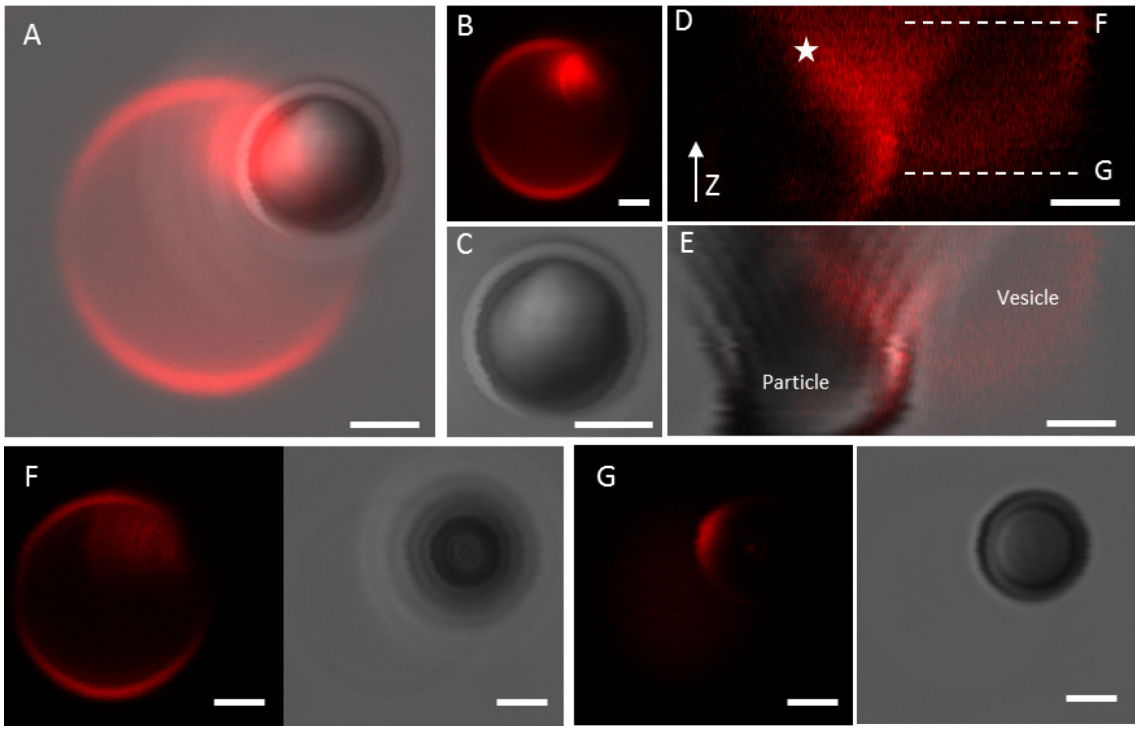

Fig. 3.12. 4 μm sulphate-functionalised (negative surface charge) polystyrene/metal coated Janus particle partially wetted by a 5% DOTAP GUV (0.2 mol% DiI). A) 3D projection for overlay of cross-sections through GUV and attached Janus particle. B) 3D project for fluorescent signal from membrane only. C) 3D projection of brightfield images of Janus particle (zoomed in) showing the metal coating as the darker region of the particle surface. D) XZ reconstruction from z-slices through GUV volume showing partial wetting of the membrane in the region of the particle E) Previous reconstruction overlaid with bright field to show particle location. Labels indicate particle and vesicle locations. F) Confocal slice at indicated z-position in D. G) Confocal slice at indicated z-position in D. Scale bars 2 μm.

We also observed instances where the Janus particles were partially wetted by lipid on their surface but internalised to the interior of the main vesicle body, such as in Fig 3.14. The XZ images in A and B demonstrate both that the membrane does not cover the entire particle surface and that the entire particle sits inside the GUV. The latter point can for example be compared to the configuration in the previous figure, Fig. 3.13, where part of the particle is still outside the main body of the vesicle. Again, for the fully internalised particle in Fig. 3.14, we see that the particle surface is a site of many membrane defects, which could have either facilitated the wrapping of the particle or been produced during the process, as previously discussed for Fig. 3.13.

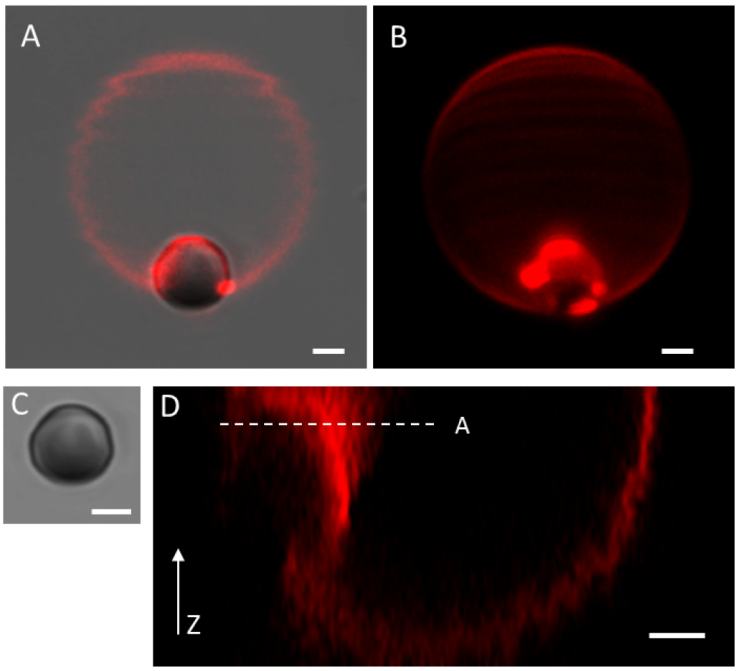

Fig. 3.13. 4 µm sulphate-functionalised (negative surface charge) polystyrene/metal coated Janus particle partially wetted by a 5% DOTAP GUV (0.2 mol% DiI). A) Confocal cross-section at equator of particle, showing pinning of contact line. B) 3D projection from multiple z-slices for the fluorescent intensity from the GUV membrane. C) Bright field image at equator of particle showing the darker region coated by metal. D) Reconstructed XZ image through the vesicle volume, indicating that the particle only sits partially inside the vesicle volume. Scale bars 2 µm.

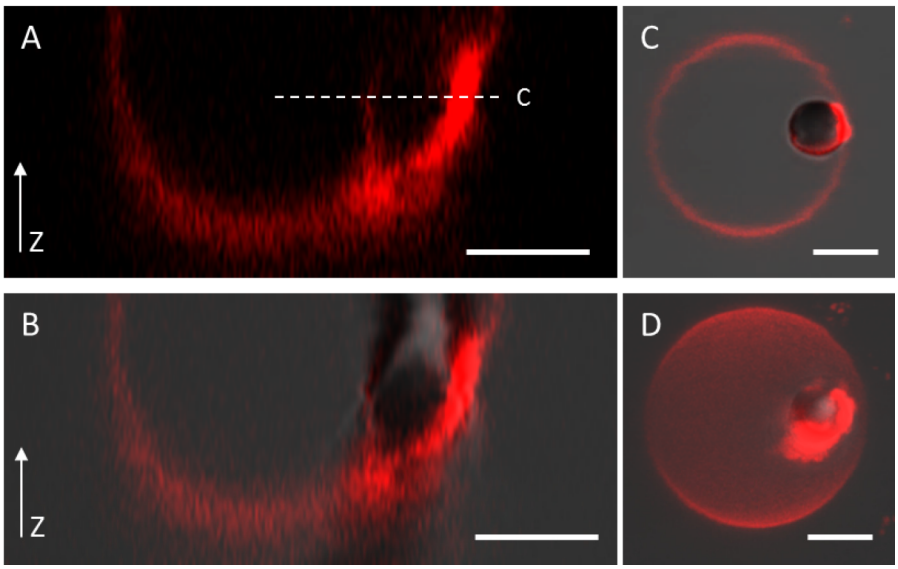

Fig. 3.14. 4 µm sulphate-functionalised (negative surface charge) polystyrene/metal coated Janus particle partially wetted and internalised by a 5% DOTAP GUV (0.2 mol% DiI). A) XZ image through vesicle volume reconstructed from multiple cross-sections, showing the Janus particle partially coated in membrane and sitting inside the vesicle volume. B) As previous, with bright field overlay. C) Cross-section at z-position shown in A. D) 3D projection from multiple confocal cross-sections.

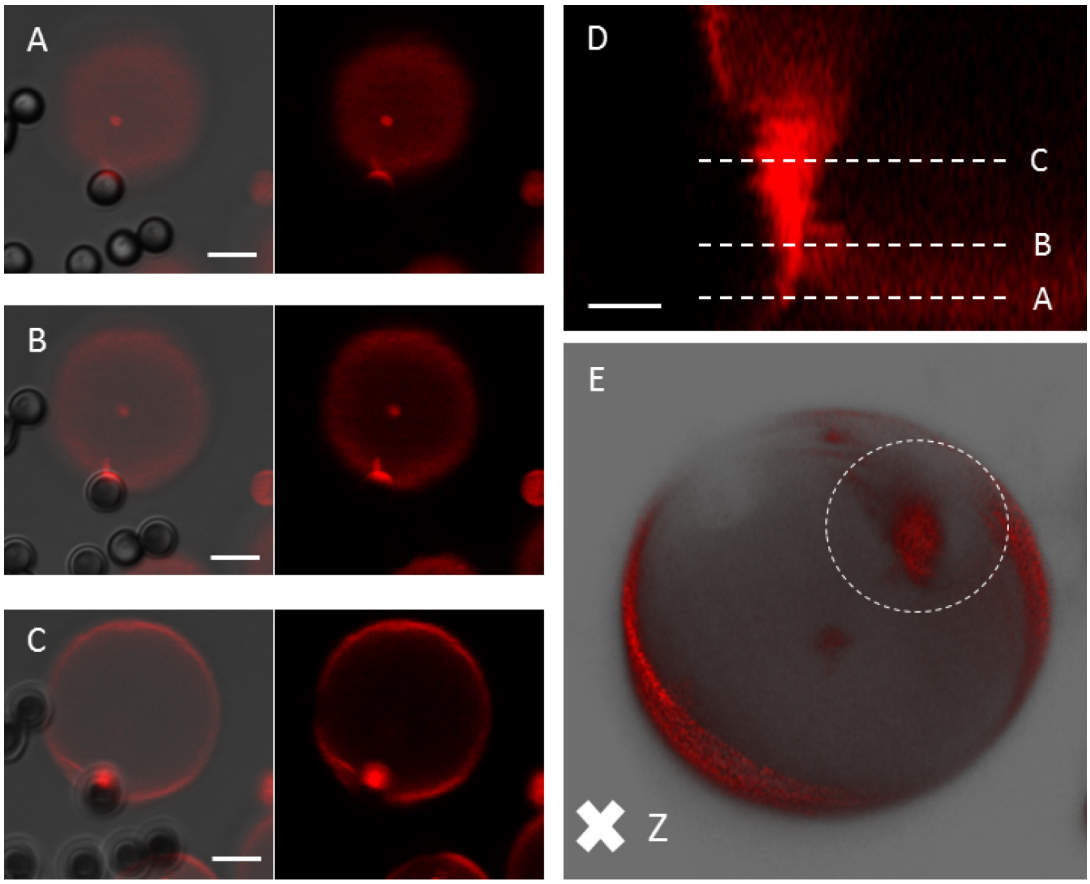

Fig. 3.15. 4 μm sulphate-functionalised (negative surface charge) polystyrene/metal coated Janus particle partially wetted by a 1% DOTAP GUV (0.2 mol% DiI). A-C) Confocal cross-sections at different z-positions through the sample, as indicated by the positions marked in D. The membrane partially wets the Janus particle and particle body is situated outside the vesicle contour. In image A one can see the membrane is adhered to the non-metallic region of the particle (the light region). D) XZ confocal cross-section obtained from many z-slices in the XY plane. This image shows the vesicle contour as it sits on the glass (at position A one can note the non-spherical behaviour of the membrane as it lays flat on the glass) and partially spreads over the particle surface. E) 3D reconstruction from multiple z-slices showing the protrusion of the membrane towards the vesicle interior in the region of the particle.

As we observed particle internalisation in some instances with Janus spheres, we decided to decrease the adhesion energy between the negative particles and positive vesicles by decreasing the amount of positive lipid in the membrane. A typical interaction for such a system is shown in Fig. 3.15. Here, we see the particle partially wetted by the membrane and that the particle body sits mostly outside of the GUV; a slight protrusion into the GUV can be observed most clearly in the 3D reconstructed image E. Interactions such as these were typical for this lipid composition and Janus particle combination; we did not observe any internalisation of the particles, only partial wetting. We can see in Fig. 3.15 that this is not a tense GUV, as it deforms slightly as it sits on the glass surface (as can be seen in image A and by looking at the contour of the vesicle in the XZ image in D). This would provide the additional membrane area required if further wrapping of the particle was energetically preferred by the system.

3.3.4 Janus particles can be held in a magnetic field and used to manipulate vesicles

To produce the Janus particles, we used metal vapour deposition on a monolayer of particles, as has been previously discussed in this Chapter. Not only does this provide the opportunity of rendering half of the sphere "inactive" with respect to the charges in the membrane, we can also utilise the properties of the metal coating, namely the response in a magnetic field. We found that upon incubating Janus particles with GUVs, we were able to manipulate the adhered particle-vesicle system, as can be seen in Fig. 3.16. Here, a 40% PG doped membrane is in contact with an amine-functionalised Janus particle. The chamber is placed between two magnetic coils, the setup of which has been previously shown and described in Chapter 3.2.5. Briefly, a current is passed through one coil, which generates a magnetic field with a non-uniform magnetic field gradient. This magnetic field gradient causes the particle to move through the chamber. In Fig. 3.16, we see a configuration of two Janus particles adhered to a vesicle. As the field is first switched on, the particle-vesicle ensemble rapidly rotates (<0.25 s), presumably to align with the magnetic field, and then moves from right to left through the chamber on the scale of seconds (~40 seconds to travel ~60 µm).

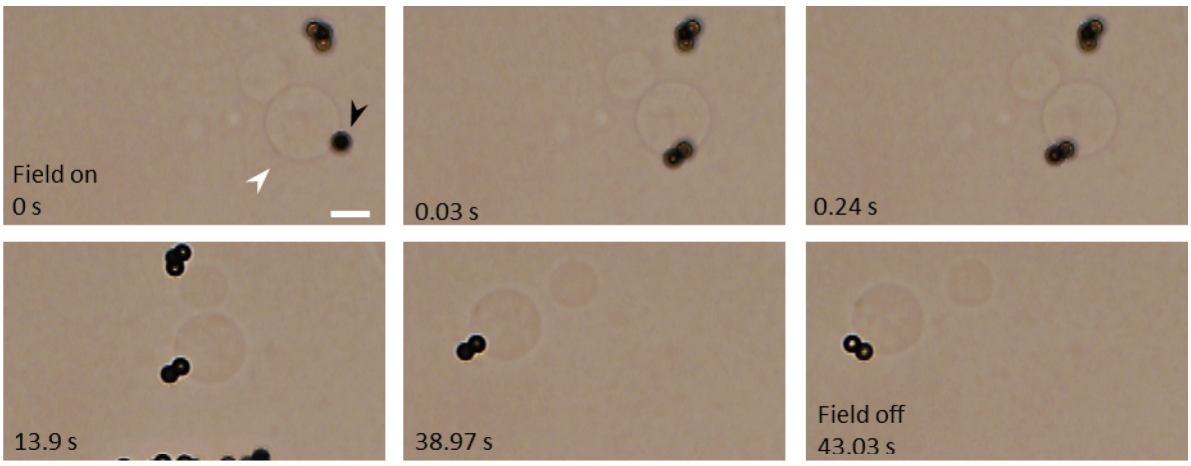

Fig. 3.16. Manipulation of Janus particle and adhering vesicle using magnetic field. Series of images from a time lapse sequence showing 6 µm amine-functionalised (positive surface charge) polystyrene/metal coated Janus particles adhered to a 40% DOPG GUV and manipulated using a magnetic field. The white arrow indicate the GUV and the black arrow the particles. As the field is switched on, the particles rapidly rotate while still remaining adhered to the GUV. The particle-vesicle configuration then moves through the chamber as a response to the field. Scale bar 10 µm.

It is not clear from the images whether the entire particle-vesicle configuration rotates as one in the field, or whether the particles move over the vesicle surface. One can also not distinguish from these images the region (metal or polystyrene) of the particle that is adhered to the membrane. The ability to move the particles through the chamber while the vesicle is still adhered indicates that this adhesion is at least stronger than the resistive forces acting on the vesicle due to drag in the fluid. Previous experiments (data not shown) have indicated that membranes do not adhere to the metallic regions of these Janus particles, regardless of the membrane composition. We only observed adhesion and engulfment, such as previously described, when we tuned the composition of the underlying particle and the GUV membrane such that they have opposite charges.

3.4 Discussion

Here, we observed how different particle surface properties affected the wetting and engulfment of the particles by the GUV membranes with different compositions. For uniform particle chemistries that apparently have sufficient adhesion energy, we observed complete wetting of the particle surface. For particles where only half the surface had such adhesive properties, we observed only partial wetting of the particle surface. It has been previously shown that membrane tension can play a role on the state of particle wetting/engulfment, with membranes under tension only partially wrapping both uniform and Janus-like particles.[48,73,74] To remove this component and instead focus only on the effects of adhesion energy and membrane bending energy, we used deflated vesicles with a reduced volume of at least 0.98 (which has been considered theoretically as a tensionless membrane[84,95]). For the particles with non-uniform surface chemistry, this allowed us to isolate the effect of the particle properties from the limitations that would be imposed on the system if the vesicle did not have sufficient excess area for total engulfment (ie, a tense vesicle). In Fig. 3.14, for example, this excess area present after adhesion by the Janus sphere is evidenced by the apparent multiple bilayer structures around the particle and the flat region of the vesicle contour, where it sits on the glass substrate. Additionally, using electrostatic interactions allowed us attain the equilibrium state of the systems where, for example, the membrane could de-wet the particle surface (if this was an energetically favourable process); this is in contrast to other similar experiments which use irreversible interactions between biotin and avidin to provide vesicle adhesion.[51,74]

We investigated the interactions of different particles using fluorescently labelled LUVs and GUVs; in the case of the latter, we could use confocal microscopy to visualise the behaviour different surface chemistries to broadly screen for combinations of particles and vesicles that could have sufficient adhesion energies for an initial adhesion and subsequent engulfment to occur, by looking at the fluorescent coverage of the LUVs on the particles' surfaces. We found that for the particles and vesicles that we used, electrostatic interactions were an important component of the adhesion energy. When we then carried these combinations forward to experiments with GUVs, we observed adhesion and engulfment of the particles by the GUVs. We first probed positively charged (amine functionalised) particles with negatively charged (40% DOPG) vesicles, and found that 1 μm amine particles were completely enwrapped by the GUV membranes. However, larger 6 μm particles were only found to adhere to the membrane surface and not be fully engulfed. As engulfment is a balance between membrane bending energy and the adhesion energy between the particle and the membrane (for tensionless, deflated membranes such as ours)[127], this lack of engulfment for these larger particles could be due to the nature of the particles themselves. For example, a lower density of functional groups on the particle surface could effectively decrease the adhesion energy. Due to material limitations, the two amine particle samples are composed of different materials; silica for the 1 μm and polystyrene for the 6 μm particles. The density of the amine groups on these particle samples is not known and might not be comparable due to the underlying particle material. Using a membrane composed entirely of negative DOPG lipid did not result in engulfment either. For some of the interactions with the 1 μm particles and GUVs, we also noted that the site of the particle engulfment had an excess of lipid material in the immediate vicinity, such as in Fig. 3.17. Membrane defects such as

these could have also aided in the engulfment of the small particles, possibly by first providing a site of initial adhesion and then subsequent excess area for the particle wrapping.

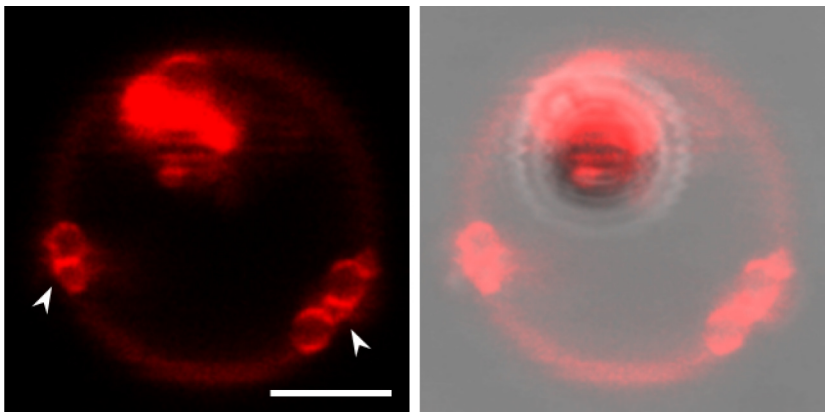

Fig. 3.17. Confocal cross-section of 4 μm sulphate Janus particle internalised by 5% DOTAP GUV with bright field image showing particle location overlaid (right image). The particle surface is not fully coated in lipid material. The arrows indicate the multilamellar structures of the vesicle. Scale bar 5 μm.

As we did not observe a strong interaction for the larger, positively charged particles (and experimental conditions would limit the ability to reliably produce a Janus surface on the 1 μm particles), we looked instead at the "opposite" configuration shown to interact in the LUV tests: negatively charged particles and positively charged membranes. For 5% DOTAP membranes and sulphate-functionalised polystyrene particles we observed complete wrapping of the particle by the membrane. This implies that the energy gain of the system due to the adhesion between the two is larger than the bending energy of the membrane required to enwrap the particle (as the membrane must bend against its preferred curvature to do so). As for the location of the wrapped particle relative to the main vesicle, we observed one of two configurations. Usually, the particle was internalised to the interior of the main GUV body, and often we could resolve the lipid structure tethering it to the unbound vesicle. We also observed one instance where the enwrapped particle was located to the exterior of the GUV, as in Fig. 3.10. This could be due to pore formation to reduce an increase in tension as the membrane spreads over the particle surface and increases the volume to surface area ratio. As the membrane reseals, it could reform such a way as to have the particle in this position. The formation of membrane pores are quite dynamic processes, as we will see later using microfluidics for the poly(ionic liquid) nanoparticles, and can often result in the visible "jump" of the vesicle as it quickly releases internal volume. It is also much harder to resolve the membrane contour in bright field in this figure, which suggests the exchange of solutions across the membrane via pore formation. Pore formation during vesicle engulfment was also discussed in this context by Dietrich et al.[48] Although we initially osmotically deflated the vesicles in glucose, the size of the particle relative to the vesicle could still require additional excess area for full engulfment.

For the interactions with Janus particles, where half of the surface was composed of negatively charged sulphate functional groups and the other half coated in metal, we observed a pinning of the contact line between the membrane and the particle (ie, the particle surface was not totally wetted with lipid). In the cases where we were able to

visualise the two regions of the particle surface (sulphate-polystyrene and metal, where the metal appears darker), we usually observed the fluorescently labelled lipids only on the sulphate regions of the particle. This agrees with our previous observations for uniform particles of the same surface chemistry, where we saw complete engulfment; we know that the adhesion between the negative particle and the positive membrane is sufficient for complete wetting and internalisation to occur. In Figs 3.12 and 3.13, one can see that the particle is partially engulfed by the vesicle body. One would imagine that when the attractive region of the particle comes into contact with the GUV, the vesicle membrane starts to spread over the surface of the particle (due to the adhesion energy exceeding the energy required to bend the membrane, as previously described), which in turn brings the particle towards the centre of the vesicle due to the decreasing vesicle radius. As the membrane reaches the region of the particle with lower adhesion energy, the energy gained by adhesion no longer exceeds the energy required to bend the membrane, and the particle is therefore stable in a partially engulfed state. However, partial wetting did not always equate to partial internalisation. In some instances, we observed the entire particle located inside the vesicle; however, this was also accompanied by multiple bilayer structures at the surface of the particle, an example of which can be seen in Fig. 3.14. For the particle to be located at the GUV interior, pore formation could have occurred during the wetting of the particle, and when the membrane re-sealed it could have closed over the top of the partially wetted particle, so that the particle was located inside the GUV. However, in another instance of Janus particle internalisation, a cross-section of which is shown in Fig. 3.17, we can also see membrane defects in regions of the GUV not in contact with the particle. One would assume that the vesicle would use these areas of excess area before the creation of a pore, as this would be a lower energy process; for example in micropipette aspiration of a GUV containing tubes, some of the tubes are pulled out before the tongue of the GUV starts to edge into the pipette.[128] In this instance, it is not yet clear how this particle came to have such a position inside the GUV. From the orientation of this particle, it is not possible to determine which region is coated with metal; however, one should note that although the fluorescent intensity from the lipid is clearly higher in one region of the particle, the lipid structures are not located on one well defined region of the particle surface. Without knowledge of the full history of the interaction, it is somewhat challenging in cases such as this to conclusively describe the process that has occurred. We also studied the interactions with the same Janus spheres and GUVs with only 1% of DOTAP, thus reducing the total vesicle charge. Here, we observed the particles were always partially wetted and were never internalised. Assessing these interactions qualitatively, we noted that the partial wetting covered less of the particle surface and the particles did not protrude as far into the interior of the vesicle in comparison to the more positively charged membranes. This is to be expected as decreasing the percentage of the positively charged lipid in the membrane should decrease the adhesion energy between the particle and the membrane. Possibly only the excess area of the deflated vesicle is used to wet the particle and bending of the quasi-spherical GUV is not energetically favourable (after the excess area is used up).

The ability of the Janus particles to displace the GUVs when in a magnetic field also opens up the possibility for applications such as transporting or applying a force to a membrane (such as torque, for example in a rotating magnetic field). Being able to use

this magnetic property of the particles in this work also helped to provide insight into the interaction between the negatively charged membrane (40% DOPG) and the positively charged (amine-functionalised) particles. Although we could not clearly resolve the region of contact between the membrane and the particle surface (for example, as described in relation to Fig. 3.8 where the fluorescence in the region of the particle is apparently decreased), being able to manipulate the vesicle using the Janus particle in a magnetic field indicates that adhesion does occur for this combination of particle and membrane compositions. It also demonstrates that it is strong enough to withstand the resistive force due to fluid drag on the vesicle. In the context of visualising the contact between the membrane and the particle, we also observed strange behaviour of the membrane fluorescence. For example, as described previously, we saw an apparent decrease in membrane intensity of the case of 40% DOPG membrane in contact with 6 μm amine-functionalised particles. We also noted that the fluorescent intensity of the membrane on the particle surface for the 5% DOTAP membranes and sulphate functionalised particles appears qualitatively much brighter; see Figs 3.9, 3.10 and 3.11. These effects could be due to the formation of multiple bilayers on the particles' surfaces during engulfment, although it seems unlikely that this would occur for all interacting particle-membrane pairs in these samples. We could also investigate the effect of using different membrane dyes in the future; DiI was used with the negatively charged particle experiments, and is a cationic dye. This could potentially cause partitioning of lipids and dye between the portions of the membrane bound and unbound to the particle. Similarly, for the reduced fluorescent signal observed for the 40% DOPG membranes with positive particles, the effect could be due to an enrichment of the negative DOPG lipid and an exclusion of the DPPE-Rh dye molecules.

The anisotropy of the particle surface also offers many further applications, apart from the ability to relocate the vesicles (as demonstrated here). The option to combine diverse or even incompatible functions into one structural unit and apply this to biomedical uses is very exciting and research in this direction is ongoing; for example bio-imaging and cell targeting.[129,130]

3.5 Conclusions and outlook

The adhesion to and engulfment of particles of different surface chemistries by vesicles of different compositions demonstrates the role that non-specific (i.e., not receptor-mediated) interactions may play in the engulfment of particles by cell membranes. We observed that the interactions between particles and vesicle membranes can be controlled electrostatically, with the strongest interactions (i.e., internalisation) occurring for oppositely charged particles and membranes. By using deflated vesicles (with reduced volume no larger than 0.98), we probed the interactions with only the interplay between adhesion energy and membrane bending energy to consider. For sulphate-functionalised (negative) particles and 5% DOTAP membranes, we observed the strongest adhesion energy, evidenced by the complete wrapping of the particle surface. These particles were mostly internalised but we noted one instance where the particle body was located mostly at the GUV exterior. For this interaction, we postulated that the wrapping event may have involved pore formation, resulting in the final configuration we observe. This was also supported by the faint contour of the vesicle observed in bright field, suggesting exchange of solutions across the membrane via pore formation. We did not observe partial wetting

for these uniform particles. We also probed the stable engulfment states that a particle with an anisotropic surface can occupy by using sulphate particles with half their surface coated in metal. We observed both partial engulfment and full engulfment for these particles, but not complete wetting of the particle surface. When the percentage of positive lipid in the membrane was decreased, we only observed partial engulfment and partial wetting of the particle surfaces (for Janus particles).

We attempt to explain the different engulfment and wetting interactions that we see here by considering the movement of the membrane as it comes into contact with the particle and the energies that would be associated. It would be interesting to follow the interaction processes as they occur, particularly for behaviour of the membrane as it spreads over the Janus particle and comes into contact with the non-adhesive region of the surface. This would also help us to understand the process that occurs in order for these partially adhesive particles to be engulfed, and how such internalisation can occur when the whole particle surface is not coated with a membrane. One such method we could use for this experiment would be to hold the particles with a micropipette and bring it close to the GUV membrane. It would be important to release the particle from the pipette once the adhesion occurs so that the presence of the pipette does not interfere with the spreading of the membrane over the particle surface. By using micropipettes we could also modulate the tension of the GUV and measure the contact angle of the membrane with the particle by changing the aspiration pressure, an approach we could use for both Janus and homogeneous particles. Measuring the contact angle between the membrane and the particle would allow us to determine the adhesion energy between the two. For the experimental method we have been using in this chapter (incubation of the particles and GUVs) we could also gain further insight into the behaviour of the system through some of the following: modulating the salt concentration of the solution so as to screen the electrostatic interactions; conduct more experiments so that we could generate statistics for the penetration of the particles into the membrane (for example, by looking at how this penetration depth varies with the ratio of particle to vesicle size); or immobilise the system in agarose to look at how the adhesion and engulfment behaves when the interaction of the membrane with the glass surface is not involved.

4 Poly(ionic liquid) nanoparticles selectively permeabilise lipid vesicles in anti-microbial-like fashion

4.1 Introduction

The study of particle-membrane systems has grown considerably in recent years due to the many applications that understanding such interactions can have, from drug delivery to medical imaging,[4,65] as has been introduced and discussed in Chapter 1. To continue the development and success of within this research field, new classes of particles should be investigated for their potential interactions. This is particularly relevant for particles that exhibit membrane-active properties, due to the recent increase in bacterial resistance.[11–14] When evaluating the effects that potential membrane-active agents can have on membrane integrity and properties, it is common to use bulk assays such as assessing the leakage from spherical small and large unilamellar vesicles (SUVs and LUVs respectively, with diameters ~20-100 nm).[54,55,131] However, the size of these vesicles can raise more questions and problems than the solutions they provide. For example, the role that membrane curvature plays at this size may not be comparable with that of cell membranes, which are typically much larger; also, the small size of LUVs and SUVs means they cannot be directly imaged and as such it is challenging to extract information about vesicle integrity. An alternative model system for such probative assays is GUVs, the benefits and characteristics of which have been discussed previously in Chapter 1. In the context of examining membrane stability, they offer the advantage of having sizes in the range of 10-100 μm, allowing direct visualisation of the potential interactions.[53,132] Recent studies have shown the promising applications of nanoparticles as a potential antimicrobial candidate.[15–18] Here, we investigate the action of nanoparticles formed from poly(ionic liquid)s with biomembranes and compare these interactions to those of known anti-microbial agents, such as anti-microbial peptides. Poly(ionic liquid) nanoparticles (PILs) are formed via dispersion polymerisation of vinylimidazolium-type liquid monomers, as was first presented by Yuan et al[77]; experimental details can be found in Chapter 4.2.3. They assemble into liposome-like, multi-lamellar structures, and their cross-section resembles that of an onion. A cross-section of the particles' internal structure (via cryo-TEM) along with the chemical structure of the PIL can be found in Fig. 4.1. These particles are unique in that they combine the attractive properties of polymers, such as flexible functionality,[133] with the additional properties provided by ionic liquids.[134] Among these, ionic liquids have been shown to have significant anti-microbial properties[79,80] and also to act against bacteria, fungi and algae.[135] Ionic liquids in polymeric form still act against microbes, as demonstrated by the antibacterial properties of poly(ionic liquid) brushes.[136] In the context of model membrane systems, the activity of an anti-microbial agent, typically an anti-microbial peptide, can be observed, among other methods, via leakage of molecules into or out of GUVs;[81] changes in membrane morphology (thickening of the membrane);[137] or GUV bursting.[59] The possibility of PIL nanoparticles as an anti-microbial agent has yet to be investigated.

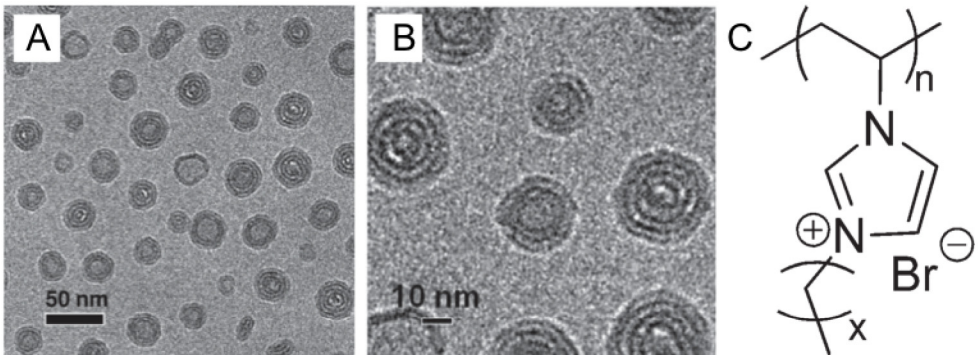

Fig. 4.1. PILs structure. A-B) Cryo-TEM images of PILs nanoparticle structures for ILM-C14. C) Chemical structure of poly(ionic liquid); x = 14 in this work. All images adapted from Yuan et al.[77]

In this chapter we examine the behaviour of GUVs in the presence of PIL nanoparticles primarily using optical microscopy. We varied the membrane compositions to between different amounts of neutral and negatively charged lipids, as this allowed us to distinguish the effect PILs would have on membranes that act as bacterial mimics.[138,139] To further understand the role of membrane charge, we also used membranes containing a proportion of positively charged lipids. It has been previously shown that in many instances charged membranes are required for the action of these membrane active molecules.[140,141] We went on to determine the lytic activity of these particles on membranes by counting the number of surviving vesicles as a function of PILs concentration. We also observed further disruption of the membranes such as bursting, and macro- and submicron-pore formation. A microfluidic device allowed us to follow the dynamics of the particle-membrane interactions from the moment the particles were introduced to the vesicles, and also allowed us to observe a fixed population of GUVs from start to finish. In order to detect membrane binding and the subsequent PILs' locations, the particles were fluorescently labelled using Rhodamine-B; this labelling process is described in more detail in Chapter 4.2.3. We assessed molecular changes in the membrane by measuring the lipid diffusion coefficient in the presence of particles and visually inspected the morphological appearance of the membrane for changes in overall membrane properties. Finally, we propose a series of possible mechanisms through which the particles may be interacting with the membrane.

4.2 Materials and methods

4.2.1 Materials

Lipids and fluorescent analogues, ITO glasses, glucose, sucrose, BSA and agarose were obtained as described in Chapter 2. Polydimethylsiloxane (PDMS) was used in the production of microfluidic devices and obtained from Biesterfeld Spezialchemie GmbH (Hamburg, Germany). Rhodamine B (>95%), 1-vinylimidazle (99%), and 1-bromotetradecane (97%) were purchased from Sigma-Aldrich. All chemicals were used without further purification. Milli-Q water was used throughout.

4.2.2 GUV preparation

Solutions of lipids in chloroform were prepared in different compositions of DOPC and either DOPG or DOTAP as the charged lipid species with the following ratios: 90/10 DOPC/charged lipid; 60/40 DOPC/charged lipid; 100% DOPC. The solutions were prepared to 4 mM without fluorescently labelled lipid species, unless explicitly stated in the relevant location in Chapter 4.3 (Results). The GUVs were prepared using the previously described electroformation protocol.[97] In total, 16 μL of lipid solution was deposited between two ITO glasses and spread using the syringe. This lipid film was first dried under a stream of nitrogen, and subsequently under vacuum for 2-2.5 hours at room temperature to remove any remaining solvent. Using a Teflon spacer, a chamber was assembled with the two ITO glasses and filled with 200 mM sucrose solution. By connecting the chamber to a function generator, an alternating current was passed through the growth chamber at 1.2 V, 10 Hz for 1.5 hours at room temperature. When the lipid composition contained a fluorescent lipid species, the growth was performed in the dark. For the lipid compositions containing DOPG, the electroformation was either performed at 60 °C or the GUVs were left for 1 day before dilution in glucose.[142] The vesicles were removed from the chamber using a pipette and stored in an Eppendorf tube. They were then either mixed in a 1:1 ratio with an osmotically matched glucose only or particles in glucose solution. The preparation of the particles is discussed subsequently. The samples were left to incubate and equilibrate for 1 hour before observation.

4.2.3 Particle preparation and characterisation

The non-labelled PILs were prepared via the previously introduced method by Yuan & Antonietti;[76] the structure of these nanoparticles was later found to be lamellar in nature, formed from concentric layers.[77] Briefly, 5g of ionic liquid monomer (prepared using the general protocol described in [76]) 3-n-Dodecyl-1-vinylimidazolium bromide (ILM-12, M_p = 47 °C) was added to a 250 mL Schlenk flask, along with 150 mg VA86 (water-soluble non- ionic azo initiator) and 100 mL of water and mixed. The mixture was completely deoxygenated by three cycles of freeze-pump-thaw procedure and backfilled with argon. The flask was then stirred in an oil bath at 70°C for 24 h. The polymerisation reached nearly full conversion (99-100%) and a stable reaction solution was obtained, which was then exhaustively dialysed against deionised water. The PILs labelled with Rhodamine-B followed the same preparation method as outlined previously, with the additional step of mixing Rhodamine-B with ionic liquid monomers prior to polymerization. Dialysis was applied to remove residual Rhodamine-B after polymerization.

The PILs' sizes were assessed from transmission electron microscopy (TEM) images and DLS measurements and the surface charge was assessed using electrophoretic mobility

measurements. The TEM images were provided by W. Zhang, an example of which is shown in Fig. 5.1, and the sizes determined by fitting circles in ImageJ to the particle circumference, a simplified view of which can be seen in the inset. The average particle size was determined from 20 particles from 3 different images within the same sample. DLS measurements were also conducted by W. Zhang. DLS operates on the principle that particles move under Brownian motion in a gas or liquid and that the velocity of the particles depends on their size. A laser is passed through the particle sample and the amount of scatter of the light is deconvoluted to determine the particle size (as smaller particles will move faster and cause the intensity to fluctuate more rapidly than large particles).

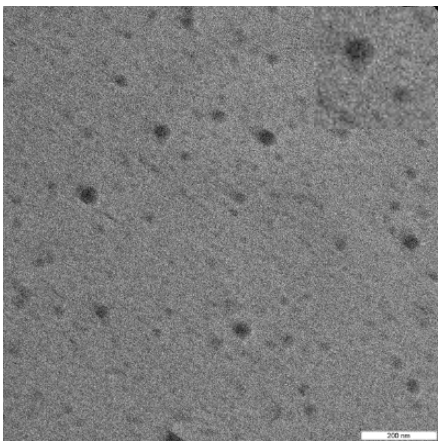

Fig. 4.2. Determining PILs nanoparticle size from TEM images, adapted from[143]. Example TEM image of Rh-PILs from which the average particle size was measured by fitting circles around the particles in ImageJ (as shown for zoomed in region inset). Scale bar 200 nm.

Zeta potential measurements were performed using a Zetasizer Nano ZS (Malvern Panalytical, UK). For the electrophoretic measurements, a PILs suspension at 0.01 mM was measured at 40 °C with 100 sub-runs per measurement. The Zetasizer works by measuring the velocity of particles that move in a cell when a potential is applied across electrodes. The velocity is expressed in terms of the electrophoretic mobility of the particles.[144] The zeta-potential is extracted by the software value using the following equation:

$$U_E = \frac{2\varepsilon\zeta f(\kappa a)}{3\eta} \qquad 7$$

where U_E = electrophoretic mobility, ζ = zeta potential, ε = dielectric constant, η = viscosity and $f(\kappa a)$ = Henry's function. A schematic representation of what the zeta-potential is measure of for a (negatively charged) colloid system is presented in Fig. 4.3.

The density of the particle configuration was measured using a density oscilation tube (DMA 5000M, Anton Paar, Graz, Austria), which was found to be 1.137 ± 0.003 g/ml.

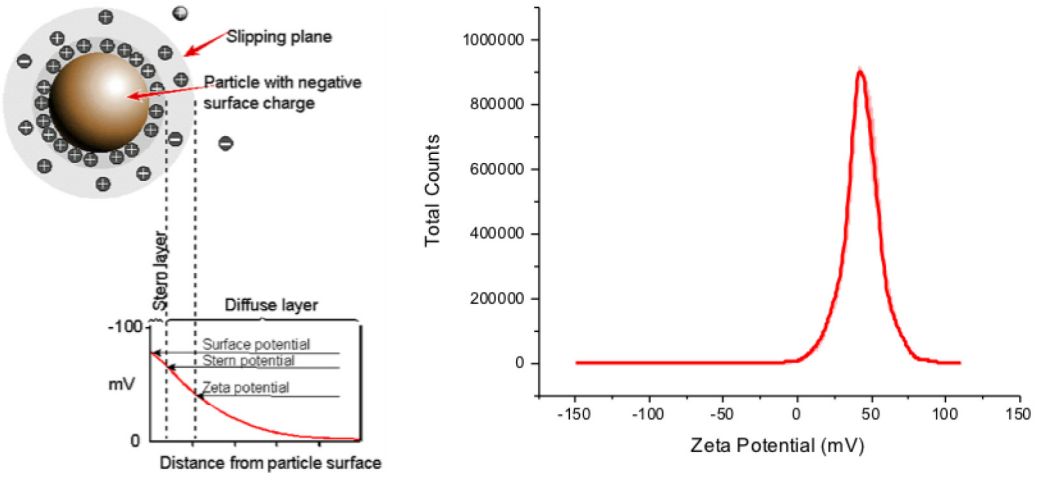

Fig. 4.3. Determining PILs' zeta-potential using a Zetasizer. A) Schematic diagram of the layer of ions that are measured for zeta-potential measurements; example is for a negative particle. Figure adapted from Malvern Panalytical.[144] B) Average zeta potential of PILs taken from 3 repeat measurements, pale red region shows standard error.

4.2.4 Fabrication and use of the microfluidic device

Microfluidic devices were used for observation of the same population of vesicles, before and after the addition of the particles. Microfluidic devices offer the opportunity to confine specific groups of vesicles for observation by making use of lamellar flow.[145] This approach offers advantageous over techniques such as micro-pipette aspiration[145] and surface modification,[146] which can impose changes on the system, such as increasing tension or introducing artificial lipids to the membrane. The device that we used had many hydrodynamic traps situated throughout its channels, where the individual traps were formed from multiple posts, creating a bucket-like shape on the order of magnitude of many 10's of microns; see Fig. 4.4 for a schematic diagram of the trap layout. The devices were fabricated following soft lithography procedures that have been reported in the literature previously.[147] Briefly, PDMS oligomer and curing agent were mixed at a ratio of 10:1 and poured onto the silicon wafer master (feature height: 40 µm) to a final thickness of 5 mm and then cured at 80˚C for 3 hours. It was then cut to size and 1.5 mm holes were punched using a 1.5 mm Biopsy puncher (Miltex, Plainsboro, New Jersey). The device was finished, and the microfluidic channels sealed, by bonding 170 ± 10 µm glass coverslips to the lower side using air plasma (1 min, 0.5 mbar; PDC-002, Harrick Plasma, Brindley, Ithaca) and subsequently left at 60˚C for 30 minutes. For operation, the device was first filled with bovine serum albumin (BSA) at 20 mg/ml dissolved in 200 mM glucose (a solution which has first been filtered using 0.45 µm pores) using centrifugation (900x g, 10 minutes). This creates a protein coating on the walls of the device to minimize vesicle sticking,[148] while the centrifugation ensures a bubble-free environment. GUVs, PILs and other solutions were delivered to the device through a reservoir, with a syringe pump (neMESYS, cetoni, Korbussen, Germany) connected to the device at the other end (from the reservoir) and operating in withdrawal mode. The BSA was removed from the device by flushing through with 200 mM sucrose (20 µL/min, 10 minutes). The GUVs were then introduced into the device in their sucrose

growth solution (10 µL/min, 15 minutes), followed by the addition of osmotically matched, filtered 200 mM glucose solution (5 µL/min, 5 minutes), which induces phase contrast between the inner and outer solutions, as has been described in Chapter 2.5.1. The GUVs held in the microfluidic trap, before and after the addition of glucose, can be seen in Fig. 4.5. The PILs particles are then introduced into the microfluidic device at a lower flow rate (2 µL/min) and images and time lapses were recorded throughout on an Axio Observer microscope, as will be described in the subsequent section.

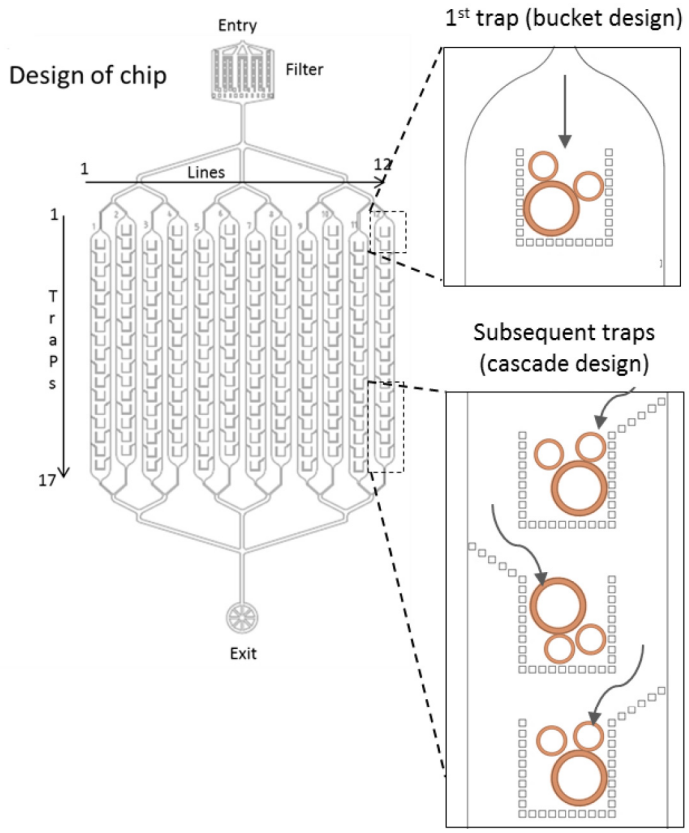

Fig. 4.4. Microfluidic device design. Schematic diagram showing the layout channels and traps within the microfluidic device and the flow of the vesicles into the two different types of traps used. The arms at 45˚ on the cascade traps direct the vesicles that are flowing past into the traps. Image courtesy of Yandrapalli & Robinson, in review.

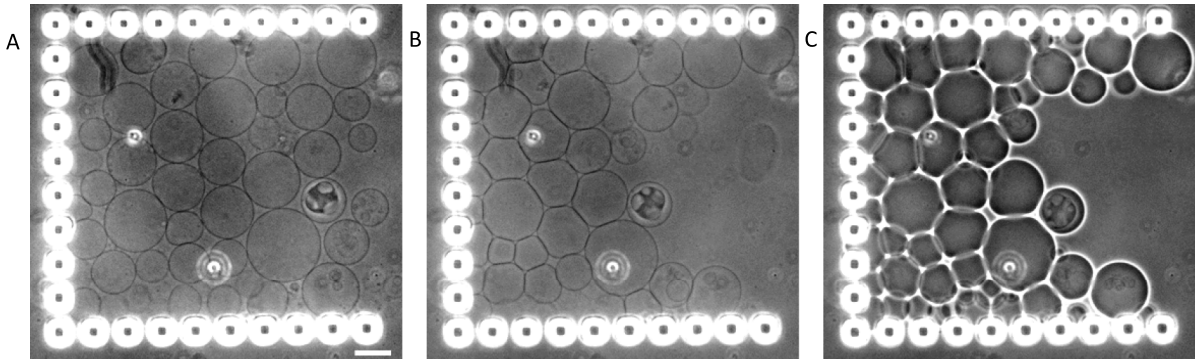

Fig. 4.5. Filling microfluidic device with GUVs and glucose for monitoring specific GUV populations. A) The vesicles are introduced into the microfluidic device using a syringe pump in withdrawal mode. The image shows the vesicles when no flow rate is applied and with the same sugar (sucrose) as the inside and outside solution. B) As soon as the pump is switched on to introduce the glucose, the GUVs move to the left and are more compressed due to the flow rate (but do not pass between the posts of the trap). C) After the glucose reaches the vesicles (approximately 1 minute) the sugar asymmetry between the GUV interior and exterior causes phase contrast (the dark inside and the white halo around the vesicle). Scale bar 10 μm.

4.2.5 GUV-particle observation

For observation of GUVs with PILs (excluding microfluidics, see previous section), the vesicles were harvested from the growth chamber (in sucrose) and diluted 1:1 with either an osmotically matched solution of glucose (for control experiments) or varying PIL concentrations (also in osmotically matched glucose solutions). As described in Chapter 2.5.1, a dilution of vesicles grown in sucrose in a glucose solution induces phase contrast, and also causes sedimentation of the GUVs to the bottom of the viewing chamber. As we will see in the Results section in this chapter, the presence of the PILs can cause exchange of solutions across the membrane. This both removes the phase contrast, as the density of solutions inside and outside the vesicles is the same, and also means the vesicles no longer sediment. Both of these factors affect the ability to image the vesicles (for example, obtaining optical slices of a moving vesicle is very challenging). One approach to improve vesicle visualisation is via immobilisation by mixing the vesicle-PILs solution 1:1 with a solution of liquid agarose (0.5% w/v in 200 mM glucose, heated to room temperature), as described in Chapter 2.3. This approach was used for observation of all vesicles in the presence of PILs (not including microfluidic experiments), and also used for observation of any control GUVs. When the agarose cools to room temperature, it creates a mesh-like structure, holding the vesicles in place. The samples were then ready to be viewed on a microscope.

For phase contrast imaging, the technique of which is described in Chapter 2.5.1, an Axio Observer D1 (Zeiss, Germany) microscope was used, which was equipped with a Ph2 20x (NA 0.5) objective, connected to an ORCA R2 CCD camera (Hamamatsu, Japan) for imaging. An HBO 100 W mercury lamp was used for sample irradiation. For the vesicle population statistics described later in this chapter, 4.3.1, and recordings were obtained on the previously referenced CCD camera at a frame rate of 15 fps. These were z-stacks taken of 5 randomly selected regions in each sample, in which the vesicle population was counted manually. The vesicle size was measured in ImageJ by fitting circles to the

vesicle contours at the vesicle mid-planes, see Fig. 4.6 for an example of a circle fitted to a vesicle contour.

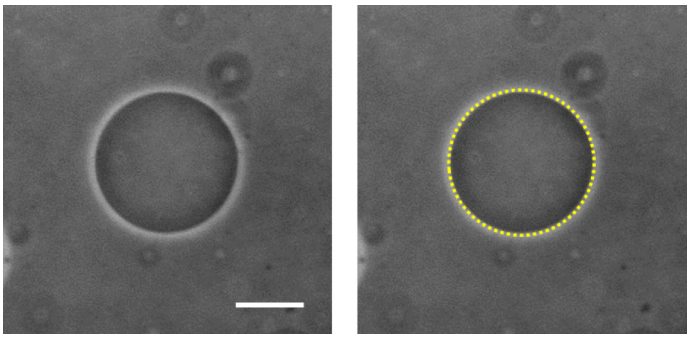

Fig. 4.6. Fitting circle to vesicle contour in ImageJ to measure size. Scale bar 20 μm.

Confocal images were obtained on a Leica confocal SP8 setup (Mannheim, Germany). Rhodamine-B (in the PILs) and Rh-DPPE (in the membrane) were both excited with a 561 nm laser and NBD-PC (in the membrane) was excited with the 476 nm line of an Argon laser. The fluorescence signals for the rhodamine dyes were collected for the wavelength range 570-700 nm, which was adjusted to 620-700 nm in the presence of NBD-PC to account for any crosstalk between the rhodamine and the NBD dyes. The fluorescence signal of NBD-PC was collected between 483-515 nm. The images were collected with a 40x (0.75 NA) dry or 63x (1.2 NA) water immersion objectives and a pinhole size of 1 Airy unit. The analysis of these confocal images is described in the subsequent section.

4.2.6 Image intensity analysis

Image intensity quantification was performed either in the Leica software (Leica Application Suite) using an intensity line profile or by measuring the average membrane intensity within a user-defined ROI; or a radial intensity distribution plugin in ImageJ was used to measure intensity as a function of radius (radially averaging accounted for dye polarisation effects).

Intensity at the GUVs' membranes from the fluorescently labelled PILs was measured in the Leica Application suite software by taking user defined ROIs of the membranes, taking care to account for any dye polarisation effects or areas of membrane defects; the latter could contain membrane segments which were no longer a bilayer and would contribute a higher value to the intensity average. The intensities were measured on non-labelled GUVs incubated with Rh-PILs, where the dye in the PILs was excited with a 561 nm laser line and the emitted fluorescent signals detected in the 570-700 nm range. Images were obtained at the vesicle equator (the focal plane of widest diameter) for a minimum of 9 GUVs in each sample. Fig. 4.7 A shows an example measurement for the PIL intensity on the membrane and how the effects of dye polarisation were accounted for by selecting a region that incorporated an equal amount of maximum and minimum intensity; the source of the dye polarisation is discussed in the Results section in this chapter. Fig. 4.7 B indicates a region of the same vesicle that would not have been included in the ROI due to a visible membrane defect.

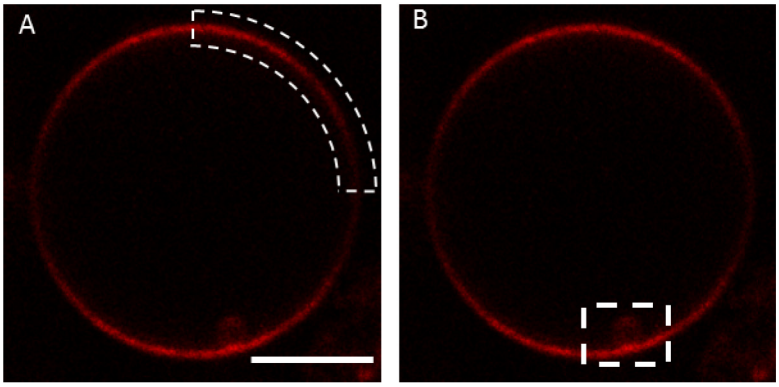

Fig. 4.7. Confocal cross section through a GUV with Rh-PILs particles, indicating how the intensity from the particles is extracted from the image; figure adapted from[143]. A) Region of interest for measurement selected such as to account for dye polarisation effects (regions of higher and lower intensity at the poles of the membrane). Scale bar 5µm. B) Area with membrane defect which would not be included in ROI intensity measurements.

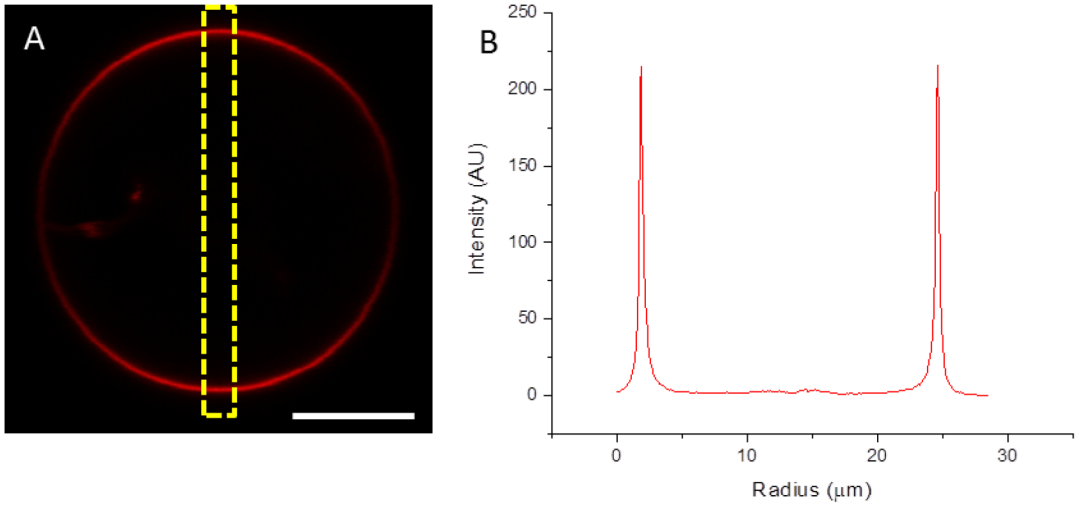

Fig. 4.8. Using line profiles to measure membrane intensity. A) Confocal cross section of a GUV where yellow ROI indicates 2 µm-thick line used to generate line intensity plot. Scale bar 10 µm. B) Line intensity profile generated from the confocal cross section shown in A).

Line profiles were also used to measure vesicle intensity at different angles through the GUVs. This was also performed in the Leica Application Suite for the same images that the user-defined ROI intensities were taken from. In the software, a 2 µm strip was selected through the GUV at the desired angle, an example of which is shown in Fig. 4.8 A. This generates a plot of intensity as a function of distance, as can be seen in Fig. 4.8 B.

The fluorescence profile across the membrane from the outside to the inside of the GUVs was extracted using the "radial profile extended plugin" developed by Phillipe Carl, obtainable from the ImageJ homepage. The GUV images at the vesicle equators are imported into ImageJ and the plugin fits a circle, or segment of a circle, around the vesicle. The radius of the circle is adjusted such that a portion of the bulk signal outside the vesicles is also included in the measurement. The plugin displays the intensity for the selected ROI as a function of radial distance; a typical vesicle measurement is shown in Fig. 4.9, along with the resultant intensity profile. Such profiles were obtained for 10 vesicles in each sample. In the results, the intensity values for each image were normalised to the peak intensity value (taken as the intensity value at the peak inflection point), and the radial values (x axis) were also normalised such that the peak position (membrane) sat at $x = 1$. The benefit of using this method is that the intensity is averaged radially over the whole segment of the membrane that is in the ROI; thus the average is generated from a greater proportion of the membrane.

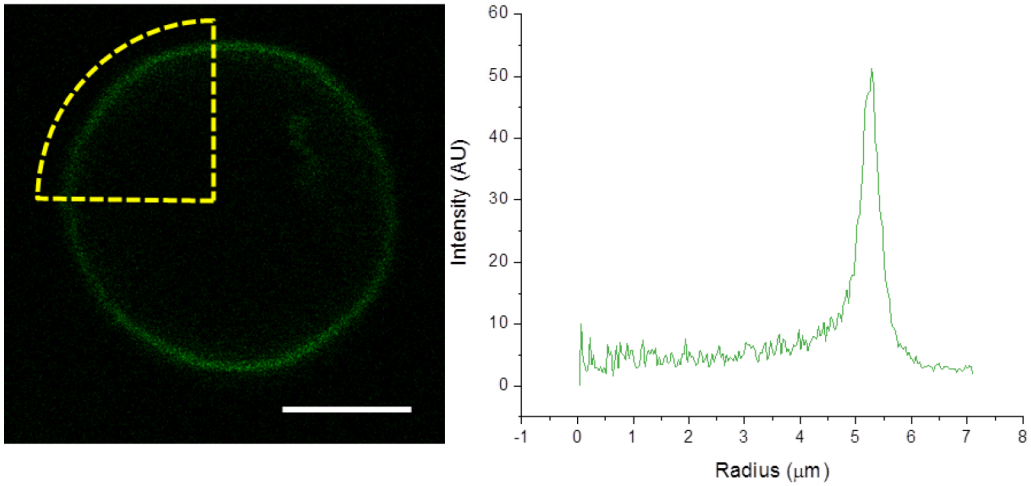

Fig. 4.9. Intensity measurements across GUV membranes were extracted using a radial profile angle ImageJ plugin. A) Confocal cross section of GUV with yellow ROI indicating segment over which the intensity is averaged as a function of radial distance. B) Resulting intensity plot as a function of radial distance.

4.2.7 Fluorescence recovery after photobleaching (FRAP)

FRAP is a widely used confocal microscopy process implemented to understand the diffusion of fluorescently labelled molecules. It can be used, in the context of cellular studies, to provide information on how lipids and proteins interact with their environment, for example for processes such as the interaction of proteins and lipids with membrane domains.[149,150] In FRAP experiments in GUVs, fluorescently labelled molecules (in our case, fluorescently labelled lipids, Rh-DPPE) are irreversibly photobleached using a high-power laser beam, and the recovery of fluorescently labelled molecules from outside this bleached region back into it is recorded.[151] From the recovery curve of fluorescence in this region of interest (ROI), the diffusion coefficient D can be calculated; a typical recovery curve is shown in Fig. 4.10, along with a schematic diagram demonstrating how such a FRAP experiment would proceed at the membrane. However, extracting this value can be a complex issue due to the in-depth knowledge of FRAP theory that is required, and there are several reported methods in the literature.[152–154] The most widely used equation for describing the Brownian two-dimensional diffusion is the following:

$$D = \frac{{r_n}^2}{4t_{1/2}} \tag{8}$$

in which r_n is the radius of photobleaching and $t_{1/2}$ is the time taken for the intensity in the bleach region to recover by half; the equation is modelled on instantaneous bleaching.

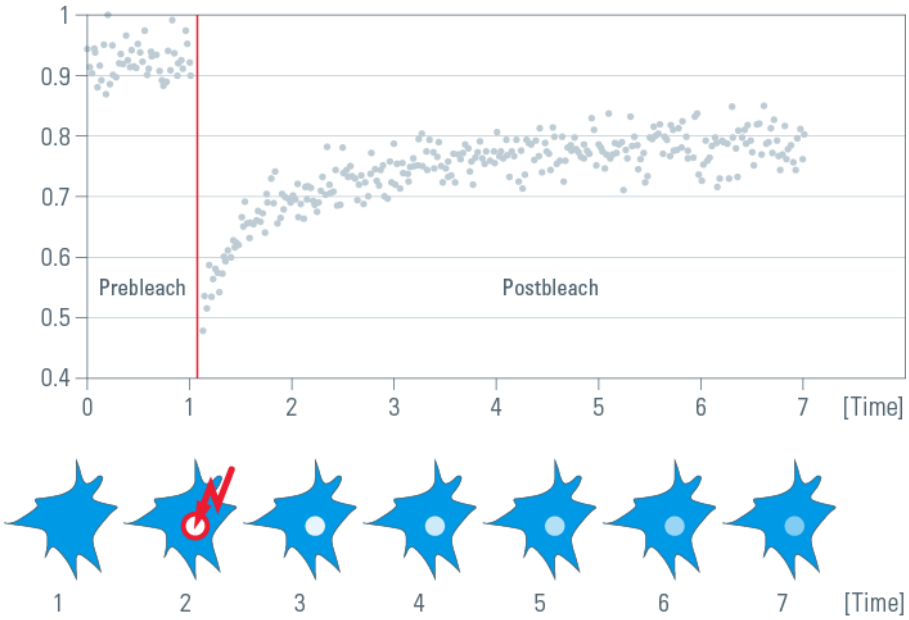

Fig. 4.10 Schematic diagram showing an example FRAP experiment (bottom) and a simplified complimentary recovery curve (top). A region of a fluorescent sample is bleached using a high-powered laser, such that the molecules in that region of interest (ROI) will no longer fluoresce. The recovery of the fluorescent signal in that region due to the movement of non-bleached surrounding molecules diffusing into it is recorded and can be used to measure the lipid diffusion coefficient of the membrane. Adapted from Leica Microsystems.[155]

For sufficient bleaching to occur however, the time required for bleaching can be on the order of milliseconds. For molecules that have a high coefficient of diffusion, bleaching over this time period can no longer be considered instantaneous and the bleaching region itself is no longer well-defined. As such, one approach is to introduce a term which also accounts for lipid/molecule diffusion during the photobleaching process, the effective radius of bleaching r_e, which exceeds the nominal radius r_n.[150] This results in an adjusted equation for the diffusion coefficient, as shown in the following equation:

$$D = \frac{{r_e}^2 + {r_n}^2}{8t_{1/2}} \tag{9}$$

The value of $t_{1/2}$ can be extracted from a recovery curve (Fig. 4.11 A) by determining the time at which the fluorescence intensity in the ROI has recovered to half the value, $F_{1/2}$, of the intensity at the end of the post-bleaching period, F_∞, using the following equation and examining the graph in Fig. 4.11 A:

$$F_{\frac{1}{2}} = \frac{F_0 + F_\infty}{2} \tag{10}$$

The effective radius can be extracted by fitting a curve to the intensity line profile taken through the ROI in the first frame post-bleaching; an example of this is shown in Fig. 5.7 B. The equation of the fit of this intensity is as follows:

$$f(x) = 1 - K\ exp\frac{-2x^2}{r_e^2} \tag{11}$$

where x is the radial position and K is the bleaching depth, as indicated in the figure.
Experimentally, we performed FRAP measurements using the following steps. Membranes were labelled with 0.1 mol% Rh-DPPE, with and without non-labelled PILs present in the samples. Images were recorded on a Leica SP8 confocal system at 1400 Hz, with a pinhole size of 1 Airy unit, in bidirectional mode, and with an image size of 256 x 256 pixels, exciting at wavelength 561 nm. Before the bleaching of the membrane took place, 10 frames at attenuated laser intensity (below 5%) were recorded, also known as the pre-bleaching phase. The photobleaching was performed for 200 ms (3 frames) at 100% laser intensity using a circular region of interest (ROI) of nominal radius r_n = 1 μm. The post-bleach recovery images were then recorded at the initial attenuated laser intensity for several seconds. The photobleaching was always conducted on the upper or lower vesicle surface. Values of r_e were obtained for each sample (ie, control and particle containing samples) by fitting equation 3 for a minimum of 5 vesicles within the sample, and taking an average value. Values of r_e = 3.50 μm and r_e = 3.35 μm were used for the control and particle containing samples respectively.

From the recovery curve (Fig. 4.11 A), it is also possible calculate the mobile fraction (M_f) with the following equation:

$$M_f = \frac{F_\infty - F_0}{F_i - F_0} \tag{12}$$

where F_i is the intensity before photobleaching. This tells us the percentage of the molecules which are free to diffuse back into the bleached region; i.e., are not bound to slow or immobile structures.

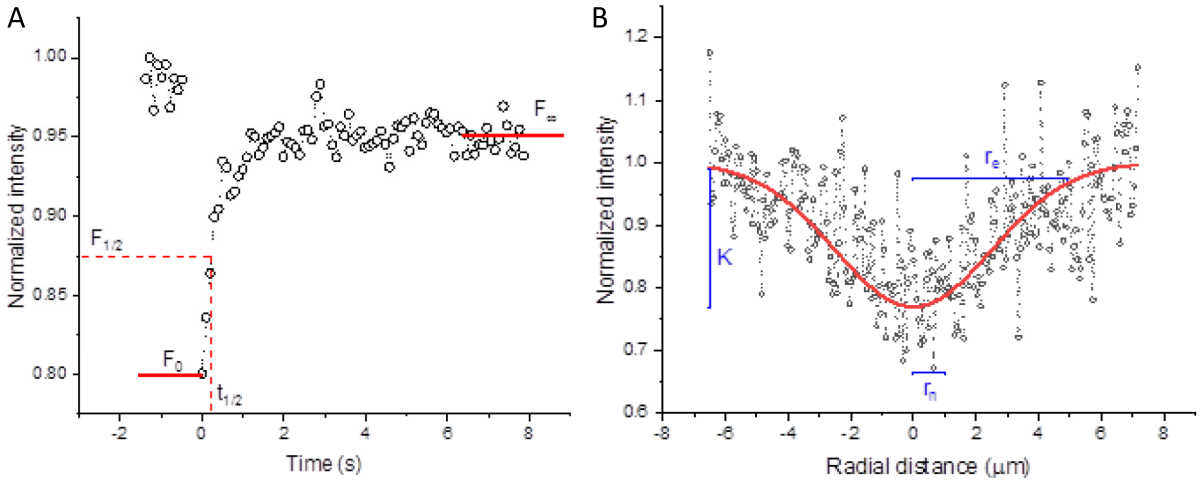

Fig. 4.11 Typical photobleaching recovery curve and intensity of ROI post-bleaching used for determining lipid diffusion coefficients.; figure adapted from [143]. A) Example FRAP recovery for a GUV formed from DOPC and immobilized in 0.5% w/v agarose. F_0 is the intensity of the ROI in the first frame post-bleaching, F_∞ is the intensity after the membrane has recovered and $t_{1/2}$ is the time taken for the intensity to recover by half. The immobile fraction is reflected by the difference between the pre-bleach signal to the recovered one, rescaled by the latter. B) Intensity line profile of the first frame post-bleaching. The red line is a fit of the data using equation 11 and from this the value of r_e for each vesicle is obtained. The value of r_e used for the calculation of each diffusion coefficient is an average of the r_e values obtained for vesicles in the same sample. In the plot, the parameters *K* and r_n are also labelled in blue. Data shown in A) and B) are from the same GUV.

4.2.8 Fluorescence intensity measurements in bulk

To determine the number of Rh-PILs particles on the vesicle membranes, confocal images were taken of GUVs with known concentrations of lipid conjugated Rhodamine-B, Rh-DPPE. Although both dyes used (in the PILs and the lipid conjugated dye) are derivatives of Rhodamine, one cannot assume that the fluorescent behaviour of these molecules in different environments is the same. To compare them, solutions of PILs with known Rhodamine-B concentrations (see section on particle preparation and characterisation earlier in this chapter) and solutions of multi-lamellar vesicles (MLVs) (see section on MLV preparation in Chapter 2) containing the same concentrations of Rh-DPPE were measured using a fluorimeter FluroMax-4 (Horiba, Germany). The two fluorescent samples were measured using a quartz transparent cuvette, which was rinsed (using ethanol and water) and dried between each sample measurement. The fluorescence emission of each sample was collected from 570-700 nm for an excitation of 561 nm (slit width 1 nm), matching the confocal imaging settings. See Fig. 4.12 for an example emission curve. To determine the intensity for each sample the areas under each curve were calculated. These intensities were calculated for three concentrations of dye and the ratio between the integrated intensities for the different samples was averaged from these three experiments.

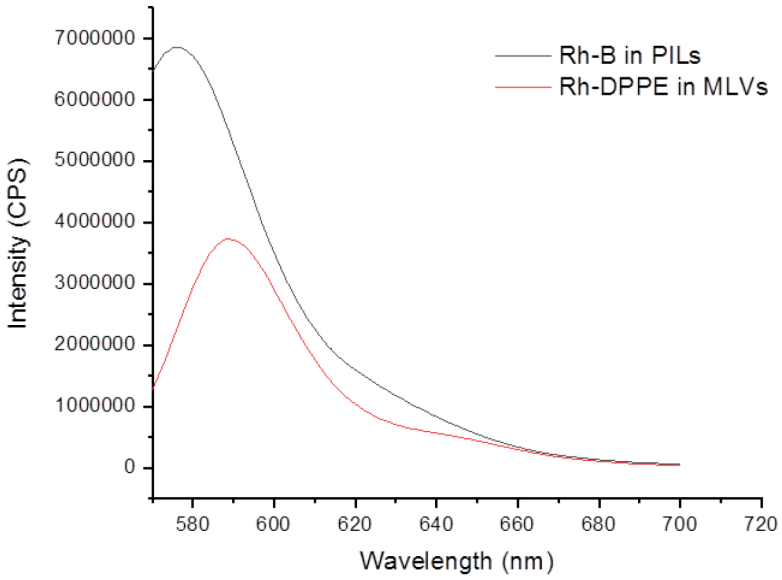

Fig. 4.12. Comparing emission spectra for Rh-PILs and Rh-DPPE MLVs, figure adapted from [143]. Example emission spectra for Rh-PILs and Rh-DPPE labelled MLVs at 0.9101 mg/l of Rhodamine dye in each sample. Obtained in Fluorimeter from excitation at 561 nm (slit width 1 nm), emission collected between 570-700 nm.

4.3 Results

The results in this chapter look with detail at the types of interactions that occur between poly(ionic liquid) nanoparticles (PILs) and GUVs of different membrane compositions. Before incubating the PIL nanoparticles with the GUVs, we first assessed the PILs' properties using both analysis of TEM images and zeta-potential measurements for their size and surface charge respectively. Both of these methods have been described earlier in the chapter (4.2.3). DLS data for the size was also provided by W. Zhang. The size of the PILs in the dried state is 24.0 ± 6.5 nm (TEM images) and 27.8 nm ±10.1 nm in a dispersion state (DLS). The size of the Rh-PILs (introduced later in section 4.3.3) was measured from TEM images to be 37 ± 11 nm; a typical TEM image for this sample from which this value was measured is shown in Fig. 4.13 A. The PILs have a positive surface charge of 45.1 ± 0.9 mV, see Fig. 4.13 B.

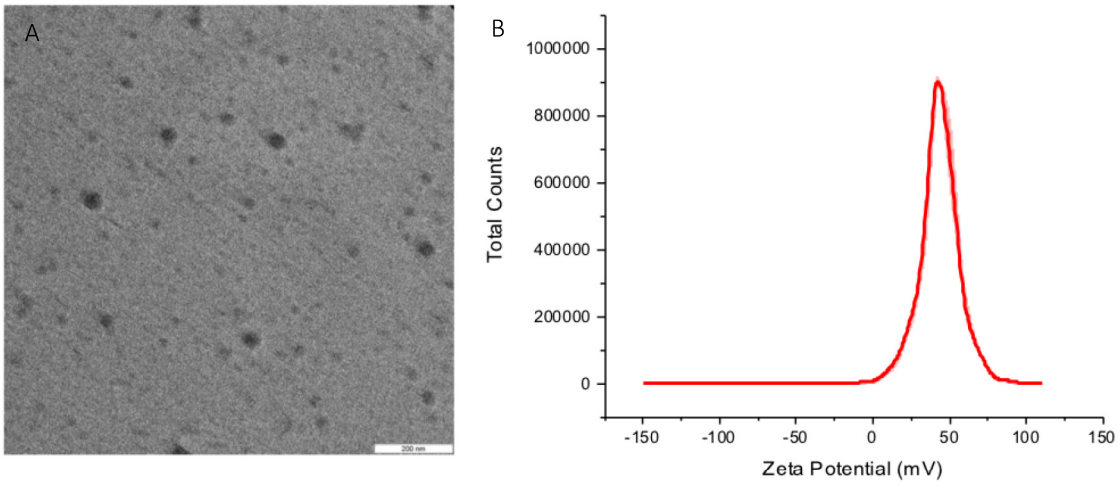

Fig. 4.13. Characterisation of the PILs using TEM images and zeta-potential measurements; figure adapted from [143]. A) TEM images of Rh-PILs that were used to determine the PILs' size. B) Zeta-potential measurement of the PILs' sample.

4.3.1 PILs induce vesicle leakage

The PILs were incubated with GUVs that had been prepared such that they contained different molar fractions of the neutral lipid dioleoylphosphatidylcholine (DOPC) and the negatively charged lipid dioleoylphosphatidylglycerol (DOPG). These compositions were used with the aim of mimicking the composition of mammalian and bacterial membranes, respectively.[156] In initial experiments, GUVs composed of DOPC:DOPG in a 9:1 molar ratio, where the DOPG lipid contributed a negative charge to the membrane, were prepared following the electroformation protocol outlined in Chapter 2.2.1. When the GUVs grown in sucrose were diluted in glucose, the sugar asymmetry across the GUV membrane aided visualization due to the difference in refractive indices when viewed in phase contrast mode, Fig 4.14 A (before). Apart from providing osmotic stabilisation, the heavier inner solution also causes sedimentation which facilitates imaging. When the sample was instead incubated with glucose containing 5 μM of PILs (1 hour incubation), an exchange of solutions across the vesicle membrane occurs, as evidenced in Fig 4.14 A (after) by the loss of contrast. The concentration of the PILs refers to the total polymer concentration in the samples. External and internal solution exchange indicates the

formation of nanometer pores which allow the exchange of the sugar molecules across the membrane. In addition, the number of surviving vesicles after incubation with PILs was observed qualitatively to decrease, suggesting that some of the vesicles have burst.

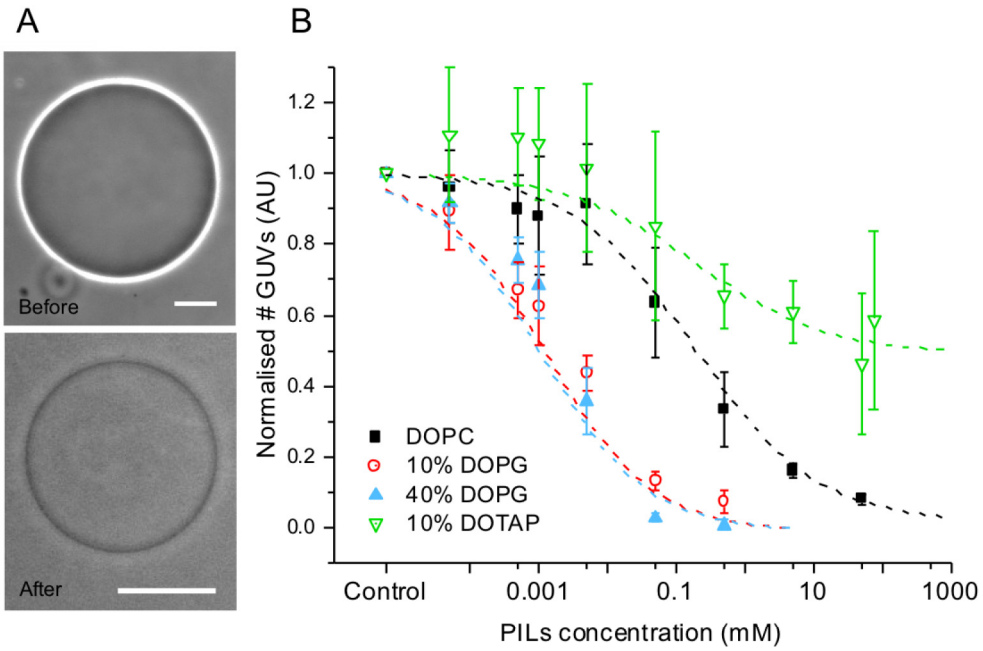

Fig. 4.14. Permeation and bursting of GUVs in presence of PILs, adapted from [143]. (A) GUVs composed of DOPC/DOPG (90/10 mol%) viewed before and after incubation with 5 µM PILs. When viewed with phase contrast, vesicles initially have a difference in refractive index between their inner and outer solutions and appear dark with a light halo. After incubation with PILs they lose this refractive index difference. Scale bars: 10 µm. (B) Plot of the number of surviving vesicles after incubation with PILs solutions. The data is shown here for an average over three separate experiments for each of the membrane compositions (raw data can be found in Fig. S7.3). The curves are a guide for the eye and are produced by fitting the averaged data with a growth/sigmoidal curve function in Origin.

The role of membrane charge and particle concentration was further probed by incubating varying PILs concentrations (from 0.5 µM to 90 mM) with GUVs composed of different molar percentages of lipids. We explored the following membrane compositions: pure DOPC (PC); DOPC/DOPG 90/10 mol% (10% PG); DOPC/DOPG 60/40 mol% (40% PG); DOPC/DOTAP 90/10 mol% (10% DOTAP). Of these lipids, DOPC is neutral, DOPG is negatively charged and DOTAP is positively charged (see Fig 2.1 in Chapter 2 for the lipids' structures).

Positively charged particles can act as a sticky agent between the GUVs and the negatively charged glass of the observation chambers, also resulting in vesicle rupture. To avoid this contact of the vesicles with the glass, before observation, the vesicles were immobilized in agarose (0.2% by weight) following a protocol introduced by Lira et al.[99] and has been described in Chapter 2.3. As a control, vesicles in the absence of PILs were also immobilized in the same way. Due to the vesicle leakage induced by PILs, the vesicles no longer sediment, thus, in addition to preventing adhesion, immobilization also freezes the vesicles, which allows for imaging and makes sure the same vesicles are not counted twice. The GUVs are immobilised randomly in all directions. We took stacks of images in the z-direction, from which we could examine the number of surviving vesicles

for a fixed sample volume. The number of surviving GUVs normalised by the number of control vesicles in the same volume was plotted as a function of particle concentration, Fig 4.14 B. We collected data from 3 samples of independently prepared vesicles. Vesicles were counted for all sizes above 4 μm and excluded if they had pronounced defects. Examples of vesicles that were counted and excluded can be found in Fig. 4.15.

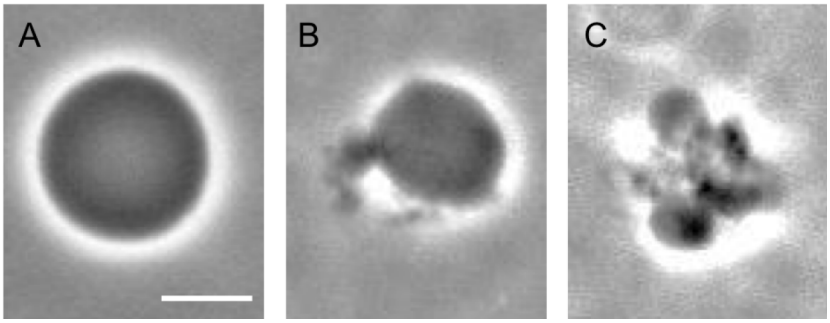

Fig. 4.15. Vesicles included and excluded when counting vesicles that survived at different PIL concentrations; adapted from [143]. A) Typical example of a vesicle that would be counted. B) & C) Typical examples of deformed vesicles/ vesicle aggregates that would not be counted. Scale bar 5 μm.

Each individual experiment produced a dataset with a specific relationship between number of vesicles and PILs concentration; in fact, all datasets could be fitted by the same growth/sigmoidal function. The number of GUVs in each experiment were individually analysed and normalised to the starting population. Note that the yield of vesicles prepared from different lipid mixtures varied significantly. The raw, averaged vesicle population data can be found in Fig S7.3. As the PIL concentration was increased, all lipid compositions experienced a decrease in population size. Notably, the onset of vesicle loss has a dependence on membrane charge, with negatively charged GUVs seeing a decrease in population at a lower PILs concentration than neutral and positively charged GUVs.

The poration and rupture of the vesicles that we observe due to the presence of the PILs could be due to an increase in membrane tension as it bends and wraps around the particles. The formation of membrane pores would then relieve this increased membrane tension and would also result in the reduction of internal volume. Short-lived pores (with lifetimes in the 10-100 ms range, as observed in phosphatidylcholine membranes upon electroporation[157]) are less likely to be the origin of the loss contrast as they reseal fast due to the high membrane edge tension,[158] which leaves the vesicle contrast preserved. We conclude that the membrane develops rather stable pores, which allow the observed full exchange of the internal and external solutions to occur within a period of a few seconds. For the interactions of antimicrobial peptides with GUVs, a similar poration effect is also reported (also observed in this instance by a loss of phase contrast).[159] Due to this similarity, we decided to assess the vesicle responses to the PILs using the same method; determining the minimum bursting concentration (MBC) of the PILs.[59] The MBC is here defined as the minimum concentration that is required to cause extensive GUV bursting (>90%). Using such a method is also biologically applicable, as it has been shown that values obtained for the MBC for GUVs can be directly compared with the minimum inhibitory concentration (MIC) on microorganisms, for example for

antimicrobial peptides, as shown in Refs. [59] and [160]. This comparison shows that using the lytic activity of GUVs is indeed a useful indicator for the action of antimicrobial peptides in vivo. From the data in Fig. 4.14 B, we were able to determine the MBC of PILs for each membrane composition; a summary of this can be found in Table 4.1.

Membrane composition	MBC (mM)	Error (St. Dev.)
40 % DOPG	0.03	0.01
10 % DOPG	0.19	0.10
Pure DOPC	42	14
10 % DOTAP	> 90	-

Table 4.1 The minimal bursting concentrations (MBC) of PILs acting on membranes with different lipid compositions, adapted from [143]. The MBC (concentration of PILs required to reduce the vesicle population by 90%) has a strong dependence on membrane charge, with positively charged particles (the same charge as the nanoparticles) being the most resistant (they do not fall below 90% for the experimental conditions possible). Similarly, we see that the more negative the membrane composition, the lower the PIL concentration required to reach the MBC.

For the negatively charged populations, there is not a distinct difference in their response to the PILs in terms of the MBC; both compositions reach their MBC within the concentration range of 0.03 – 0.2 mM. Taking the MBC (for 10% PG membranes) and comparing the vesicle survival rate at the same concentration for PC membranes, we see that at this concentration only 40% of the GUVs have been destroyed. The neutral membranes reach the MBC at 42±14 mM. One should note that the large error bars in Fig. 4.14 B are due to a relatively small starting population size for this lipid composition – DOTAP doped membranes are notoriously more difficult to form but also are not found in nature. The use of this positive lipid species helps us to probe the contribution that membrane composition has on the PIL-membrane interaction; it is clear that there is a strong dependence on charge, and that the electrostatic interactions facilitate at least the initial adhesion of the PILs to the vesicles.

If these particles are to be used in a biological context, especially as an anti-bacterial agent, it is important to consider how these interactions we observe are relevant to this goal. Given that most bacterial membranes have an overall negative charge,[161] it is highly significant that the negative vesicles reach the 10% survival population at a concentration several order of magnitude lower than for neutral membranes (which represent the mammalian mimics). Due to the significant affinity for negative membranes that these positively charged particles exhibit, we believe that the interaction between the two is strongly mediated by membrane charge, and this is the source of the initial adhesion of the particles to the membrane.

The population results in Fig. 4.14 B show the number of surviving vesicles but are unable to provide further properties of their state after these interactions. We have already seen in Fig. 4.14 A that the nanoparticle incubation induced leakage and extensive morphological changes on the vesicles (see below). As such, we also investigated the change in size of the GUVs for the PC, 10% PG, 40% PG and 10% DOTAP compositions. We found that all compositions responded to the incubation with a

decrease in the average vesicle size as a function of PIL concentration, as shown in Fig 4.16 A. However, this change in size (normalised to the average size for each composition at 0 mM of PILs – the raw data can be found in Fig. S7.4) seems to only have a weak dependency on charge (Fig 4.16). For most concentrations, the negatively charged populations have smaller average sizes than for PC and 10% DOTAP membranes; however, their sizes still fall within the error bars (standard deviation) of the neutral and positively charged membranes. When we examine the distribution of vesicle sizes shown in Fig 4.16 B for the 10% PG membrane composition, one can see that the larger vesicles are either destroyed or have a decrease in size due to interactions with the particles.

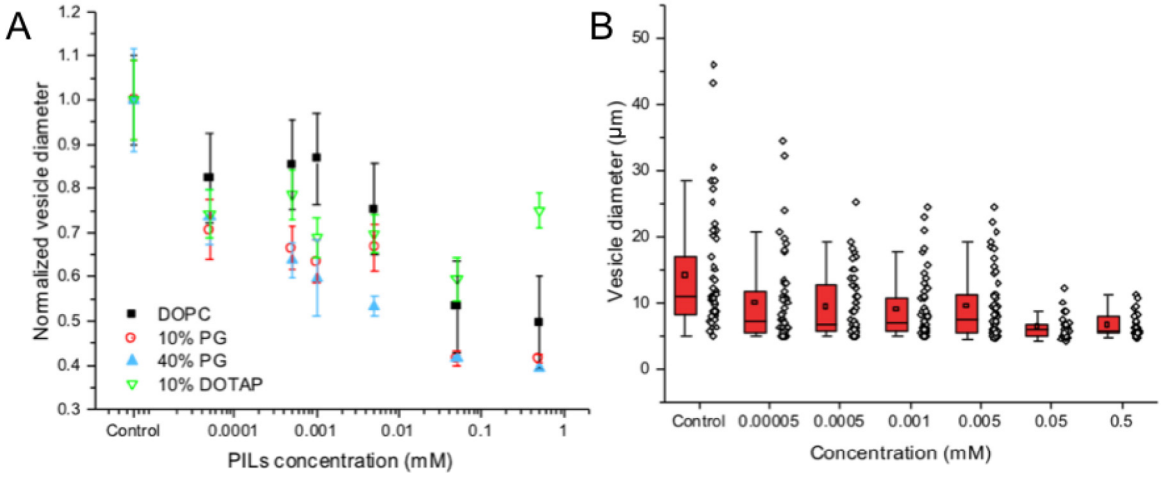

Fig. 4.16. GUV response to PILs incubation, represented by vesicle diameter as a function of PILs concentration; adapted from [143]. A) Normalised (to the average diameter for vesicles prior to incubation) vesicle sizes as a function of increasing nanoparticle concentration for all investigated lipid compositions. With increasing PILs concentrations, we observe a decrease in average GUV size, with no strong dependence on membrane charge. B) When examining the relationship more closely between vesicle size and particle concentration, for 10% PG membranes, we see that the larger GUVs are destroyed or decrease in size due to nanoparticle interactions.

4.3.2 Dynamics of GUV response to PILs

One of the drawbacks of the type of bulk assays used previously, is the lack of information regarding the changes the vesicles have undergone to reach the state that we view them in after incubation. As such, we used a microfluidic device to observe the PILs-membrane interactions as the PILs were introduced to a trapped population of GUVs. In addition to being able to observe the same population of GUVs, the setup also allows us to track the interactions while complete fluid exchange is performed. A detail on the preparation and use of the microfluidic setup has been described earlier in Chapter 4.2.4. For use here, after the initial preparatory steps (see earlier section 4.2.4), the device was filled with 10% PG vesicles, as this membrane composition was previously shown to be more affected by the nanoparticles. An osmotically matched glucose solution was flushed in to the device to induce contrast. The addition of glucose before the PILs results in different solutions internally and externally, as visualised by the dark interior and light halo (previously described in Chapter 2.4.1). A solution of PILs at 0.1 mM was then

introduced while recording the interactions. We expected that we would be able to watch the exchange of solutions “live”; we had previously inferred such solution exchange from the appearance of the vesicles before and after the incubation with PILs (Fig. 4.14 A). After the addition of the PILs to the microfluidic device, a significant number of the GUVs are destroyed. The particles may mediate adhesion of the vesicles to the glass leading to tension increase and rupture. The typical interactions that the vesicles underwent have been summarised into three different interaction pathways in Fig. 4.17.

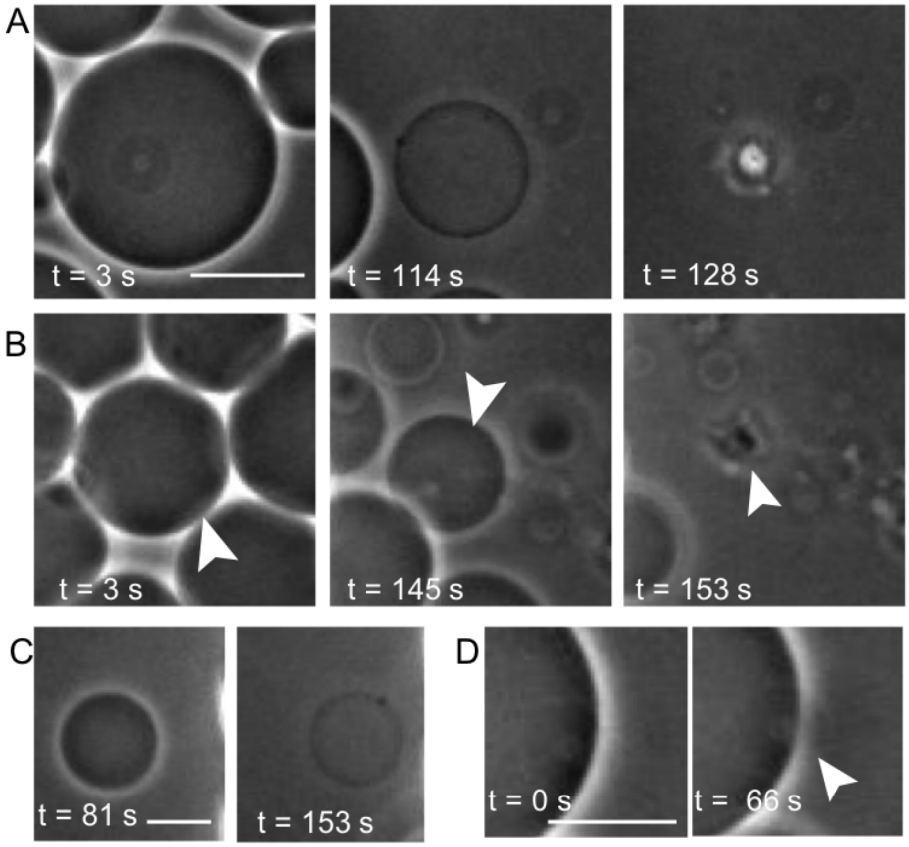

Fig. 4.17. 10% DOPG GUV responses to the addition of 0.1 mM PILs, as observed in a microfludidc chamber (the nanoparticles are introduced from the right), adapted from [143]. We observed different vesicle responses. A) Vesicle size decrease, membrane becomes permeable, vesicle eventually bursts. B) Vesicle size decrease, contrast is retained, vesicle bursts. Arrow indicates the vesicle of interest throughout the time sequence. C) Slight decrease in vesicle size, contrast across membrane is lost, but vesicle remains intact throughout observation. D) (Macro)pore formation in a vesicle with preserved contrast; the pore can be observed by the changes in the bright halo surrounding the vesicle, which appears interrupted in the region of the pore. Scale bars 15 μm.

We observed: a loss of phase contrast and simultaneous reduction in vesicle diameter, ending in vesicle destruction (Fig. 4.17 A); preserved phase contrast, but the vesicle diameter decreases until the vesicle is destroyed (Fig. 4.17 B); and loss of phase contrast, but the vesicle size remains almost constant throughout observation and the vesicle is not destroyed (Fig. 4.17 C). There were also visible instances of (macro)pore formation, as can be seen in Fig. 4.17 D. Such (macro)pores are at least one of the causes of the observed membrane leakage.

The different responses of the GUVs could be caused by different factors, such as (i) the membrane properties on a vesicle-to-vesicle scale, as the preparation protocol offers limited control over lipid composition at the individual vesicle level[162,163] or (ii) previous bursting of vesicles that then spread on the glass, thus generating differences in the chamber surface properties which would then prevent other vesicles from bursting due to particle-mediated adhesion to the glass. Another factor that could determine the different types of vesicle response is the initial membrane tension; this tension can significantly vary from 10^{-6} mN/m to 1 mN/m. Therefore, vesicles with more excess area (low tension) could possibly wrap the particles, while tense ones may only need to come into contact with a few particles to reach lysis tension of approximately 5-10 mN/m[164] and then subsequently burst.

We also observed a vesicle-to-vesicle variation for losing or retaining contrast; this suggests that different types of pores are forming. For the vesicle size to decrease, such as in Figs. 4.17 A and B, the internal volume of the GUV needs to decrease. This is most likely through the expulsion of the internal sucrose solution. However, in Fig. 4.17 A, not only do we observe this decrease in size, but we also see a loss of contrast. For this loss of contrast to occur, the solutions inside and outside of the GUVs need to be the same. This could suggest that the membrane also forms more stable/longer-lived pores to allow full mixing of the solutions across the membrane. The use of the microfluidic device, although incredibly useful for controlling the addition of PILs and observing the interactions directly, meant we could not avoid contact between the vesicles and the substrate. This contact may have additionally contributed to the membrane tension via adhesion of the GUVs to the glass (as mediated by the particles).

4.3.3 Membrane coverage of PILs

Both the bulk experiments and the microfluidic observations showed us how the PILs affect the vesicle populations. Next, we attempted to characterise the surface concentration of PIL on the GUVs. To do so, the PILs were labelled with the fluorescent dye Rhodamine-B (the experimental details of this labelling process were described previously in Chapter 4.2.3). We confirmed that the labelling process and the presence of the dye in the PILs structure did not interfere with the interactions of the PILs with the GUVs by repeating the statistical experiments for the number of GUVs at different PILs concentrations. From the data presented in Fig. S7.5, we can see that the number of surviving vesicles exhibits the same trend with increasing PILs concentrations for the labelled and non-labelled samples alike. As such, we can assume that the presence of the dye does not impinge on the interaction between the membranes and the PILs. Confocal microscopy observations of the GUVs incubated with Rh-PILs (1 hr incubation time) revealed that in fact the PILs were located both on the vesicle membrane and at the vesicle interior. In this section of the chapter we evaluate the data for the PILs at the membrane; in the subsequent section we look at measurements for the PILs inside the GUVs.

Fig. 4.18 A-D shows the fluorescence from non-labelled membranes after incubation with PILs solutions of different concentrations. The fluorescent signal demonstrates that the PILs enrich on the membranes (at concentrations that cause leakage and size decrease of the vesicles). The source of the fluorescent signal can be purely attributed to the dye in the PILs' structures, as the GUVs were prepared in the absence of dye. The control

images of the non-labelled GUVs used in this experiment can be found in Fig. S7.6 and demonstrate that there is no/only background fluorescent signal.

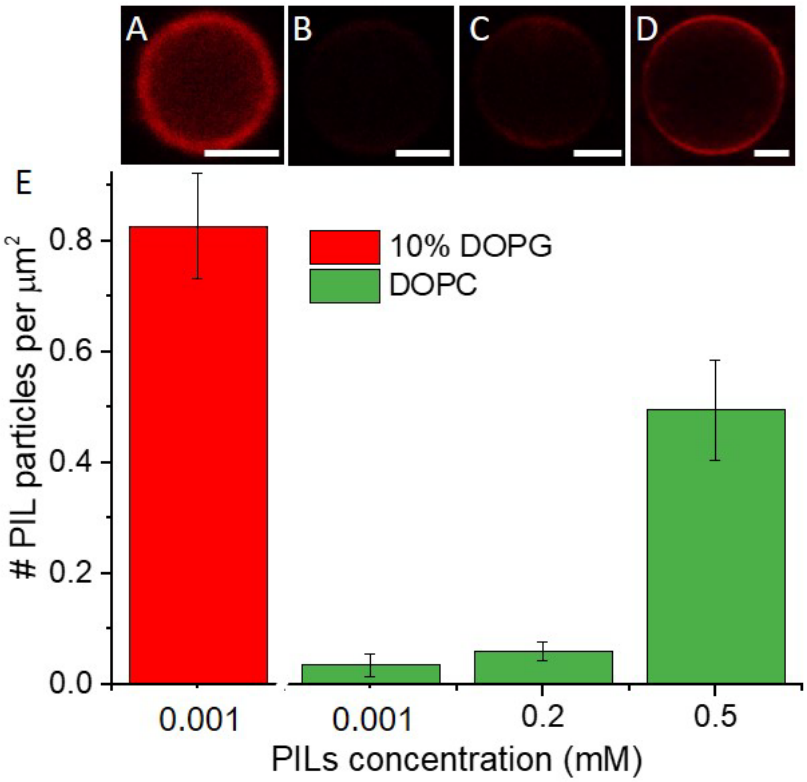

Fig. 4.18. Fluorescently labelled PILs on unlabelled GUV membranes of different compositions and the area occupied per PIL particle calculated from such images; figure adapted from [143]. A) 0.001 mM Rh-PILs on 10% DOPG GUV. B) 0.001 mM Rh-PILs on DOPC GUV. C) 0.2 mM PILs on DOPC GUV. D) 0.5 mM PILs on DOPC GUV. Scale bars: 5 μm. E) Number of PILs per 1 μm^2 membrane area. The error bars represent the standard errors determined from 9-10 vesicles per composition/concentration.

If we look first at the intensity values from the PILs on the membranes, we can already see a difference between vesicles with different lipid compositions (Images A and B, Fig. 4.18). For the same concentration of PILs (0.001 mM), the measured membrane intensities were 21.23 ± 12.75 AU for the 10% DOPG membrane and 2.82 ±1.81 for the DOPC membranes. The intensity of the 10% DOPG membranes is larger by an order of magnitude. These values were obtained by measuring the average pixel intensity for a fixed section of membrane (taking care to account for any dye polarisation effects or membrane defects); this process has been described earlier in this chapter in section 4.2.6. If the nanoparticle concentration is then increased to 0.5 mM (a concentration at which approximately 50% of the DOPC population has been destroyed, as is also the case for 10% DOPG vesicles at 0.001 mM; refer back to Fig. 4.9), the average membrane intensity increases to 13.71 ± 6.44. However, this is still notably lower than the intensity for the 10% DOPG membranes at a much lower PILs concentration. The intensity values are naturally related to the number of nanoparticles at the membrane, which we now go on to quantify.

4.3.3.1 Quantifying the number of bound PILs

First, to be able to determine the number of nanoparticles on the membrane from the Rh-PILs' intensities, we needed to know the labelling efficiency of the Rhodamine-B in the PILs. To do so, we dissolved the particles in ethanol and measured the solution absorbance, which then could then be converted to a concentration using the Beer-Lambert Law:

$$A = \epsilon \cdot l \cdot c \tag{13}$$

where A is the measured absorbance, ϵ is the wavelength-dependent molar absorptivity coefficient, l is the path length through the sample and c is the sample concentration. The concentration of the Rh-B in 14.96 mg/ml PILs was found to be 9.1×10^{-4} mg/ml. We determined the ratio between the number of Rh-B molecules and the number of PILs particles as follows. First, the diameter (d) of the particles from TEM images (see Fig. 4.2 and description in section 4.2.3) was found to be 37 ± 11 nm, which gave a volume (V) of a single particle as 2.65×10^{-17} ml. The mass of a single particle (m_{PILs}) was calculated using, $m_{PILs} = \rho \times V$, (the particle density is $\rho = 1.137 \pm 0.003$ g/ml, see section 4.2.3 for a brief measurement description) and found to be $3.01 \times 10^{-14}\ mg$. The number density of PILs (n_{PILs}) was then calculated using,

$$n_{PILs} = \frac{[PILs]}{m_{PILs}} = 4.97 \times 10^{14}\ \text{particles}/ml \tag{14}$$

where $[PILs]$ is the total PILs concentration given as $14.96\ mg/ml$. The concentration of Rh-B measured by absorbance was $[RhB] = 0.00091 mg/ml = 1.8998 \times 10^{-6} mol/L$, which gives the number density of Rh-B (n_{RhB}) as

$$n_{RhB} = [RhB] \times N_A = 1.14 \times 10^{15}\ molecules/ml \tag{15}$$

Therefore, the number of Rh-B molecules to PILs particles was calculated using:

$$\frac{n_{RhB}}{n_{PILs}} = \frac{1.14 \times 10^{15}}{4.97 \times 10^{14}} = 2.3\ RhB/particle \tag{16}$$

We next needed to convert the intensity that we measured on the membrane (values given in previous section of this chapter) to a Rh-B concentration. For this we used vesicles labelled with known concentrations of a similar fluorophore, Lissamine Rhodamine-B dipalmitoylphosphatidylcholinne (Rh-DPPE), to generate a calibration curve of membrane intensity as a function of Rh-DPPE concentration. This graph is shown in Fig. 4.19. The difference in the fluorophores' natures and fluorescence performances was accounted for by comparing the emission spectra of multi-lamellar vesicles (MLVs) doped with Rh-DPPE and Rh-PILs, as has been described in further detail in section 4.2.8.

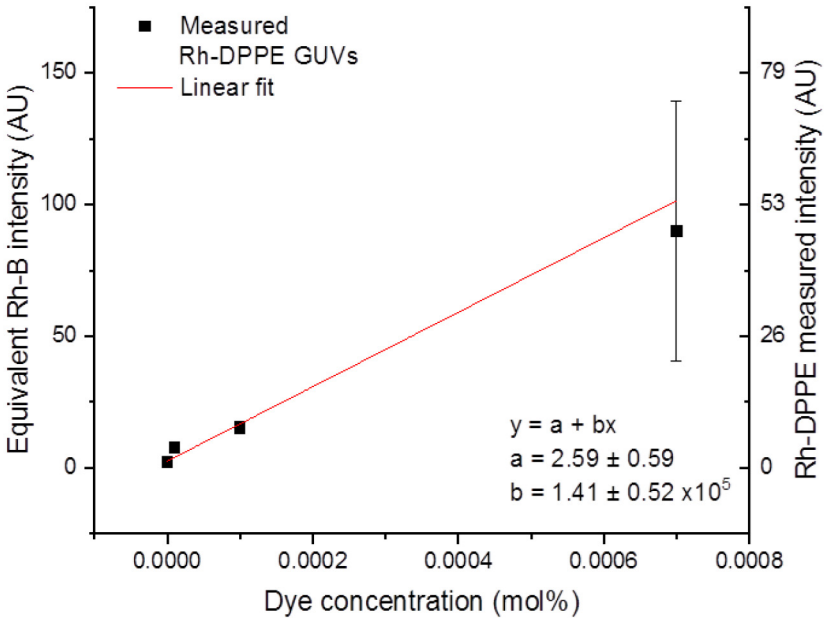

Fig. 4.19. Calibration curve of the measured fluorescence intensity of GUVs (left axis) as a function of Lissamine Rhodamine-B DPPE (Rh-DPPE) concentration in their membrane; figure adapted from [143]. The Rh-DPPE concentration was varied from 0 to 0.004 mol%. The GUV fluorescence intensities were then converted to equivalent Rh-B intensities (right axis) based on the fluorescence correction factor between these two dyes as assessed in Fig. 4.12. The linear fit (red line) of the equivalent Rh-B intensities can be subsequently used to determine the concentration of Rh-B in the membrane from the fluorescence intensities of GUVs in the presence of Rh-PILs as measured in the main text.

From the calibration curve in Fig. 4.19, which is also shown with the equivalent Rh-B intensity on the left-hand axis, we could calculate the Rh-B concentration on the GUV membranes:

$$[RhB_{membrane}] = \frac{Intensity - 2.59}{1.41}\ mol\% \tag{17}$$

where the values for *intensity* are the measured y-values for the intensity of the Rh-DPPE GUVs and the numerical values are obtained from the fit of the curve in Fig. 4.14. Considering the particle labelling efficiency, this was then converted to the concentration of PILs on the membrane:

$$[PILs_{membrane}] = \frac{[RhB_{membrane}]}{\frac{n_{RhB}}{n_{PILs}}} mol\% \tag{18}$$

where the ratio $\frac{n_{RhB}}{n_{PILs}}$ has been previously defined in equation 13. Finally, the area per PIL was determined by taking the area of 0.7 nm^2 to be that occupied by a single DOPC lipid headgroup[165] and using the following relation:

$$Area\ per\ PIL = \frac{100\ (lipids)}{[PILs_{membrane}](mol\%)} \times 0.7\ nm^2 \tag{19}$$

from which the number density of PILs per membrane area is calculated, which is the data presented in Fig. 4.18 E. This data indicates that the particle density increases with increasing PILs concentration (for the PC membranes). However, the largest value of surface density, ~1 particle per 1 μm^2 for 10% DOPG membranes with 0.001 mM PILs, is relatively small when one considers the small size of the particles. Comparing the two different membrane compositions at 0.001 mM (DOPC and 10% DOPG), we see that the surface charge of the membrane corresponds with the binding efficiency of the particles (greater affinity for oppositely charged membranes). We note here that these values for surface coverage should be considered with caution. Although the average vesicle diameters (Fig. 4.16) do follow a similar trend between the different membrane compositions, we do not know the individual histories for the vesicles analysed in Fig. 4.18. Additionally, we calculate the areas here as projected areas as excess area of the GUVs may have been used to enwrap the particles, with the membrane folding on itself.

4.3.3.2 Behaviour of dye intensity values on the vesicle membranes

We also observed a scatter in the intensity values within a population of GUVs with Rh-PILs, as can be seen in Fig. 4.20. The scatter for the 10% DOPG with 0.001 mM PILs sample are larger than for the DOPC with 0.5 mM PILs which could be due to a non-uniform distribution of charged lipids between vesicles, resulting in some vesicles with a larger net charge than others. A similar observation was made during the microfluidics experiments, where we see different vesicle responses to the PILs within the same sample. In the case of the vesicles in the microfluidic trap the response is immediately recorded and not all of them are simultaneously exposed to the exact same PILs concentration, which could explain the difference in morphological changes that we observe. However, for the coverage of the fluorescent PILs on the membranes, these images are obtained after incubation for 1 h, which should allow the system to equilibrate. Again, we should also consider that the exact histories of the GUVs are not known; properties such as tension and excess area can vary on a vesicle-to-vesicle basis.

While observing the Rh-PILs on the GUV membranes, we also noticed that the intensity varied over the vesicle as a function of angle, where the poles of the GUVs had the maximum intensities. We observed this polarisation effect for all vesicles in the DOPC with 0.5 mM PILs sample, as can be seen in Fig. 4.21 A. For the 10% DOPG membranes with 0.001 mM PILs we did not observe such angular dependence for the membrane intensities, but rather a homogeneous fluorescence over the whole vesicle contour. Additional line profiles for both samples can be found in **Fig. S7.7.** We also observed such polarisation effects for small DOPC GUVs (data not included here), so this effect is not dependent on the size of vesicle that is measured.

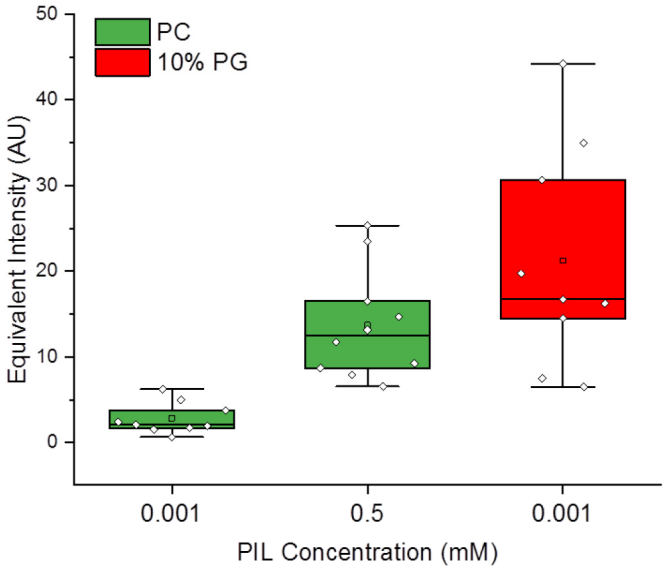

Fig. 4.20 Intensity measurements for fluorescently labelled PILs on DOPC and 10% DOPG membranes; figure adapted from [143]. The graph shows how the broad the spread of the data was for the different membrane intensities measured within the samples.

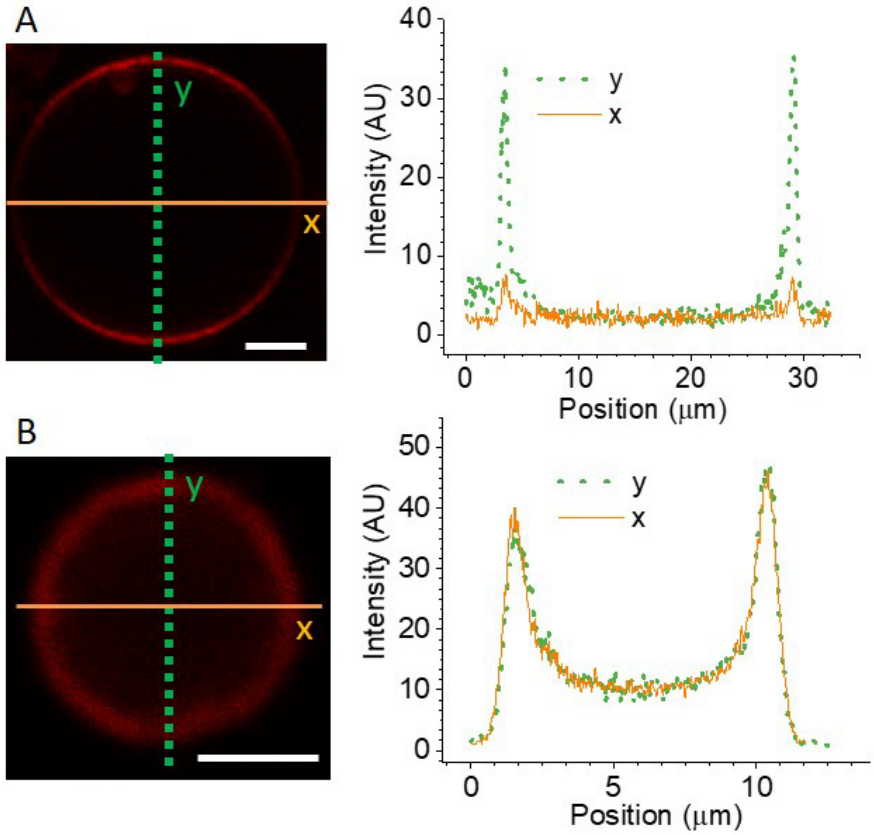

Fig. 4.21 Fluorescence of Rh-PILs on GUV membranes varies as a function of angle; figure adapted from [143]. A) Polarization effect exhibited as strong angular dependence of the intensity of Rh-B in the PILs along a DOPC vesicle membrane, as emphasized with the line profiles (right) along the respective dashed lines indicated on the image. B) 10% DOPG membranes with no observed polarization effects. The intensity line profiles were generated for a 2 μm-wide stripe in the vertical and horizontal direction. Scale bars: 5 μm.

Such angular dependence of membrane fluorescence intensity has been observed previously,[166] and so this observation may initially seem trivial. However, this difference in intensity between the 10% DOPG and DOPC sample may actually be hiding an important piece of information about the interactions in these two samples. The difference between these two lipid compositions is that the 10% DOPG membranes carry a negative charge; this result could indicate that there is charge dependence for how the nanoparticles interact with the membrane and that there could in fact be different interaction mechanisms. The angle-dependent intensity is a result of the dye orientation with respect to the polarization plane of the excitation light, known as the photoselection effect. When fluorophores are illuminated by linearly polarized light, those with transition moments orientated in the same direction as the incident light will be preferentially excited.[167] There is a dependence of $\cos^2\theta$ for this phenomenon, where the angle θ is the angle between the polarization of the incident light and the transition moment of the dye. When the orientation of a Rhodamine dye is coupled to the membrane normal, GUVs have been observed to exhibit photoselection in their intensities.[166] During the synthesis of the labelled PILs, the dye should be incorporated between the layers with no preferred orientation. Even if the rhodamine-B molecules did incorporate with specific alignment to the internal structural elements of the PILs, this effect should be negated by the concentric circular structure of the particles. The photoselection suggests that these membranes have an interaction with the PILs such that the particle restructures in a way that allows the rhodamine-B to translocate to the membrane (as the molecules are lipophilic)[168], and align with the membrane normal. Considering the 10% DOPG membranes, the stronger electrostatic interaction between the negatively charged membrane and positively charged polymer could instead result in rapid engulfment. The membrane quickly wraps the nanoparticles, leaving their structures intact and the rhodamine-B orientated randomly inside. Indeed, the significant decrease in vesicle size could be a result of area loss due to involvement in complete engulfment of the particles.

4.3.4 Uptake of PILs to GUV interior

We also measured the fluorescence intensity from the rhodamine-B in the PILs at the interior of the GUVs. We exposed DOPC GUVs to 1 mM of Rh-PILs. Similar measurements on 10% DOPG membranes were not feasible due to the small size, as discussed below. Increasing the concentration of the nanoparticles to 1 mM helped to overcome the poor labelling efficiency of the PILs; at insufficient concentrations we may not have been able to detect any signal from the dye (a false negative result). We plotted radial intensity profiles of the confocal cross-sections of the GUVs; the method is described in further detail in section 4.2.6 of this chapter). Radially averaging is helpful as it not only provides an average intensity from a larger portion of the membrane (compared to straight-line averages) but it also negates any effects from the polarisation of the dye, as previously discussed. To avoid interpreting out-of-focus membrane intensity as signal from free Rh-PILs inside the vesicles, we compared these measurements to intensity profiles for PIL-free GUVs of a similar size but labelled with 0.05 mol% Rh-DPPE. The out-of-focus signal in the interior scales inversely with vesicle size, with smaller vesicles having a larger contribution at their centre than larger vesicles, as can be seen in Fig. 4.22. Therefore, we made sure to measure Rh-DPPE labelled vesicles that had a comparable size range to the GUVs with Rh-PILs (8 – 15 μm).

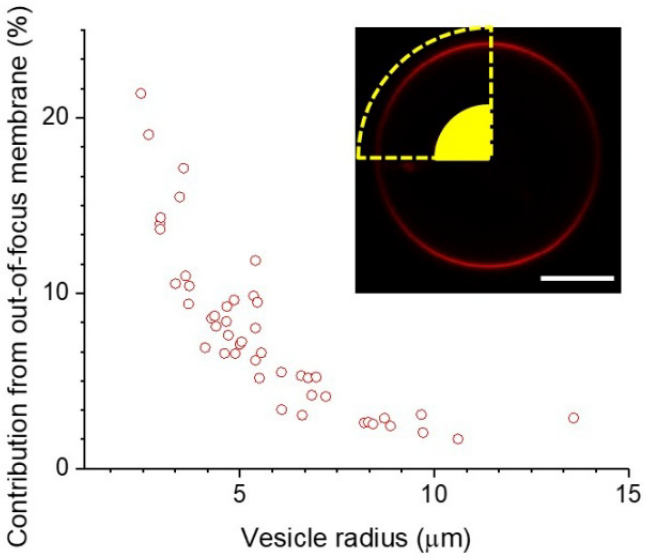

Fig. 4.22. Plot showing membrane interior intensity for the 1st 40% of the distance from the center to the vesicle radius as a function of vesicle size; adapted from [143]. We measured vesicle intensities for GUVs of different sizes. Then, we calculated the average intensity for the central 40% of the vesicle (counting from the center outwards) and determine what percentage this region is of the maximum membrane intensity value (segment in diagram is for illustrative purposes only, showing this 40%). We plotted these values as a function of vesicle size, clearly demonstrating the increased contribution of out-of-focus fluorescence for smaller vesicles at the vesicle interior. Scale bar on confocal inset 5 μm.

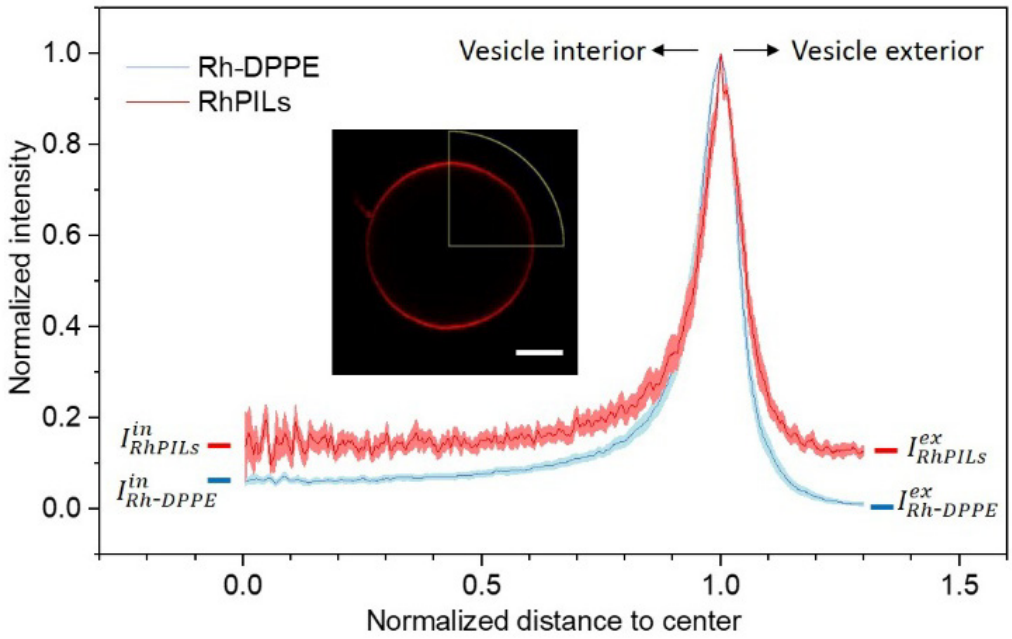

Fig. 4.23. Measuring fluorescent intensity from Rh-PILs inside GUVs; adapted from [143]. Radial profile of the fluorescence intensity signal averaged over the vesicle azimuthal angle and normalized by the maximum value as a function of distance from vesicle center normalized by vesicle size for Rh-DPPE labelled GUVs (blue curve) and DOPC GUVs incubated with 1 mM Rh-PILs (red). The intensity values show signal averaged from measurements on 10 GUVs, with the standard deviation shown as the error on the curves (pink and light-blue band).

The data displayed in Fig. 4.23 shows the averaged intensities for both experiments (obtained from 10 GUVs for each experiment). The values on the y axis are normalised by the intensity value of the membrane and the values on the x axis are normalised by the position of the membrane. From the flat region of the graph for values on the x axis of radii $0<x<0.4$, we took an average intensity at the vesicle interior for both the Rh-PILs and Rh-DPPE curves. The values for I^{in}_{RhPILs} and $I^{in}_{Rh-DPPE}$ correspond to the interior intensities from the PILs and the out-of-focus membrane respectively. The data from the Rh-DPPE vesicles demonstrates the out-of-focus contribution, as the interior signal is higher than that outside, $I^{in}_{Rh-DPPE} > I^{ex}_{Rh-DPPE}$. However, the interior signal for the vesicles with Rh-PILs is even higher $I^{in}_{RhPILs} > I^{in}_{Rh-DPPE}$ than the labelled membranes without Rh-PILs, suggesting that there is signal from Rh-PILs in the vesicle interior. The effective intensity from PILs inside the vesicles can be expressed as the difference $I^{in}_{eff} = I^{in}_{RhPILs} - I^{in}_{Rh-DPPE}$. Similarly, for the exterior of the membrane, $I^{ex}_{eff} = I^{ex}_{RhPILs} - I^{ex}_{Rh-DPPE}$ describes the effective intensity from the PILs outside the vesicles. When we compared these two values, we determined that the intensity at the vesicle interior is 70.3 ± 20.4 % of the external intensity value, where this external intensity value is the contribution from the free Rh-PILs at 1mM with DOPC vesicles. The intensity value that we measure at the vesicle interiors strongly indicates that the particles have crossed the membrane. This is likely to happen during the formation of membrane pores, as we have observed both directly via the microfluidic experiments, and indirectly through the exchange of sugars across the membrane. This measurement also implies that either the pores formed on the membrane have a size large enough to permit PIL nanoparticles to travel through them, or that lipid-wrapped particles detach from the vesicle membrane (after being wrapped by it). However, when we repeat this experiment with non-labelled particles and a fluorescently labelled membrane, we do not detect any signal from membrane dye at the vesicle interior (see Fig. S7.8). This suggests that bare (lipid-free) particles permeate through the membrane pores in order to reach the vesicle interior.

4.3.5 PILs cause changes in membrane properties

When the GUVs were exposed to the PILs we also observed changes in the vesicles' appearance, as can be seen in Fig. 4.24. In the absence of PILs, Rh-DPPE labelled DOPC GUVs appear smooth and without many defects as in image A (3D confocal projection). When the PILs are introduced membranes defects are now visible, as in the 3D confocal projection in B and the phase contrast image in C. The defects represent lipid aggregates that are co-localised (in the case of image B) with increased signal from Rh-PILs. Defects like these can also be seen in the phase contrast images of GUVs after incubation with PILs (Fig. 4.24 C). These aggregates with increased optical density could be due to membrane wrapping around the nanoparticles and lipid accumulation in their vicinity. The size of these defects is well above the average size of the nanoparticles; as such, it could also be possible that upon docking to the membrane, some of the particles cooperatively wrap into clusters. Such effects have been shown previously both in simulations[169] and experimentally with micron-sized particles.[51,52]Regions of dense membrane have also been observed when GUVs are exposed to membrane active peptides and agents.[137,140,141,170] This behaviour is often observed throughout the literature for cationic membrane-active molecules. A mechanism proposed to explain this observation depicts the membrane active agents behaving as an intermediate sticky contact between two folded pieces of membrane.[171]

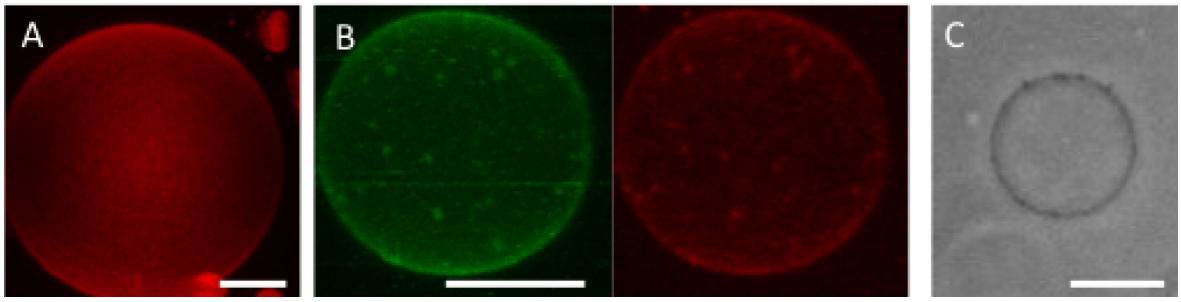

Fig. 4.24. Morphological membrane changes caused by PILs; adapted from [143]. (A) In the absence of PILs, vesicle membranes typically exhibit a smooth surface, as shown in the 3D projection from confocal images of a DOPC vesicle. (B) When exposed to 0.1 mM PILs, these membranes develop lipid clusters and inclusions characterized by the high-intensity spots (NBD-PC labelled membrane in green, Rh-PILs in red). (C) Similar membrane defects can also be observed in phase contrast. Scale bars = 5 μm.

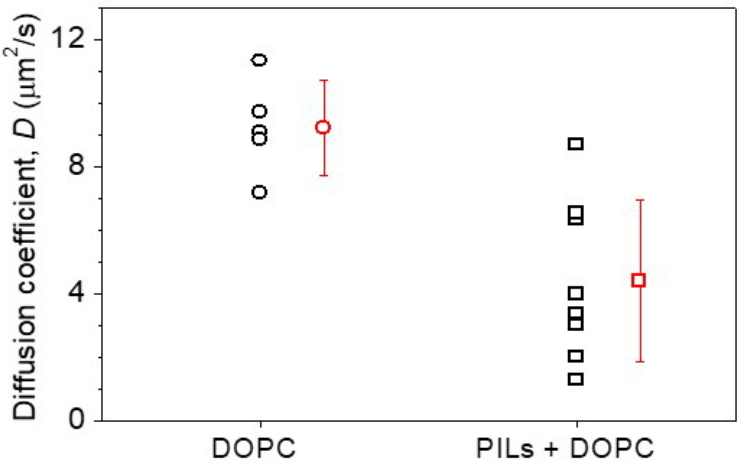

Fig. 4.25 Diffusion in DOPC membranes in the presence of PILs slows down; figure adapted in [143]. Lipid diffusion was measured using FRAP of DOPC membranes labelled with 0.1 mol% Rh-DPPE with and without 0.1 mM PILs. The black symbols indicate the measurements from individual vesicles; the mean and standard deviation for the two conditions are given in red. A larger scatter was observed for the PIL containing sample.

Within the context of membrane properties, we also observed a decrease in lipid fluidity in the presence of PILs. This was assessed using a technique called fluorescence recovery after photobleaching (FRAP) and the method has been described in detail in section 4.2.7. FRAP is commonly used to measure changes in membrane fluidity by placing the fluorophore in different environments. This has many direct biological implications as long-range lipid diffusion is vital to many membrane processes.[172,173] For DOPC (0.1 mol% Rh-DPPE labelled) GUVs incubated with 0.1 mM PILs, we observed a decrease in the average lipid diffusion coefficient, from 9.2 ± 1.5 $\mu m^2/s$ (for vesicles in the absence of PILs) to 4.4 ± 2.5 $\mu m^2/s$, see Fig. 4.25. This indicates that the PILs interact with the membrane in such a way as to impinge on the movement of lipids. This could be a sign of particle insertion into the bilayer creating obstacles that the lipids must diffuse around. Alternatively, the particles could condense or tightly bind many lipids simultaneously, such that a significant number are immobilized on the particle and diffuse slowly with it. The fraction of immobilised lipids during the course of the measurement (see Fig. 4.11), for the control and PIL-incubated vesicles (0.82 ± 0.03 and 0.74 ± 0.08, respectively) are similar within the error and indicate that the particles reduce the overall diffusion of lipids (or alternatively, the overall membrane state) without lipid immobilisation. In addition to the decrease in membrane diffusion, we also observed scatter in the diffusion coefficient values, with individual vesicles in the same sample exhibiting different lipid diffusion. This could be due to differences in properties, such as initial membrane tension modulating the PILs-membrane interaction, with some vesicles having more or less excess area for the interactions (resulting in partial wrapping, for example). We observed a similar spread of values for the membrane intensities (from the Rh-PILs at the membrane), as previously discussed, and shown in Fig. 4.20.

4.4 Discussion

4.4.1 PILs interaction mechanisms with biomembranes

These experimental findings, both individually and in conjunction with each other, lead us to speculate the potential interaction mechanisms of the PILs with the GUVs; schematic diagrams of the different proposed mechanisms can be found in Figs 4.26-4.27. The first stage of any interaction pathway that the PILs might have must be docking to the membrane. This is revealed by the use of the fluorescently labelled PILs in Fig 4.18. The fluorescent images of the PILs on the GUV membranes also imply that after this initial contact, the particles maintain this adhesion. Some particles might then experience engulfment by the membrane as well as clustering. The visible aggregates on the vesicle co-localized with signal from the membrane itself, as in Fig. 4.24, could be an indication of such a mechanism. See Fig. 4.26 for a simplified schematic of the engulfment and wrapping of the particles. This wrapping of the particles could also increase membrane tension, by reducing the vesicle surface area to volume ratio as more membrane is taken up to spread over the particle surface. Pore formation was inferred via the loss of phase contrast in Fig. 4.14 and directly observed during the microfluidic experiments in Fig. 4.17; this mechanism would allow the vesicle to reduce its volume. The formation of a (macro)pore would allow the GUV to expel some of its internal solution and thus reduce the tension on its membrane. The measurements obtained in Fig. 4.23, indicating fluorescence from the PILs at the GUV interior, could also be as a result of particles entering the GUVs through a pore. This, together with the complete exchange of solutions, as shown in Figs. 4.14 A (before/after) and 4.17 A, implies longer lived, more stable pores. Such pores would require stabilisation due to the high membrane edge tension.[158]

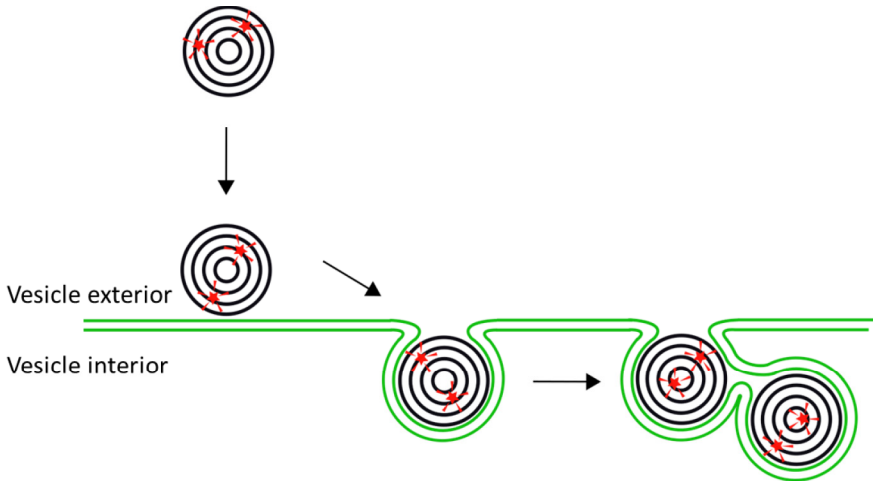

Fig. 4.26. Schematic diagram for adhesion and engulfment of PILs mechanism. Here, a Rh-PILs nanoparticle is shown adhering to the membrane and subsequently the vesicle membrane spreads over its surface. The potential clustering of these particles is also shown as a next step in the interaction. The green lines indicate the lipid bilayer and the black concentric circles represent the PILs particles; the size of these is approximately to scale for a bilayer thickness of 5 nm and a particle size of 37 nm. The red stars indicate the Rhodamine-B molecules. The arrows indicate how the mechanism progresses.

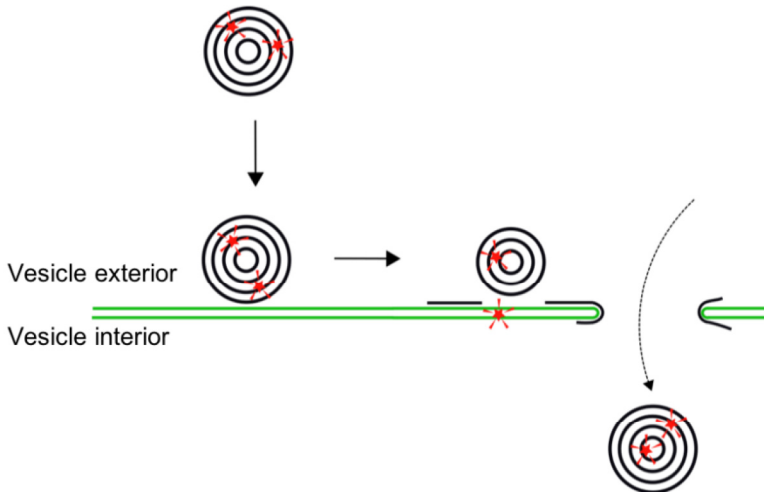

Fig. 4.27. Schematic diagram for adhesion and unwrapping of the particle structure leading to pore stabilisation. Upon adhesion to the membrane, the Rh-PIL nanoparticle starts to partially unwrap its outer structure, which both potentially releases dye molecules from between the layers and provides polymer for pore stabilisation (black arrows depict stages of mechanism). A Rh-PIL particle is shown entering to the GUV interior through such a pore (black dashed arrow).

We now speculate on two possible alternative mechanisms of this pore stabilisation; the unwrapping of the layer-like structure of the particle and the interactions of the polymer with the membrane generating regions of frustrated bilayer. For particle unwrapping, once the particle docks to the GUV membrane, the outer-most layer of polymer could unwrap from the main structure and provide polymer sections to stabilise the pores, as shown in Fig. 4.27. The pores do not reseal, and unbound particles are free to enter to the GUV interior.

A frustrated membrane refers to regions of the membrane that are incomplete or irregular, where the compact hydrophobic core is not completely shielded from the surrounding solutions due to other competing forces acting on the membrane.[174] For a frustrated bilayer to occur, once the particle adheres to the membrane surface, the lipids in the bilayer can incorporate between the particle layers due to the amphiphilic nature of both the polymer structure and the lipids themselves, and possibly electrostatic interactions between the positive particle and zwitterionic lipids. This could then lead to the particle being incorporated between the lipid layers or being wrapped by a frustrated bilayer, as tentatively illustrated in Fig. 4.28 B, which is ruptured in the particle vicinity. This defect could stabilise the pore. Such a process might be more favourable for the smaller particles in this poly-disperse sample.

Alternatively, the incorporation of (frustrated) lipids between the particle's layers could be a contributory factor to the particle unwrapping that has just been discussed. The lipids could swell the layer-like structure of the particle and effectively plasticise the particle. For plastics, plasticiser molecules behave by embedding themselves between the chains of the polymers, creating space between the chains and subsequently reducing the secondary forces between the polymers.[175] Swelling of the outer layer of the particle could cause it to expand and peel off from the main structure. These unwrapped portions of the polymer could then stabilise the pores in the lipid bilayer, as shown in Fig. 4.28 A.

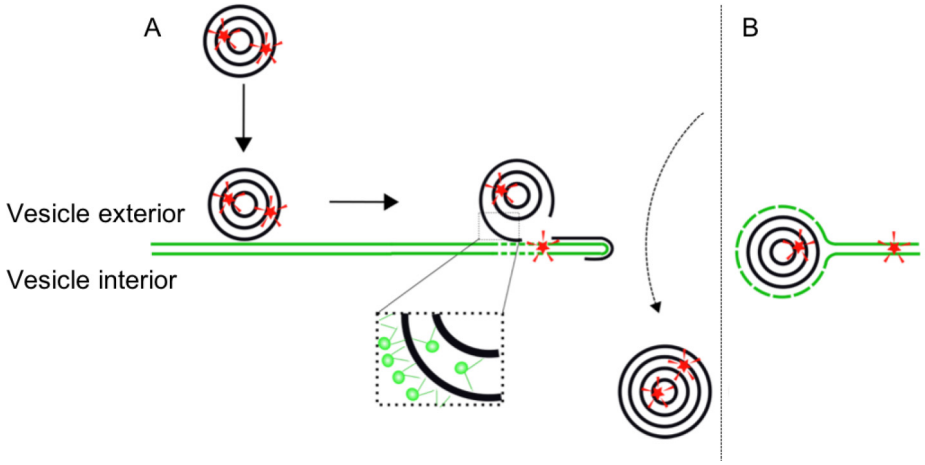

Fig. 4.28. Schematic diagram showing potential pore stabilisation via lipid swelling of particle or a membrane defect.A) The attraction the lipids and the strongly hydrophobic core of the particle structure could result in the uptake of lipid molecules between the polymer layers, effectively swelling the particles. The swelling weakens the intermolecular forces between the polymers, making regions of polymer available to stabilise the pores for later PIL entry to GUV interior (entry of free particle indicated by black dashed arrow, solid arrows depict the stages of the mechanism). B) The defect is generated by a particle disturbing lamellarity of membrane and frustrating the bilayer. The particle may get covered by a lipid monolayer (as shown) or an incomplete bilayer. Other Rh-PIL nanoparticles are able to enter the vesicle interior via these stabilised pores. The dotted green lines in both A) and B) represent a possible frustrated or incomplete bilayer.

The evidence presented in Fig. 4.21, with the polarisation of the DOPC membranes, also contributes to our models for both potential mechanisms of pore stabilisation. As discussed, polarisation can only occur when the transition moment of the dye molecule is aligned with the orientation of the lipids. The unwrapping of the particle structure could result in the release of the dye molecules which then incorporate into the membrane as a result of their lipophilic nature. Alternatively, the incorporation of the frustrated lipids between the outer layer of the particle structure and the main GUV bilayer could create an opening/pathway that the dye molecules could pass through.

From the intensities obtained from the particles at the membrane, we also observed a range of intensity values (particle concentration) within a sample. We have previously commented that this could be due to vesicle to vesicle differences, such as differences in membrane tension or heterogeneous distribution of charged lipid for the case of 10% PG membranes (as observed for different interactions for these membranes in the microfluidic device). Another factor, at least in the case of different membrane intensities, could be the labelling efficiency differences on a particle to particle level. We calculated that each particle has 2.30 ± 2.02 dye molecules per particle; as such, the variation in intensities between individual particles could vary significantly and thus account for vesicle to vesicle intensity differences within a sample. The fluorescently labelled particles were also used to determine the number of particles per area of membrane (Fig. 4.18). As previously described, we saw a dependence on particle density both on particle concentration and membrane composition. As PIL concentration increased, the number of particles per unit area on PC membranes increased. For PILs with negatively charged

membranes, the intensity from the particles was the highest, showing that the particles are more closely packed on negative membranes, most probably due to the increased adhesion energy provided by the electrostatic interaction. When we directly compare 0.001 mM PILs on PC and 10% PG membranes, we see very different intensity and thus particle density values. This could indicate that the particles on the PC membranes are experiencing unwrapping of their structures, effectively increasing their membrane coverage. This could also account for the dye polarization effects that we only observe for neutral membranes as well as slowing down of the diffusion by bound polymers.

Whichever mechanism occurs once the PILs have adhered to the membrane, their presence at the membrane has been shown to affect the diffusion of lipids (Fig. 4.25). The exact mechanism of this slowing of the lipids is not clear but we propose the following mechanism. Each particle could simultaneously bind to many lipids (and slowly diffuse with them), and by doing so create regions of lipids that exhibit hindered diffusion due to the steric hindrance by the particles. This would effectively create barriers throughout the bilayer. A similar phenomenon has been observed for the lipid diffusion in cell membranes.[176] The diffusion of lipids in small compartments had a similar diffusion coefficient to comparable synthetic membranes, but the overall diffusion of the cell membrane was significantly lower. The actin-based membrane skeleton, on which some transmembrane proteins are anchored, created small compartments; the transition of lipids from compartment to compartment was responsible for the overall slowing of the lipids. In our case, the PILs could be creating mobile barriers or platforms. We should also consider the situation of the nanoparticles being engulfed by the membrane in the bleach region. Here, a larger area of membrane would be used up to wrap around the particles, therefore more fluorescent lipids would be photobleached. This would then require a larger number of lipids to diffuse into this region, which would make the fluorescence recover slower.

We next go on to discuss how the behaviour of the PILs particles may be comparable to the action of AMPs and make a comparison with a specific peptide, Gomesin, in order to comment on the applicability of our nanoparticles as a possible alternative to AMPs.

4.4.2 PILs' relevance as antimicrobial agents

Some of the results that we have observed in this Chapter are comparable with the behaviour of the action of antimicrobial peptides (AMPs) on biomembranes. For example, the lytic effect of the AMP Gomesin (Gm) on GUV membranes has been observed,[59] along with the formation of pores in GUVs in the presence of Alamethicin, LL37 or melittin.[81] The mechanisms of action of AMPs can be described using three different models: barrel-stave pore formation, toroidal pore formation and the carpet mechanism. Briefly, these different mechanisms proceed as follows: for barrel-stave pores, the helical peptides accumulate on the membrane surface until a threshold concentration where they insert into the membrane and associate to form a stave-stabilized bundle with a central lumen;[177] for toroidal pores the mechanism is similar except that the peptides associate with the lipid head-groups and as such the pore is lined by both the peptides and the lipid headgroups;[178] the carpet mechanism is a non-pore forming mode of action where the peptides cover the membrane surface until the membrane eventually ruptures or disintegrates.[179] In the context of our experimental observations, for a pore to stay open once it has formed it must be stabilised (as is the role

of the AMPs in the two pore models of action). For this, we have speculated on two possible behaviours of the PILs nanoparticles. One possible mechanism could involve the PILS structure unwrapping upon adhesion to the membrane and the unwrapped polymer stabilises the pores (where the pores are generated to offset the increase in membrane tension following engulfment of the particles). Alternatively, we have discussed the possibility of the PILs on the membrane generating regions of frustrated bilayer. This could then result in the unpeeling of the PILs structure due to a plasticising-type effect, and the polymers stabilise the pores as described previously. The stabilisation of the membrane pores by the polymer would be somewhat comparable to the stabilisation of the AMPs in the toroidal pore mechanism. The PILs could also disrupt the lamellarity of the bilayer as shown in Fig. 4.27 and these regions of membrane defects could result in pore stabilisation. The carpet mechanism of AMP action could also possibly exist for our system as we see an instantaneous decrease in vesicle population upon the addition of particles, and also observe occasional macropore formation (see Fig. 4.17).

When considering the potential uses of these particles, it makes sense to draw comparisons with agents which either behave in a similar way or are already employed for the application of interest. As we have observed a lytic action of these PILs particles, with a pronounced contrast between membrane compositions, which can be considered in the context of bacterial membranes, we have been comparing this action to that of antimicrobial peptides. One important factor to consider is the concentration dependence of these particles. We have found that the PILs produce a biologically relevant interaction when we exceed a monomer concentration of 0.03 mM (for 40% negatively charged membranes). In comparison, the MBC for the antimicrobial peptide Gomesin (Gm) acting on POPC membranes doped with 25% PG is 0.2 μM,[59] two orders of magnitude lower than that of the PILs. This might suggest that the concentration of PILs required to have a significant biological impact is too high and thus cannot compete with such peptides as candidates for antimicrobial agents. However, when one considers that the PIL particles are formed from many repeating monomer units, the effective particle number density is actually several orders of magnitude lower than for Gm. For the critical concentrations of 0.03 mM (PILs) and 0.2 μM (Gm), the number densities are 3.65×10^2 PILs/picoliter and 2.73×10^{11} Gm/picoliter respectively. This implies that many more individual peptides are required to work on the membrane to induce the same response as with the PILs particles.

We have also observed events such as stabilized pores and dye polarization which suggests transfer of material from the PILs to the membrane. Such a phenomenon could be utilized for release of active molecules at a target site, for example localized doses of a drug when the particles bind to a membrane of a specific composition.

4.5 Conclusions and outlook

Here we have observed the permeabilisation and rupture of GUVs by PIL nanoparticles and, for the surviving vesicles, we assessed the changes in membrane properties, such as lipid diffusion. We also measured fluorescently labelled PILs both on the vesicle membranes and at the vesicle interiors. The changes in vesicle population were dependent on PIL concentration, with the number of GUVs decreasing as the particle concentration increased. This result also had a dependency on membrane charge, with negatively charged GUVs being destroyed at a lower concentration. We attributed this behaviour to

an electrostatic component of the particle membrane interactions, as the PILs are positively charged. Microfluidic experiments allowed us to directly observe interactions as the PILs were introduced to the GUVs; we saw different GUV responses to the PILs, such as the exchange of sugars across the membrane, vesicle bursting and the formation of macropores. By fluorescently labelling the PILs with Rhodamine-B, we were able to assess their location both at the membrane and inside the GUVs. For the Rh-PILs on the membrane, we used a calibration curve to calculate the nanoparticle density and also compared this to the charge of the membrane and particle concentration. We used FRAP to look at how lipid diffusion changed in the presence of PILs and observed that the nanoparticles slowed the diffusion of the lipids. For the interactions of the PILs with the membranes, we suggested possible mechanisms to explain the phenomena we observed. The permeabilisation of the vesicle membranes, observed via the loss of phase contrast, could be attributed to pores that form when nanoparticles are engulfed by the membrane, as this would increase the membrane tension (due to a decreased surface area to volume ratio). As for the stabilisation of these pores, we speculated on different behaviours of the PILs, such as the particle structure unwrapping, to account for this. The permeabilisation and rupture of the vesicles shows similarities to the interactions between anti-microbial peptides and biomembranes, and we discuss briefly the different interaction mechanisms that AMPs can have. The slowing of the lipid diffusion by the PILs could possibly be due to the particles creating barriers throughout the membrane, similar to the compartment-like behaviour observed in cellular membranes. We observed polarisation of the Rh-B molecules, which suggests alignment of the dye with the lipids in the membrane. This transfer of material from the interior of the PILs structure to the membrane, together with the permeabilisation of the membrane which could allow other molecules to gain access to the cell interior, potentially lends itself quite well to the use of these particles as a drug delivery system.

There are still certain aspects of this PIL-vesicle system that we do not understand and here we outline some next experiments that could be done and the information that they could provide about the interactions.

To look more closely at the behaviour of the particles on the membrane, we considered employing electron microscopy. This would allow us to directly resolve the PIL particles and also look at how the bilayer behaves when it is in contact with them, such as looking for clusters of particles engulfed by membrane. It could also provide the opportunity of visualising the stable pores that we predict for the exchange of sugars and the PILs' entry to the vesicle interiors. Such methods should also allow us to directly observe any particle structures inside the GUVs. Some preliminary experiments have been performed but the results so far have been inconclusive due to the low GUV concentration.

We could use FRET (fluorescence resonance energy transfer) microscopy to look at the possible incorporation of the polymer with the lipid bilayer. Briefly, this technique works by a transfer of energy between two dye molecules, a donor and an acceptor. The donor fluorophore is excited and if an accepting fluorophore is within a certain distance, the emission from the donor is absorbed. Experimentally, this results in a decrease in the fluorescent signal (detected emission) from the donor and an increase in the fluorescent signal (detected emission) from the acceptor. Incorporation of the polymer with the bilayer would result in an increase in membrane area, and effectively increasing the distance between the donor and acceptor fluorophores. We already implemented one

FRET assay by attempting to measure a change in donor signal in the membrane when the Rh-PILs were added to the sample. However, this approach was inconclusive as we did not have a calibration with known concentrations of the acceptor molecule to compare the changes in intensity values with.

Edge tension measurements could allow us to probe the presence of the PIL (in either a wrapped or unwrapped state) at the pore edge. We initially attempted to take such measurements using the electroporation method of Portet & Dimova,[158] however we found it was not applicable due to the membrane having sub-microscopic pores which the field passes through. Another approach to measure the tension could be using visible light to put the membrane under tension until a pore forms.[180,181] We could also add an external dye after different fixed periods of time to determine the pore stability. A similar approach was used by Fuertes et al. to determine how long pores formed by the α5 fragment from the proapoptotic protein Baxα5 stayed open.[182]

During the synthesis of the PILs nanoparticles, we could also try to covalently attach a dye molecule whose lifetime changes within different environments. This could be a way to explore the possible plasticisation of the outer nanoparticle layers by the lipid molecules; if the behaviour of the dye was different in the presence of purely polymer and in the presence of lipids, this could be detected by a change in the fluorescent lifetime of the molecule. The covalent attachment would be important as we have already observed apparent relocation of the Rhodamine-B from the PILs structure to the lipid bilayer for the current ionic bonding between the dye and the PILs. A related experiment would be to produce particles that are loaded with an active substance, where the delivery of this active substance to the vesicle interior can be measured. This would allow us to characterise the efficiency of the PILs as a drug delivery system.

We could also measure the charge of LUVs and GUVs with the compositions frequently used for the interactions with PILs, DOPC and 10% DOPG. As we observe a marked difference in interactions between these two compositions, such as MBC and density of the PILs on the membranes, we would like to quantify the difference in charge between these two lipid compositions. However, other studies using zeta potential measurements of GUVs discussed the reliability of some measurements due to factors such as the polydispersity of the GUV sample or the membrane charge;[183,184] as such, we should look critically at any data we obtain in this way.

We could also extract further data from the microfluidic experiments by looking at the changes in vesicle volume and the exchange of sugars (via phase contrast loss) over time. This would give us further information of the temporal behaviour of the interactions. Similarly, another experiment that could be expanded upon would be to look at the changes in lipid diffusion for the negatively charged (10% DOPG) membranes.

5 Conclusions and outlook

The work presented in this thesis looks at the interactions between particles of different sizes and chemistries and biomembranes by using the model membrane system of GUVs. We used a predominantly optical microscopy-based approach. The first part dealt with how the membrane behaves in the presence of micron-sized particles and how this behaviour changes when we use particles that have been modified to have one Janus surface. We used electrostatic interactions to modulate the adhesion and wetting of the particle surfaces by the GUVs and deflated the vesicles so that the effect of membrane tension was minimised. We found that the membrane prefers to wet only the attractive portion of the particle; in the case of homogeneous particles, the whole particle surface was wetted when the adhesion energy is sufficiently large. However, internalisation does not always depend on the whole particle surface having an attractive interaction, as Janus particles were partially wetted but sometimes still internalised by the membrane. Decreasing the electrostatic interaction resulted in partially wetted particles that were never internalised by the GUVs. The metallic coating on the Janus particles also provided a means to transport adhered vesicles via manipulating the particles with a magnetic field. Future experiments could involve observing the entire interaction from start to finish by introducing the particles once observation is already underway. One way to do so would be to utilise micropipettes. Not only would this allow us to carefully select the vesicles and particles that we want to examine, we could also directly measure how the membrane tension changes as a function of adhesion angle. Other measurements relating to adhesion angle would be to extract data from further bulk experiments so that we could calculate the adhesion energy for each system. We could also generate statistics on the particle penetration depths into the vesicles.

The second part of the study investigated the interactions of poly(ionic liquid) nanoparticles (PILs) with model lipid membranes. These particles are a relatively new type of particle combining many interesting properties, such as a concentric layer-like conformation and potentially the previously observed antibacterial nature of (poly)ionic liquid brushes. In nanoparticle form, interactions with biomembranes have yet to be investigated. The nanoparticles were positively charged. When the PILs were incubated with GUVs, we observed poration of the membrane. This was initially inferred via a loss of phase contrast and later directly observed using microfluidics. With increasing particle concentration the population of GUVs decreased; this effect was also dependent on the membrane composition, with negatively charged membranes being destroyed at lower PILs concentrations. Using PILs labelled with Rhodamine-B we were able to observe the PILs' locations, which was found to be both on the membrane and at the GUV interior. We also examined the changes in membrane properties, namely morphological appearance and lipid diffusion, after incubation with PILs We drew comparisons between our observations and the behaviour of antimicrobial peptides with model membrane systems. We also suggested and discussed the possible interaction mechanisms between the nanoparticles and the membrane based on our experimental findings. Future experiments could use electron microscopy imaging (such as TEM or SEM) to look at the interactions on a smaller scale by directly resolving the PILs structures (and not rely on fluorescent signal). We could also probe how the particle structures possibly integrate themselves with the membranes by looking at changes in FRET (fluorescence resonance

energy transfer) signal in the presence of the PILs. The present work has implications on biological applications such as drug delivery or controlling cytotoxicity; both for increasing our understanding of the possible parameters that can govern the interactions (as presented in Chapter 3) and also for the potential use of a new class of nanoparticle as an antimicrobial agent (PILs interaction in Chapter 4).

6 References

1. Hussain SM, Hess KL, Gearhart JM, Geiss KT, Schlager JJ. In vitro toxicity of nanoparticles in BRL 3A rat liver cells. In: *Toxicology in Vitro*. Vol 19. Pergamon; 2005:975-983. doi:10.1016/j.tiv.2005.06.034
2. Iavicoli I, Leso V, Bergamaschi A. Toxicological effects of titanium dioxide nanoparticles: A review of in vivo studies. *J Nanomater*. 2012;2012. doi:10.1155/2012/964381
3. Wang L, Hu C, Shao L. The antimicrobial activity of nanoparticles: present situation and prospects for the future. *Int J Nanomedicine*. 2017;12:1227-1249. doi:10.2147/IJN.S121956
4. Nune SK, Gunda P, Thallapally PK, Lin Y-Y, Forrest ML, Berkland CJ. Nanoparticles for biomedical imaging. *Expert Opin Drug Deliv*. 2009;6(11):1175-1194. doi:10.1517/17425240903229031
5. C. Peetla, A. Stine VL. Biophysical interactions with model lipid membranes: applications in drug discovery and drug delivery. *Mol Pharm*. 2009;6(5):1264-1276. doi:10.1021/mp9000662.Biophysical
6. Cole M, Lindeque P, Halsband C, Galloway TS. Microplastics as contaminants in the marine environment: A review. *Mar Pollut Bull*. 2011;62(12):2588-2597. doi:10.1016/j.marpolbul.2011.09.025
7. Mulet X, Boyd BJ, Drummond CJ. Advances in drug delivery and medical imaging using colloidal lyotropic liquid crystalline dispersions. *J Colloid Interface Sci*. 2013. doi:10.1016/j.jcis.2012.10.014
8. Xiong MH, Bao Y, Yang XZ, Zhu YH, Wang J. Delivery of antibiotics with polymeric particles. *Adv Drug Deliv Rev*. 2014. doi:10.1016/j.addr.2014.02.002
9. Debouttière P-J, Roux S, Vocanson F, et al. Design of Gold Nanoparticles for Magnetic Resonance Imaging. *Adv Funct Mater*. 2006. doi:10.1002/adfm.200600242
10. Lai SK, Wang YY, Hanes J. Mucus-penetrating nanoparticles for drug and gene delivery to mucosal tissues. *Adv Drug Deliv Rev*. 2009. doi:10.1016/j.addr.2008.11.002
11. Chopra I, O'Neill AJ, Miller K. The role of mutators in the emergence of antibiotic-resistant bacteria. *Drug Resist Updat*. 2003;6(3):137-145. doi:10.1016/S1368-7646(03)00041-4
12. Rizzo L, Manaia C, Merlin C, et al. Urban wastewater treatment plants as hotspots for antibiotic resistant bacteria and genes spread into the environment: A review. *Sci Total Environ*. 2013;447:345-360. doi:10.1016/j.scitotenv.2013.01.032
13. Khachatourians GG. Agricultural use of antibiotics and the evolution and transfer of anitbiotic-resistant bacteria. *Can Med Assoc J*. 1998;159(9):1129-1136. doi:1998-024
14. Andersson DI. Persistence of antibiotic resistant bacteria. *Curr Opin Microbiol*. 2003;6(5):452-456. doi:10.1016/j.mib.2003.09.001
15. Rai M, Yadav A, Gade A. Silver nanoparticles as a new generation of antimicrobials. *Biotechnol Adv*. 2009;27(1):76-83. doi:10.1016/j.biotechadv.2008.09.002
16. Kim JS, Kuk E, Yu KN, et al. Antimicrobial effects of silver nanoparticles. *Nanomedicine Nanotechnology, Biol Med*. 2007;3(1):95-101. doi:10.1016/j.nano.2006.12.001
17. Ren G, Hu D, Cheng EWC, Vargas-Reus MA, Reip P, Allaker RP. Characterisation of copper oxide nanoparticles for antimicrobial applications. *Int J*

Antimicrob Agents. 2009;33(6):587-590. doi:10.1016/j.ijantimicag.2008.12.004
18. Sondi I, Salopek-Sondi B. Silver nanoparticles as antimicrobial agent: A case study on E. coli as a model for Gram-negative bacteria. *J Colloid Interface Sci*. 2004;275(1):177-182. doi:10.1016/j.jcis.2004.02.012
19. Khan JA, Pillai B, Das TK, Singh Y, Maiti S. Molecular effects of uptake of gold nanoparticles in HeLa cells. *ChemBioChem*. 2007;8(11):1237-1240. doi:10.1002/cbic.200700165
20. Chithrani BD, Ghazani AA, Chan WCW. Determing the Size and Shape Dependence of Gold Nanoparticles Uptake Into Mammalian Cells. *Nano Lett*. 2006;6(4):662-668. doi:10.1021/nl052396o
21. Chithrani BD, Chan WCW. Elucidating the mechanism of cellular uptake and removal of protein-coated gold nanoparticles of different sizes and shapes. *Nano Lett*. 2007;7(6):1542-1550. doi:10.1021/nl070363y
22. Li W, Chen C, Ye C, et al. The translocation of fullerenic nanoparticles into lysosome via the pathway of clathrin-mediated endocytosis. *Nanotechnology*. 2008;19(14). doi:10.1088/0957-4484/19/14/145102
23. Goya GF, Marcos-Campos I, Fernández-Pacheco R, et al. Dendritic cell uptake of iron-based magnetic nanoparticles. *Cell Biol Int*. 2008;32(8). doi:10.1016/j.cellbi.2008.04.001
24. Pradhan P, Giri J, Banerjee R, Bellare J, Bahadur D. Preparation and characterization of manganese ferrite-based magnetic liposomes for hyperthermia treatment of cancer. *J Magn Magn Mater*. 2007;311(1 SPEC. ISS.):208-215. doi:10.1016/j.jmmm.2006.10.1179
25. Ma YJ, Gu HC. Study on the endocytosis and the internalization mechanism of aminosilane-coated Fe3O4nanoparticles in vitro. In: *Journal of Materials Science: Materials in Medicine*. Vol 18. ; 2007:2145-2149. doi:10.1007/s10856-007-3015-8
26. Chithrani BD, Ghazani AA, Chan WCW. Determining the size and shape dependence of gold nanoparticle uptake into mammalian cells. *Nano Lett*. 2006;6(4):662-668. doi:10.1021/nl052396o
27. Nel AE, Mädler L, Velegol D, et al. Understanding biophysicochemical interactions at the nano–bio interface. *Nat Mater www.nature.com/naturematerials*. 2009;8. doi:10.1038/nmat2442
28. Cho EC, Xie J, Wurm PA, Xia Y. Understanding the Role of Surface Charges in Cellular Adsorption versus Internalization by Selectively Removing Gold Nanoparticles on the Cell Surface with a I 2 / KI Etchant 2009. *Nano Lett*. 2009;9(3):1080-1084. doi:10.1021/nl803487r
29. Xie J, Xu C, Kohler N, Hou Y, Sun S. Controlled PEGylation of monodisperse Fe3O4 nanoparticles for reduced non-specific uptake by macrophage cells. *Adv Mater*. 2007;19(20):3163-3166. doi:10.1002/adma.200701975
30. Chang E, Yu WW, Colvin VL, Drezek R. Quantifying the Influence of Surface Coatings on Quantum Dot Uptake in Cells. *J Biomed Nanotechnol*. 2005;1(4):397-401. doi:10.1166/jbn.2005.053
31. Cooper GM, Hausman RE. *The Cell: A Molecular Approach 2nd Edition*.; 2007. doi:NBK9839
32. Lodish H, Berk A, Zipursky S. Molecular Cell Biology. 4th edition. Section 11.1, Transcription Termination.
33. Yeagle PL. Lipid – Protein Interactions in Membranes. In: *The Membranes of Cells*. Academic Press; 2016:291-334. doi:10.1016/B978-0-12-800047-2.00012-7
34. Sohlenkamp C, Geiger O. Bacterial membrane lipids: Diversity in structures and pathways. *FEMS Microbiol Rev*. 2015;40(1):133-159. doi:10.1093/femsre/fuv008

35. Yeung T, Gilbert GE, Shi J, Silvius J, Kapus A, Grinstein S. Membrane phosphatidylserine regulates surface charge and protein localization. *Science (80-)*. 2008;319(5860):210-213. doi:10.1126/science.1152066
36. Jane Reece, Urry LA, Cain ML, et al. *Campbell Biology: Global Edition*.; 2011. http://view.ebookplus.pearsoncmg.com/ebook/launcheText.do?values=bookID::5799::platform::1004::fromloginpage::N::invokeType::lms::launchState::goToEBook::platform::1004::globalBookID::CM12301699::userID::13814279::scenario::3::scenarioid::scenario3::cours.
37. Spooner MJ, Gale PA. Anion transport across varying lipid membranes - The effect of lipophilicity. *Chem Commun*. 2015;51(23):4883-4886. doi:10.1039/c5cc00823a
38. Israelachvili J. *Intermolecular and Surface Forces*.; 2011. doi:10.1016/C2009-0-21560-1
39. Smith R, Tanford C. The critical micelle concentration of l-α-dipalmitoylphosphatidylcholine in water and water/methanol solutions. *J Mol Biol*. 1972;67(1):75-83. doi:10.1016/0022-2836(72)90387-7
40. Jouhet J. Importance of the hexagonal lipid phase in biological membrane organization. *Front Plant Sci*. 2013;4:494. doi:10.3389/fpls.2013.00494
41. Singer SJ, Nicholson GL. The fluid mosaic model of the structure of cell membranes. *Science (80-)*. 1972;175(4023):720-731.
42. Lladó V, López DJ, Ibarguren M, et al. Regulation of the cancer cell membrane lipid composition by NaCHOleate: Effects on cell signaling and therapeutical relevance in glioma. *Biochim Biophys Acta - Biomembr*. 2014;1838(6):1619-1627. doi:10.1016/j.bbamem.2014.01.027
43. Vertegel AA, Siegel RW, Dordick JS. Silica Nanoparticle Size Influences the Structure and Enzymatic Activity of Adsorbed Lysozyme. *Langmuir*. 2004;20(16):6800-6807. doi:10.1021/la0497200
44. Oberdörster G, Maynard A, Donaldson K, et al. Principles for characterizing the potential human health effects from exposure to nanomaterials: elements of a screening strategy. *Part Fibre Toxicol*. 2005;2(1):8. doi:10.1186/1743-8977-2-8
45. Gratton SEA, Ropp PA, Pohlhaus PD, et al. The effect of particle design on cellular internalization pathways. *Proc Natl Acad Sci*. 2008;105(33). http://www.pnas.org/content/105/33/11613.short. Accessed July 26, 2018.
46. Karlsson HL, Cronholm P, Hedberg Y, et al. Cell membrane damage and protein interaction induced by copper containing nanoparticles-Importance of the metal release process. *Toxicology*. 2013;313(1):59-69. doi:10.1016/j.tox.2013.07.012
47. Kim JA, Aberg C, Salvati A, Dawson KA. Role of cell cycle on the cellular uptake and dilution of nanoparticles in a cell population. *Nat Nanotechnol*. 2012;7(1):62-68. doi:10.1038/nnano.2011.191
48. Dietrich C, Angelova M, Pouligny B. Adhesion of Latex Spheres to Giant Phospholipid Vesicles: Statics and Dynamics. *J Phys II*. 1997;7(11):1651-1682. doi:10.1051/jp2:1997208
49. Natsume Y, Pravaz O, Yoshida H, Imai M. Shape deformation of giant vesicles encapsulating charged colloidal particles. *Soft Matter*. 2010;6(21):5359. doi:10.1039/c0sm00396d
50. Mihut AM, Dabkowska AP, Crassous JJ, Schurtenberger P, Nylander T. Tunable adsorption of soft colloids on model biomembranes. *ACS Nano*. 2013;7(12):10752-10763. doi:10.1021/nn403892f
51. van der Wel C, Heinrich D, Kraft DJ. Microparticle Assembly Pathways on Lipid Membranes. *Biophys J*. 2017;113(5):1037-1046. doi:10.1016/j.bpj.2017.07.019

52. van der Wel C, Vahid A, Šarić A, et al. Lipid membrane-mediated attraction between curvature inducing objects. *Sci Rep*. 2016;6:32825. doi:10.1038/srep32825
53. Li S, Malmstadt N. Deformation and poration of lipid bilayer membranes by cationic nanoparticles. *Soft Matter*. 2013;9(20):4969. doi:10.1039/c3sm27578g
54. Kettiger H, Québatte G, Perrone B, Huwyler J. Interactions between silica nanoparticles and phospholipid membranes. *Biochim Biophys Acta - Biomembr*. 2016;1858(9):2163-2170. doi:10.1016/j.bbamem.2016.06.023
55. Engel MFM, Khemtémourian L, Kleijer CC, et al. Membrane damage by human islet amyloid polypeptide through fibril growth at the membrane. *Proc Natl Acad Sci U S A*. 2008;105(16):6033-6038. doi:10.1073/pnas.0708354105
56. Altamura E, Stano P, Walde P, Mavelli F. Giant vesicles as micro-sized enzymatic reactors: Perspectives and recent experimental advancements. *Int J Unconv Comput*. 2015;11(1):5-21.
57. Jesorka A, Orwar O. Liposomes: Technologies and Analytical Applications. *Annu Rev Anal Chem*. 2008. doi:10.1146/annurev.anchem.1.031207.112747
58. Dimova R. Giant Vesicles. A Biomimetic Tool for Membrane Characterization. *Adv Planar Lipid Bilayers Liposomes*. 2012. doi:10.1016/B978-0-12-396534-9.00001-5
59. Domingues TM, Riske KA, Miranda A. Revealing the lytic mechanism of the antimicrobial peptide gomesin by observing giant unilamellar vesicles. *Langmuir*. 2010;26(13):11077-11084. doi:10.1021/la100662a
60. Lens M. Use of fullerenes in cosmetics. *Recent Patents Biotechnol*. 2009. doi:10.2174/187220809788700166
61. Tournihac F, Simon P. Cosmetic or dermatological topical compositions comprising dendritic polyesters. 2001.
62. Sakamoto J, Annapragada A, Decuzzi P, Ferrari M. Antibiological barrier nanovector technology for cancer applications. *Expert Opin Drug Deliv*. 2007. doi:10.1517/17425247.4.4.359
63. Van Broekhuizen P, Van Broekhuizen F, Cornelissen R, Reijnders L. Use of nanomaterials in the European construction industry and some occupational health aspects thereof. *J Nanoparticle Res*. 2011. doi:10.1007/s11051-010-0195-9
64. Haveli SD, Walter P, Patriarche G, et al. Hair fiber as a nanoreactor in controlled synthesis of fluorescent gold nanoparticles. *Nano Lett*. 2012. doi:10.1021/nl303107w
65. Björnmalm M, Yan Y, Caruso F. Engineering and evaluating drug delivery particles in microfluidic devices. *J Control Release*. 2014;190:139-149. doi:10.1016/j.jconrel.2014.04.030
66. Barbé C, Bartlett J, Kong L, et al. Silica particles: A novel drug-delivery system. *Adv Mater*. 2004. doi:10.1002/adma.200400771
67. Ito A, Shinkai M, Honda H, Kobayashi T. Medical application of functionalized magnetic nanoparticles. *J Biosci Bioeng*. 2005. doi:10.1263/jbb.100.1
68. Song D, Forciniti D. Effects of cosolvents and pH on protein adsorption on polystyrene latex: A dynamic light scattering study. *J Colloid Interface Sci*. 2000;221(1):25-37. doi:10.1006/jcis.1999.6560
69. Fair B., Jamieson a. . Studies of protein adsorption on polystyrene latex surfaces. *J Colloid Interface Sci*. 1980;77(2):525-534. doi:10.1016/0021-9797(80)90325-2
70. Browne MM, Lubarsky G V., Davidson MR, Bradley RH. Protein adsorption onto polystyrene surfaces studied by XPS and AFM. *Surf Sci*. 2004;553(1-3):155-167. doi:10.1016/j.susc.2004.01.046

71. Sahil K, Akanksha M, Premjeet S, Bilandi A, Kapoor B. Microsphere: a review. *Int J Res Pharm Chem*. 2011;1(4):1184-1198. http://www.ijrpc.com/files/000055.pdf.
72. Saralidze K, Knetsch MLW, van Hooy-Corstjens CSJ, Koole LH. Radio-opaque and surface-functionalized polymer microparticles: Potentially safer biomaterials for different injection therapies. *Biomacromolecules*. 2006;7(11):2991-2996. doi:10.1021/bm0603903
73. Li N, Sharifi-Mood N, Tu F, et al. Curvature-Driven Migration of Colloids on Tense Lipid Bilayers. *Langmuir*. 2017;33(2):600-610. doi:10.1021/acs.langmuir.6b03406
74. Sarfati R, Dufresne ER. Long-range attraction of particles adhered to lipid vesicles. *Phys Rev E*. 2016;94(1):1-7. doi:10.1103/PhysRevE.94.012604
75. Walther A, Müller AHE. Janus particles. *Soft Matter*. 2008;4(4):663-668. doi:10.1039/b718131k
76. Yuan J, Antonietti M. Poly(ionic liquid) latexes prepared by dispersion polymerization of ionic liquid monomers. *Macromolecules*. 2011;44(4):744-750. doi:10.1021/ma102858b
77. Yuan J, Soll S, Drechsler M, Müller AHE, Antonietti M. Self-assembly of poly(ionic liquid)s: Polymerization, mesostructure formation, and directional alignment in one step. *J Am Chem Soc*. 2011;133(44):17556-17559. doi:10.1021/ja207080j
78. Men Y, Kuzmicz D, Yuan J. Poly(ionic liquid) colloidal particles. *Curr Opin Colloid Interface Sci*. 2014;19(2):76-83. doi:10.1016/j.cocis.2014.03.012
79. Carson L, Chau PKW, Earle MJ, et al. Antibiofilm activities of 1-alkyl-3-methylimidazolium chloride ionic liquids. *Green Chem*. 2009;11(4):492. doi:10.1039/b821842k
80. Docherty KM, Kulpa, Jr. CF. Toxicity and antimicrobial activity of imidazolium and pyridinium ionic liquids. *Green Chem*. 2005;7(4):185. doi:10.1039/b419172b
81. Faust JE, Yang PY, Huang HW. Action of Antimicrobial Peptides on Bacterial and Lipid Membranes: A Direct Comparison. *Biophys J*. 2017;112(8):1663-1672. doi:10.1016/j.bpj.2017.03.003
82. Chen Y-F, Sun T-L, Sun Y, Huang HW. Interaction of Daptomycin with Lipid Bilayers: A Lipid Extracting Effect. *Biochemistry*. 2014;53(33):5384-5392. doi:10.1021/bi500779g
83. Zhang S, Nelson A, Beales PA. Freezing or Wrapping: The Role of Particle Size in the Mechanism of Nanoparticle–Biomembrane Interaction. *Langmuir*. 2012;28(35):12831-12837. doi:10.1021/la301771b
84. Agudo-Canalejo J, Lipowsky R. Critical particle sizes for the engulfment of nanoparticles by membranes and vesicles with bilayer asymmetry. *ACS Nano*. 2015;9(4):3704-3720. doi:10.1021/acsnano.5b01285
85. Deserno M, Bickel T. Wrapping of a spherical colloid by a fluid membrane. *Europhys Lett*. 2003;62(5):767-773. doi:10.1209/epl/i2003-00438-4
86. Raatz M, Lipowsky R, Weikl TR. Cooperative wrapping of nanoparticles by membrane tubes. *Soft Matter*. 2014;10(20):3570-3577. doi:10.1039/c3sm52498a
87. Sahay G, Alakhova DY, Kabanov A V. Endocytosis of nanomedicines. *J Control Release*. 2010. doi:10.1016/j.jconrel.2010.01.036
88. Mukherjee S, Ghosh RN, Maxfield FR. Endocytosis. *Physiol Rev*. 1997.
89. Seifert U. Configurations of fluid membranes and vesicles. *Adv Phys*. 1997;46(1):13-137. doi:10.1080/00018739700101488
90. Helfrich W. Elastic Properties of Lipid Bilayers: Theory and Possible Experiments.

Zeitschrift fur Naturforsch - Sect C J Biosci. 1973;28(11-12):693-703. doi:10.1515/znc-1973-11-1209

91. Dimova R, Aranda S, Bezlyepkina N, Nikolov V, Riske KA, Lipowsky R. A practical guide to giant vesicles. Probing the membrane nanoregime via optical microscopy. *J Phys Condens Matter*. 2006;18:1151-1176. doi:10.1088/0953-8984/18/28/S04
92. Lipowsky R, Leibler S. Unbinding Transitions of Interacting Membranes. *Phys Rev Lett*. 1986;56(23):2541-2544. doi:10.1103/PhysRevLett.56.2541
93. Seifert U, Lipowsky R. Adhesion of vesicles. *Phys Rev A*. 1990;42(8):4768-4771. doi:10.1103/PhysRevA.42.4768
94. Capovilla R. Elastic bending energy: A variational approach. *J Geom Symmetry Phys*. 2017;45:1-45. doi:10.7546/jgsp-45-2017-1-45
95. Agudo-Canalejo J, Lipowsky R. Uniform and Janus-like nanoparticles in contact with vesicles: energy landscapes and curvature-induced forces. *Soft Matter*. 2017;13(11):2155-2173. doi:10.1039/C6SM02796B
96. Ungewickell EJ, Hinrichsen L. Endocytosis: clathrin-mediated membrane budding. *Curr Opin Cell Biol*. 2007;19(4):417-425. doi:10.1016/j.ceb.2007.05.003
97. Angelova MI, Dimitrov DS. Liposome Electro formation. *Faraday Discuss Chem SOC*. 1986;81(0):303-311. doi:10.1039/dc9868100303
98. Weinberger A, Tsai F-C, Koenderink GH, et al. Gel-assisted formation of giant unilamellar vesicles. *Biophys J*. 2013;105(1):154-164. doi:10.1016/j.bpj.2013.05.024
99. Lira RB, Steinkühler J, Knorr RL, Dimova R, Riske KA. Posing for a picture: vesicle immobilization in agarose gel. *Sci Rep*. 2016;6(April):25254. doi:10.1038/srep25254
100. Stein H, Spindler S, Bonakdar N, Wang C, Sandoghdar V. Production of isolated giant unilamellar vesicles under high salt concentrations. *Front Physiol*. 2017;8(FEB):63. doi:10.3389/fphys.2017.00063
101. Bagatolli LA, Parasassi T, Gratton E. Giant phospholipid vesicles: Comparison among the whole lipid sample characteristics using different preparation methods - A two photon fluorescence microscopy study. *Chem Phys Lipids*. 2000;105(2):135-147. doi:10.1016/S0009-3084(00)00118-3
102. Traïkia M, Warschawski DE, Recouvreur M, Cartaud J, Devaux PF. Formation of unilamellar vesicles by repetitive freeze-thaw cycles: Characterization by electron microscopy and 31P-nuclear magnetic resonance. *Eur Biophys J*. 2000;29(3):184-195. doi:10.1007/s002490000077
103. Ruzin SE. Plant Microtechnique and Microscopy: Special Methods. In: *Plant Microtechnique and Microscopy*. Oxford University Press; 1951:127-128. doi:10.2307/1224595
104. Ishikawa-Ankerhold HC, Ankerhold R, Drummen GPC. Advanced Fluorescence Microscopy Techniques—FRAP, FLIP, FLAP, FRET and FLIM. *Molecules*. 2012;17(4):4047-4132. doi:10.3390/molecules17044047
105. Olympus. Confocal Microscope Scanning Systems. *Olympus Lifescience website*. 2015;2:1-7. https://www.olympus-lifescience.com/en/microscope-resource/primer/techniques/confocal/confocalscanningsystems/. Accessed June 29, 2018.
106. Conchello JA, Lichtman JW. Optical sectioning microscopy. *Nat Methods*. 2005;2(12):920-931. doi:10.1038/nmeth815
107. De Chaumont F, Dallongeville S, Chenouard N, et al. Icy: An open bioimage informatics platform for extended reproducible research. *Nat Methods*.

2012;9(7):690-696. doi:10.1038/nmeth.2075
108. Li S, Malmstadt N. Deformation and poration of lipid bilayer membranes by cationic nanoparticles. *Soft Matter*. 2013;9(20):4969-4976. doi:10.1039/c3sm27578g
109. Agudo-Canalejo J, Lipowsky R. Uniform and Janus-like nanoparticles in contact with vesicles: energy landscapes and curvature-induced forces. *Soft Matter*. 2017;13(11):2155-2173. doi:10.1039/C6SM02796B
110. Bharti B, Rutkowski D, Han K, Kumar AU, Hall CK, Velev OD. Capillary Bridging as a Tool for Assembling Discrete Clusters of Patchy Particles. *J Am Chem Soc*. 2016;138(45):14948-14953. doi:10.1021/jacs.6b08017
111. Prevo BG, Velev OD. Controlled, Rapid Deposition of Structured Coatings from Micro- and Nanoparticle Suspensions. *Langmuir*. 2004;20(6):2099-2107. doi:10.1021/la035295j
112. Ling XY, Phang IY, Acikgoz C, et al. Janus particles with controllable patchiness and their chemical functionalization and supramolecular assembly. *Angew Chemie - Int Ed*. 2009;48(41):7677-7682. doi:10.1002/anie.200903579
113. Wang B, Li B, Zhao B, Li CY. Amphiphilic Janus gold nanoparticles via combining “solid-state grafting-to” and “grafting-from” methods. *J Am Chem Soc*. 2008;130(35):11594-11595. doi:10.1021/ja804192e
114. Wang H, Brandl DW, Le F, Nordlander P, Halas NJ. Nanorice: A hybrid plasmonic nanostructure. *Nano Lett*. 2006;6(4):827-832. doi:10.1021/nl060209w
115. Koo HY, Yi DK, Yoo SJ, Kim DY. A snowman-like array of colloidal dimers for antireflecting surfaces. *Adv Mater*. 2004;16(3):274-277. doi:10.1002/adma.200305617
116. Nie Z, Li W, Seo M, Xu S, Kumacheva E. Janus and ternary particles generated by microfluidic synthesis: Design, synthesis, and self-assembly. *J Am Chem Soc*. 2006;128(29):9408-9412. doi:10.1021/ja060882n
117. Subramaniam AB, Abkarian M, Mahadevan L, Stone HA. Colloid science: Non-spherical bubbles. *Nature*. 2005;438(7070):930. doi:10.1038/438930a
118. Hu SH, Gao X. Nanocomposites with spatially separated functionalities for combined imaging and magnetolytic therapy. *J Am Chem Soc*. 2010;132(21):7234-7237. doi:10.1021/ja102489q
119. Loget G, Kuhn A. Bulk synthesis of Janus objects and asymmetric patchy particles. *J Mater Chem*. 2012;22(31):15457-15474. doi:10.1039/c2jm31740k
120. Smoukov SK, Gangwal S, Marquez M, Velev OD. Reconfigurable responsive structures assembled from magnetic Janus particles. *Soft Matter*. 2009;5(6):1285-1292. doi:10.1039/b814304h
121. Thévenaz P, Ruttimann UE, Unser M. A pyramid approach to subpixel registration based on intensity. *IEEE Trans Image Process*. 1998;7(1):27-41. doi:10.1109/83.650848
122. Ghosh S, Puri IK. Soft polymer magnetic nanocomposites: Microstructure patterning by magnetophoretic transport and self-assembly. *Soft Matter*. 2013;9(6):2024-2029. doi:10.1039/c2sm27420e
123. Goldstein JL, Anderson RGW, Brown MS. Coated pits,coated vesicles,and receptor-mediated endocytosis. *Nature*. 1979;279(5715):679-685. doi:10.1038/279679a0
124. Noppl-Simson DA, Needham D. Avidin-biotin interactions at vesicle surfaces: Adsorption and binding, cross-bridge formation, and lateral interactions. *Biophys J*. 1996;70(3):1391-1401. doi:10.1016/S0006-3495(96)79697-2
125. Fröhlich E. The role of surface charge in cellular uptake and cytotoxicity of

medical nanoparticles. *Int J Nanomedicine*. 2012;7:5577-5591. doi:10.2147/IJN.S36111
126. Bezlyepkina N, Gracià RS, Shchelokovskyy P, Lipowsky R, Dimova R. Phase diagram and tie-line determination for the ternary mixture DOPC/eSM/Cholesterol. *Biophys J*. 2013;104(7):1456-1464. doi:10.1016/j.bpj.2013.02.024
127. Lipowsky R, Döbereiner HG. Vesicles in contact with nanoparticles and colloids. *Europhys Lett*. 1998;43(2):219-225. doi:10.1209/epl/i1998-00343-4
128. Bhatia T, Agudo-Canalejo J, Dimova R, Lipowsky R. Membrane Nanotubes Increase the Robustness of Giant Vesicles. *ACS Nano*. 2018;12(5):4478-4485. doi:10.1021/acsnano.8b00640
129. Jiang J, Gu H, Shao H, Devlin E, Papaefthymiou GC, Ying JY. Bifunctional Fe3O4-Ag heterodimer nanoparticles for two-photon fluorescence imaging and magnetic manipulation. *Adv Mater*. 2008;20(23):4403-4407. doi:10.1002/adma.200800498
130. Lee SM, Kim HJ, Ha YJ, et al. Targeted chemo-photothermal treatments of rheumatoid arthritis using gold half-shell multifunctional nanoparticles. *ACS Nano*. 2013;7(1):50-57. doi:10.1021/nn301215q
131. Moghadam BY, Hou WC, Corredor C, Westerhoff P, Posner JD. Role of nanoparticle surface functionality in the disruption of model cell membranes. *Langmuir*. 2012;28(47):16318-16326. doi:10.1021/la302654s
132. Van Der Wel C, Bossert N, Mank QJ, Winter MGT, Heinrich D, Kraft DJ. Surfactant-free Colloidal Particles with Specific Binding Affinity. *Langmuir*. 2017;33(38). doi:10.1021/acs.langmuir.7b02065
133. Hetemi D, Pinson J. Surface functionalisation of polymers. *Chem Soc Rev*. 2017;46(19):5701-5713. doi:10.1039/c7cs00150a
134. Rogers RD, Seddon KR. Ionic Liquids--Solvents of the Future? *Science (80-)*. 2003;302(5646). http://science.sciencemag.org/content/302/5646/792. Accessed August 8, 2018.
135. Alberto EE, Rossato LL, Alves SH, Alves D, Braga AL. Imidazolium ionic liquids containing selenium: synthesis and antimicrobial activity. *Org Biomol Chem*. 2011;9(4):1001-1003. doi:10.1039/C0OB01010C
136. Ye Q, Gao T, Wan F, et al. Grafting poly(ionic liquid) brushes for anti-bacterial and anti-biofouling applications. *J Mater Chem*. 2012;22(26):13123. doi:10.1039/c2jm31527k
137. Chen YF, Sun TL, Sun Y, Huang HW. Interaction of daptomycin with lipid bilayers: A lipid extracting effect. *Biochemistry*. 2014;53(33):5384-5392. doi:10.1021/bi500779g
138. Dathe M, Nikolenko H, Meyer J, Beyermann M, Bienert M. Optimization of the antimicrobial activity of magainin peptides by modification of charge. *FEBS Lett*. 2001. doi:10.1016/S0014-5793(01)02648-5
139. Glukhov E, Stark M, Burrows LL, Deber CM. Basis for selectivity of cationic antimicrobial peptides for bacterial versus mammalian membranes. *J Biol Chem*. 2005. doi:10.1074/jbc.M507042200
140. Manzini MC, Perez KR, Riske KA, et al. Peptide:lipid ratio and membrane surface charge determine the mechanism of action of the antimicrobial peptide BP100. Conformational and functional studies. *Biochim Biophys Acta - Biomembr*. 2014;1838(7):1985-1999. doi:10.1016/j.bbamem.2014.04.004
141. Tamba Y, Ohba S, Kubota M, Yoshioka H, Yoshioka H, Yamazaki M. Single GUV method reveals interaction of tea catechin (2)-epigallocatechin gallate with lipid membranes. *Biophys J*. 2007;92(9):3178-3194.

doi:10.1529/biophysj.106.097105
142. Steinkühler J, De Tillieux P, Knorr RL, Lipowsky R, Dimova R. Charged giant unilamellar vesicles prepared by electroformation exhibit nanotubes and transbilayer lipid asymmetry. *Sci Rep*. 2018;8(1):11838. doi:10.1038/s41598-018-30286-z
143. Ewins E, Lira RB, Zhang W, et al. Poly(Ionic Liquid) Nanoparticles Selectively Disrupt Biomembranes. *Adv Sci*. December 2018:1801602. doi:10.1002/advs.201801602
144. Instruments M. Zeta potential: An Introduction in 30 minutes. *Zetasizer Nano Serles Tech Note MRK654-01*. 2011;2:1-6. doi:10.1017/CBO9781107415324.004
145. Deschamps J, Kantsler V, Segre E, Steinberg V. Dynamics of a vesicle in general flow. *Proc Natl Acad Sci U S A*. 2009;106(28):11444-11447. doi:10.1073/pnas.0902657106
146. Li S, Hu PC, Malmstadt N. Imaging molecular transport across lipid bilayers. *Biophys J*. 2011;101(3):700-708. doi:10.1016/j.bpj.2011.06.044
147. Robinson T, Kuhn P, Eyer K, Dittrich PS. Microfluidic trapping of giant unilamellar vesicles to study transport through a membrane pore. *Biomicrofluidics*. 2013;7(4):44105. doi:10.1063/1.4816712
148. Silva-López EI, Edens LE, Barden AO, Keller DJ, Brozik JA. Conditions for liposome adsorption and bilayer formation on BSA passivated solid supports. *Chem Phys Lipids*. 2014;183:91-99. doi:10.1016/j.chemphyslip.2014.06.002
149. Day CA, Kenworthy AK. Tracking microdomain dynamics in cell membranes. *Biochim Biophys Acta - Biomembr*. 2009;1788(1):245-253. doi:10.1016/j.bbamem.2008.10.024
150. Kang M, Day CA, Kenworthy AK, DiBenedetto E. Simplified equation to extract diffusion coefficients from confocal FRAP data. *Traffic*. 2012;13(12):1589-1600. doi:10.1111/tra.12008
151. Miyawaki A. Proteins on the move: Insights gained from fluorescent protein technologies. *Nat Rev Mol Cell Biol*. 2011;12(10):656-668. doi:10.1038/nrm3199
152. Soumpasis DM. Theoretical analysis of fluorescence photobleaching recovery experiments. *Biophys J*. 1983;41(1):95-97. doi:10.1016/S0006-3495(83)84410-5
153. Axelrod D, Koppel DE, Schlessinger J, Elson E, Webb WW. Mobility measurement by analysis of fluorescence photobleaching recovery kinetics. *Biophys J*. 1976;16(9):1055-1069. doi:10.1016/S0006-3495(76)85755-4
154. Kang M, Day CA, Drake K, Kenworthy AK, DiBenedetto E. A Generalization of Theory for Two-Dimensional Fluorescence Recovery after Photobleaching Applicable to Confocal Laser Scanning Microscopes. *Biophys J*. 2009;97(5):1501-1511. doi:10.1016/j.bpj.2009.06.017
155. Schröder J. Fluorescence Recovery after Photobleaching (FRAP) and its Offspring. 2011;(Figure 1):1-5. https://www.leica-microsystems.com/science-lab/fluorescence-recovery-after-photobleaching-frap-and-its-offspring/. Accessed July 6, 2018.
156. Som A, Tew GN. Influence of lipid composition on membrane activity of antimicrobial phenylene ethynylene oligomers. *J Phys Chem B*. 2008;112(11):3495-3502. doi:10.1021/jp077487j
157. Riske KA, Dimova R. Electro-deformation and poration of giant vesicles viewed with high temporal resolution. *Biophys J*. 2005;88(2):1143-1155. doi:10.1529/biophysj.104.050310
158. Portet T, Dimova R. A new method for measuring edge tensions and stability of lipid bilayers: Effect of membrane composition. *Biophys J*. 2010;99(10):3264-

3273. doi:10.1016/j.bpj.2010.09.032
159. Islam MZ, Alam JM, Tamba Y, Karal MAS, Yamazaki M. The single GUV method for revealing the functions of antimicrobial, pore-forming toxin, and cell-penetrating peptides or proteins. *Phys Chem Chem Phys*. 2014;16(30):15752-15767. doi:10.1039/C4CP00717D
160. Fázio MA, Oliveira VX, Bulet P, Miranda MTM, Daffre S, Miranda A. Structure-activity relationship studies of gomesin: Importance of the disulfide bridges for conformation, bioactivities, and serum stability. *Biopolym - Pept Sci Sect*. 2006;84(2):205-218. doi:10.1002/bip.20396
161. Jucker BA, Harms H, Zehnder AJB. Adhesion of the positively charged bacterium Stenotrophomonas (Xanthomonas) maltophilia 70401 to glass and teflon. *J Bacteriol*. 1996. doi:10.1128/jb.178.18.5472-5479.1996
162. Czogalla A, Grzybek M, Jones W, Coskun Ü. Validity and applicability of membrane model systems for studying interactions of peripheral membrane proteins with lipids. *Biochim Biophys Acta - Mol Cell Biol Lipids*. 2014;1841(8):1049-1059. doi:10.1016/j.bbalip.2013.12.012
163. Steinkühler J, De Tillieux P, Knorr RL, Lipowsky R, Dimova R. No Title. *Sci Rep*. 2018;In revisio.
164. Rawicz W, Olbrich KC, McIntosh T, Needham D, Evans E. Effect of Chain Length and Unsaturation on Elasticity of Lipid Bilayers. *Biophys J*. 2000;79(1):328-339. doi:10.1016/S0006-3495(00)76295-3
165. Tristram-Nagle S, Petrache HI, Nagle JF. Structure and interactions of fully hydrated dioleoylphosphatidylcholine bilayers. *Biophys J*. 1998;75(2):917-925. doi:10.1016/S0006-3495(98)77580-0
166. Bagatolli LA. To see or not to see: Lateral organization of biological membranes and fluorescence microscopy. *Biochim Biophys Acta - Biomembr*. 2006;1758(10):1541-1556. doi:10.1016/j.bbamem.2006.05.019
167. Valeur B, Berberan-Santos MN. *Molecular Fluorescence : Principles and Applications*. Wiley-VCH; 2013. https://books.google.de/books?hl=en&lr=&id=NdySsFt8TN8C&oi=fnd&pg=PR15&dq=%22physical+basis%22+beer+lambert+law&ots=yTXiZvZ2N1&sig=OUqqLAcoJhJ1rIjwjF725Dtu1_E#v=onepage&q=%22physical basis%22 beer lambert law&f=false. Accessed May 3, 2018.
168. Vult Von Steyern F, Josefsson JO, Tågerud S. Rhodamine B, a fluorescent probe for acidic organelles in denervated skeletal muscle. *J Histochem Cytochem*. 1996;44(3):267-274. doi:10.1177/44.3.8648087
169. Bahrami AH, Lipowsky R, Weikl TR. Tubulation and aggregation of spherical nanoparticles adsorbed on vesicles. *Phys Rev Lett*. 2012;109(18):188102. doi:10.1103/PhysRevLett.109.188102
170. Lee C-C, Sun Y, Qian S, Huang HW. Transmembrane Pores Formed by Human Antimicrobial Peptide LL-37. *Biophys J*. 2011;100(7):1688-1696. doi:10.1016/j.bpj.2011.02.018
171. Riske KA. Optical Microscopy of Giant Vesicles as a Tool to Reveal the Mechanism of Action of Antimicrobial Peptides and the Specific Case of Gomesin. *Adv Planar Lipid Bilayers Liposomes*. 2015;21:99-129. doi:10.1016/bs.adplan.2014.12.001
172. Mullineaux CW, Kirchhoff H. Using Fluorescence Recovery After Photobleaching to Measure Lipid Diffusion in Membranes BT - Methods in Membrane Lipids. In: Humana Press; 2007:267-275. doi:10.1007/978-1-59745-519-0_18
173. Kahya N, Scherfeld D, Bacia K, Poolman B, Schwille P. Probing lipid mobility of

raft-exhibiting model membranes by fluorescence correlation spectroscopy. *J Biol Chem*. 2003;278(30):28109-28115. doi:10.1074/jbc.M302969200

174. Sadoc JF, Charvolin J. Frustration in bilayers and topologies of liquid crystals of amphiphilic molecules. *J Phys*. 1986. doi:10.1051/jphys:01986004704068300
175. Vieira MGA, Da Silva MA, Dos Santos LO, Beppu MM. Natural-based plasticizers and biopolymer films: A review. *Eur Polym J*. 2011;47(3):254-263. doi:10.1016/j.eurpolymj.2010.12.011
176. Fujiwara T, Ritchie K, Murakoshi H, Jacobson K, Kusumi A. Phospholipids undergo hop diffusion in compartmentalized cell membrane. *J Cell Biol*. 2002;157(6):1071-1081. doi:10.1083/jcb.200202050
177. Wimley WC. Describing the mechanism of antimicrobial peptide action with the interfacial activity model. *ACS Chem Biol*. 2010;5(10):905-917. doi:10.1021/cb1001558
178. Yang L, Harroun TA, Weiss TM, Ding L, Huang HW. Barrel-stave model or toroidal model? A case study on melittin pores. *Biophys J*. 2001;81(3):1475-1485. doi:10.1016/S0006-3495(01)75802-X
179. Shai Y, Oren Z. From "carpet" mechanism to de-novo designed diastereomeric cell-selective antimicrobial peptides. *Peptides*. 2001;22(10):1629-1641. doi:10.1016/S0196-9781(01)00498-3
180. Karatekin E, Sandre O, Guitouni H, Borghi N, Puech PH, Brochard-Wyart F. Cascades of transient pores in giant vesicles: Line tension and transport. *Biophys J*. 2003. doi:10.1016/S0006-3495(03)74981-9
181. Puech PH, Borghi N, Karatekin E, Brochard-Wyart F. Line Thermodynamics: Adsorption at a Membrane Edge. *Phys Rev Lett*. 2003. doi:10.1103/PhysRevLett.90.128304
182. Fuertes G, García-Sáez AJ, Esteban-Martín S, et al. Pores formed by Baxα5 relax to a smaller size and keep at equilibrium. *Biophys J*. 2010. doi:10.1016/j.bpj.2010.08.068
183. Steinkühler J, De Tillieux P, Knorr RL, Lipowsky R, Dimova R. Charged giant unilamellar vesicles prepared by electroformation exhibit nanotubes and transbilayer lipid asymmetry. *Sci Rep*. 2018;8(1):11838. doi:10.1038/s41598-018-30286-z
184. Carvalho K, Ramos L, Roy C, Picart C. Giant Unilamellar Vesicles Containing Phosphatidylinositol(4,5)bisphosphate: Characterization and Functionality. *Biophys J*. 2008. doi:10.1529/biophysj.107.126912

7 Appendix

7.1 Supplementary Information

Name	Diameter	Charge	Material	Surface	Excitation (nm)	Detection (nm)	Producer	Additional information
1 µm amine	1 µm	+	Silica	Amine	488	495 - 530	Chemiecell	
6 µm amine	6 µm	+	Polystyrene	Amine	488	495 - 530	Polysciences	Autofluorescent property of polystyrene utilised
6 µm sulphate	6 µm	-	Polystyrene	Sulphate			Polysciences	
4 µm Janus	4 µm	-	Polystyrene	Sulphate/iron			Interfacial Dynamics Corp.	Half particle surface coated with iron
PILs	24.0 ± 6.5 nm	+	Poly(ionic liquid)				J. Yuan & M. Antonietti (MPIKG collaboration)	
Rh-PILs	37 ± 11 nm	+	Poly(ionic liquid)		561	570 - 700	J. Yuan & M. Antonietti	Labelled with Rhodamine-B

Fig. S 7.1 Summary of main properties for all particles used in both chapters in this thesis.

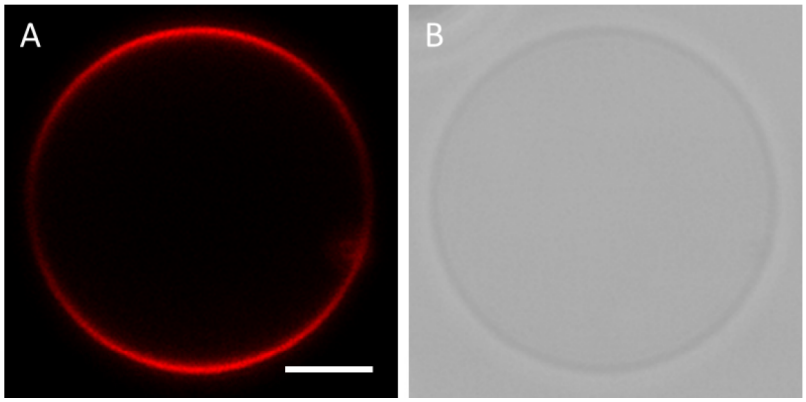

Fig. S 7.2 GUV viewed with confocal microscopy with visible membrane in bright field due to different solutions inside and outside vesicle. A) Fluorescent cross-section of 5% DOTAP GUV labelled with 0.2 mol% DiI. B) Same GUV viewed in transmission mode where the different refractive indices of the sucrose and glucose inside and outside the vesicle (respectively) give the vesicle a slightly darker interior and a brighter halo around the outside. Scale bar 5 µm.

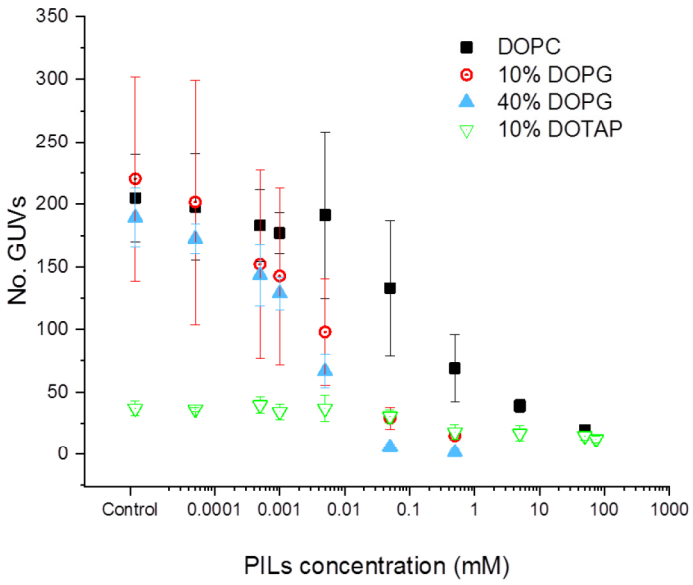

Fig. S 7.3 Raw data for the number of surviving vesicles in a population with increasing PILs concentration, adapted from [143].

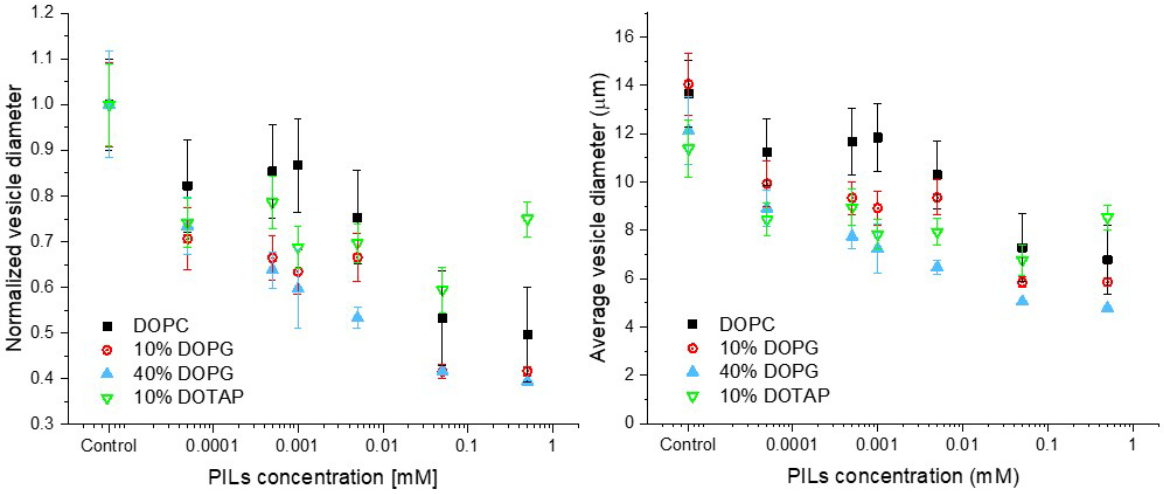

Fig. S 7.4 Changes in average vesicle size for all lipid compositions, normalised (left) and raw (right) data, adapted from [143]. The error bars represent standard deviation from three independent measurements.

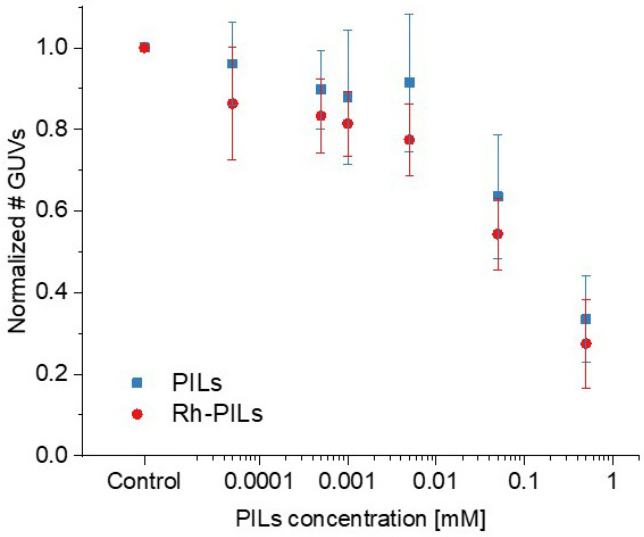

Fig. S 7.5. Comparison between changes in vesicle population as a function of PILs concentration for DOPC membranes with labelled and non-labelled PILs samples; adapted from [143].

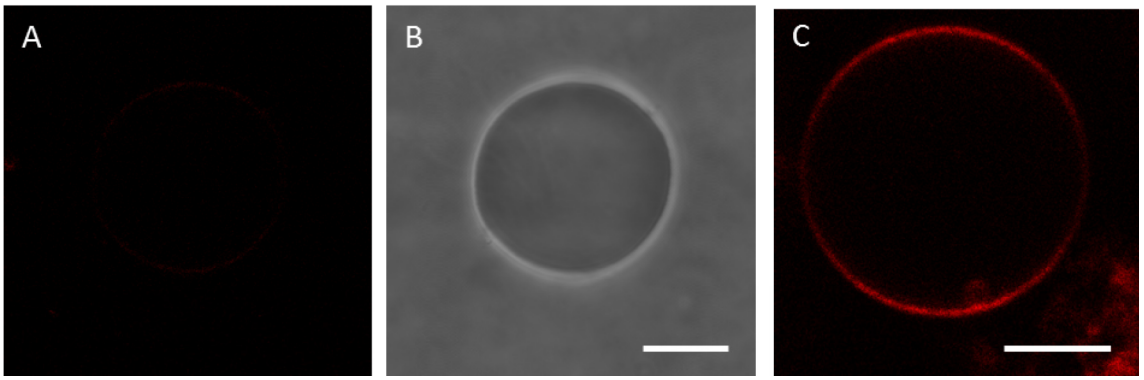

Fig. S 7.6. Comparison between non-labelled membranes without (A, B) and with Rh-PILs (C). (A) Confocal cross section of non-labelled membrane. (B) Phase contrast image of same vesicle as in (A). (C) Confocal cross-section of non-labelled DOPC GUV incubated with 0.5 mM Rh-PILs. This illustrates that fluorescent signal on membrane in contact with Rh-PILs is not a result of background signal or fluorescent contamination of vesicle sample. Scale bars: 5 µm.

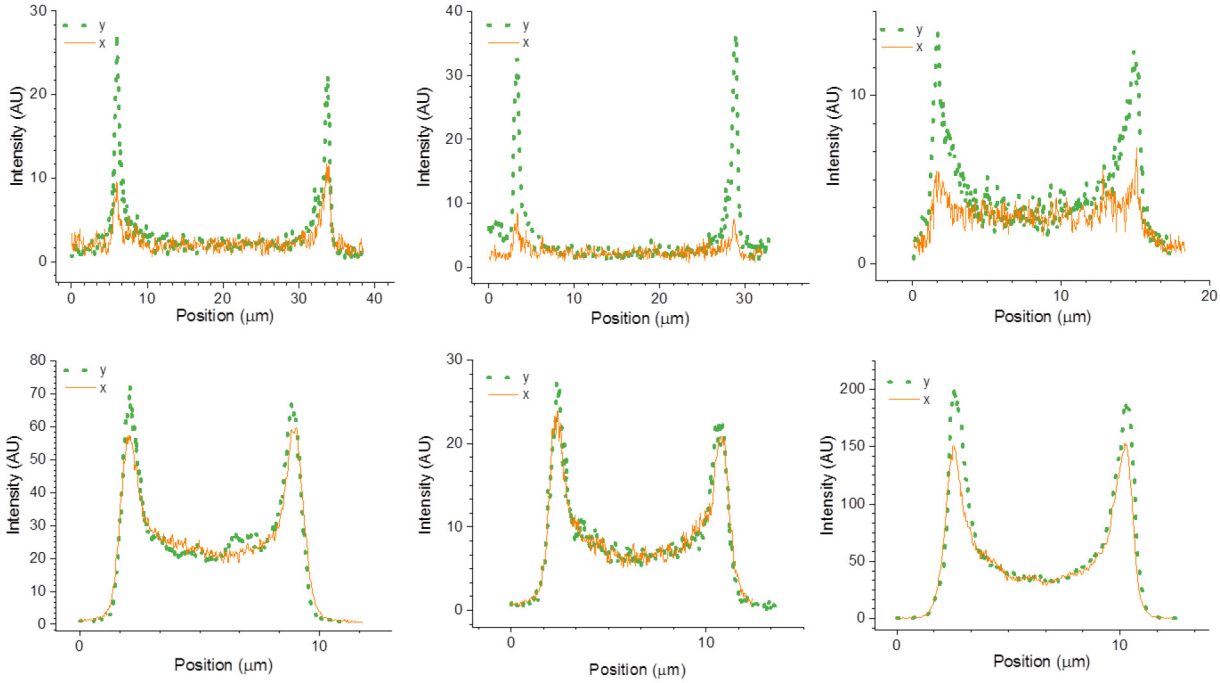

Fig. S 7.7. Additional line profile plots showing the polarisation effects of the rhodamine-B dye in the PIL nanoparticles on DOPC and 10% DOPG membranes; adapted from [143]. Top row is for DOPC membranes with 0.5 mM PILs, bottom row is 10% DOPG membranes with 0.0001 mM PILs.

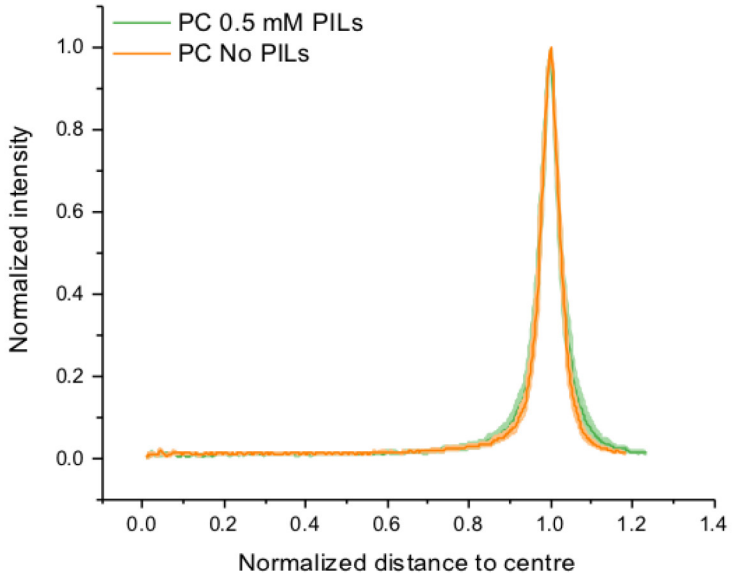

Fig. S 7.8 Fluorescent intensity at membrane interior with labelled membrane and non-labelled PILs, adapted from [143]. Radial profile of the fluorescence intensity signal averaged over the vesicle azimuthal angle and normalised by the maximum value as a function of distance from vesicle centre normalized by vesicle size for NBD-PE labelled DOPC GUVs with (green curve) and without (orange curve) 0.5 mM PILs. The intensity values show signal averaged from measurements on 10 GUVs, with the standard deviation shown as the error on the curves (orange and light-green bands).

7.2 List of figures

7.3 List of publications in preparation

Controlled adhesion, membrane pinning and vesicle manipulation (working title). **E. Ewins**, K. Han, B. Bharti, T. Robinson, R. Lipowsky, O.D. Velev, R. Dimova. *In preparation*.
See pages 22-46 for content; all figures used in publication will be different.

Mimicking cell pinocytosis using a purely synthetic system (working title). R. B. Lira, **E. Ewins**, I. Platzman, J. Spatz, R. Lipowsky, R. Dimova. *In preparation.*
Not presented here.